Seismic imaging of the geodynamic activity at the western Eger rift in central Europe and Fresnel zone imaging

DISSERTATION

To obtain the degree of PhD in Geophysics
at the Department of Earth Sciences
at Freie Universität Berlin
Faculty of Geophysics

Nirjhar Mullick

Berlin, 2016

Date of defense: 6th May, 2016

Supervisors:

Prof. Dr. Stefan Buske
TU Bargakademie Freiberg, Freiberg

Prof. Dr. Serge A. Shapiro
FU Berlin, Berlin

"I declare that this thesis is my original work and it has been written entirely by me. I have acknowledged all the sources of information which have been used in the thesis. This thesis has not been submitted for any degree in any university previously."

Berlin, May 2016

Nirjhar Mullick

Summary

This thesis consists of two parts. In part A, a geodynamically active region in Central Europe (western Eger rift) is investigated by seismic imaging. In part B, a new seismic imaging technique called ‘Fresnel zone imaging’ is developed.

The western Eger rift at the Czech-German border is an important geodynamically active area within the European Cenzoic rift system in the forelands of the Alps. Along with two other active areas of the ECRIS, the French Massif Central and the Eifel volcanic fields, it is characterized by numerous CO_2-rich fluid emission points and frequent micro-seismicity. Existence of a plume(s) is indicated in the upper mantle which may be responsible for these observations.

The subsurface of the western Eger Rift area is explored here by reprocessing a pre-existing deep reflection seismic profile called ‘9HR’. The subsurface structures as mapped by seismic reflectivity are interpreted with previous findings, mainly from seismological and geochemical studies, to investigate the observed geodynamic activity. Prominent hints of pathways are found which may allow magmatic fluids originating in the upper mantle to rise through the crust and cause the fluid emanations and earthquakes. The reflectivity image indicates existence of a non-permeable boundary in the upper crust below the swarm area that apparently acts as a fluid trap. The records of the P-to-S converted waves by this boundary from the P waves generated by the swarm earthquakes is employed to produce a P-to-S conversion image

between the swarm earthquakes and a seismological station at the surface conveniently located to receive such converted waves. A converter can be clearly identified which corresponds the non-permeable boundary below the swarm area confirming the existence of the fluid trap from another independent seismic dataset.

Seismic waves from a natural or controlled source reflected and mode converted at different subsurface structures can be recorded at a number of receivers. These recorded events can be then re-located to their points of origin to create an image of the subsurface. This process is known as seismic migration. The Fresnel zone imaging technique presented here is a seismic migration method which works by projecting the reflected/converted waves recorded at a number of receivers back to all potential Fresnel zones on all possible reflectors/converters from which the recorded waves may originate. The back projected reflected/converted waveforms interfere constructively at the actual reflectors/converters and destructively elsewhere to produce an image of the subsurface structures. The working principle is demonstrated on simple synthetic models containing single reflectors/converters as well as on the complex Marmousi model. Then, its application on real earthquake and reflection seismic data is presented.

The Fresnel zone imaging technique follows the same core imaging principle that underlies the Kirchhoff pre-stack depth migration method. However, in the Kirchhoff technique, the back projection process is not restricted to the Fresnel zones on the reflectors/converters which often cause significant noise and artifacts. The capabilities of the Fresnel zone imaging technique is illustrated against the Kirchhoff pre-stack depth migration in all of the given synthetic and real data examples.

Zusammenfassung

Diese Promotionsschrift besteht aus zwei Teilen. Im Teil A wird eine geodynamisch aktive Region in Mitteleuropa (westliches Egerrift) mittels seismischer Abbildungsverfahren untersucht. Im Teil B wird mit dem "Fresnelzonen-Imaging" ein neues seismisches Abbildungsverfahren entwickelt.

Das westliche Egerrift an der Grenze zwischen Deutschland und der Tschechischen Republik ist eine bedeutende geodynamisch aktive Region im Europäischen Känozoischen Riftsystem (ECRIS) im Alpenvorland. Zusammen mit zwei anderen aktiven Bereichen des ECRIS, dem französichen Zentralmassiv und den Vulkanfeldern der Eifel, zeichnet es sich durch CO2-reiche Fluidaustritte an zahlreichen Stellen und häufige Mikroseismizität aus. Diese deuten auf die Existenz eines Plumes im Oberen Erdmantel hin, der für diese Beobachtungen verantwortlich sein könnte.

Der Untergrund unter dem westlichen Egerrift wird hier mittels Reprozessierung des existierenden reflexionsseismischen Tiefenprofils "9HR" erkundet. Die geologischen Untergrundstrukturen, wie sie sich mit der seismischen Reflektivität abbilden, werden zusammen mit den bisherigen Erkenntnissen, hauptsächlich von seismologischen und geochemischen Untersuchungen interpretiert, um die beobachtete geodynamische Aktivität zu untersuchen. Darin finden sich Anzeichen von Wegsamkeiten, die es magmatischen Fluiden erlauben, aus dem Oberen Erdmantel durch die Erdkruste aufzusteigen, an der Erdoberfläche

auszutreten und Erdbeben zu verursachen. Das Reflektivitätsabbild deutet die Existenz einer nichtpermeablen Grenze in der Oberen Kruste unterhalb des Schwarmbebengebietes an, die offensichtlich als Fluidbarriere wirkt. Daneben werden die Aufzeichnungen von P-Wellen, die von Schwarmbeben hervorgerufen und an Grenzschichten in S-Wellen umgewandelt werden, benutzt, um ein Abbild dieser Konversionsfläche zwischen den Hypozentren der Schwarmbeben und den seismologischen Stationen zu erzeugen. Ein Abbild einer konvertierenden Grenzschicht ist in den Daten deutlich erkennbar und entspricht der oben genannten nichtpermeablen Grenze unterhalb des Schwarmbebengebietes. Damit wird die Existenz einer Fluidbarriere mit Hilfe eines zweiten unabhängigen Datensatzes bestätigt.

Seismische Wellen, hervorgerufen von einer natürlichen oder künstlichen Quelle, die an verschiedenen Untergrundstrukturen reflektiert oder umgewandelt werden, werden von einer Vielzahl von Empfängern aufgezeichnet. Diese aufgezeichneten Ereignisse können dann an ihrem Entstehungsort abgebildet werden, um ein Abbild der Untergrundstrukturen zu erhalten. Dieses Verfahren ist als seimische Migration bekannt. Das Fresnelzonen-Imaging, das hier vorgestellt wird, ist ein seismisches Migrationsverfahren, das das aufgezeichnete reflektierte / konvertierte Wellenfeld in alle potentiellen Fresnelzonen auf allen möglichen Reflektoren / Konversionsflächen rückpropagiert, von denen das aufgezeichnete Wellenfeld hervorgerufen wurde. Die rückpropagierten reflektierten / konvertierten Wellenformen überlagern sich konstruktiv an der Position des tatsächlichen Reflektors / der tatsächlichen Konversionsfläche und destruktiv an allen anderen Stellen, um ein Abbild der Untergrundstrukturen zu liefern. Das Arbeitsprinzip wird anhand einfacher synthetischer Modelle, die einen einzelnen Reflektor / eine einzelne Konversionsfläche enthalten, sowie anhand des komplexen Marmousi-Modells gezeigt.

Das Fresnelzonen-Imaging folgt dem gleichen Abbildungsprinzip, das der Kichhoff-pre-stack-Tiefenmigration zugrunde liegt. Jedoch ist die Rückpropagation der aufgezeichneten Wellen in

der Kirchhoff-Migration nicht auf die Fresnelzonen auf den Reflektoren / Konversionsflächen beschränkt, was oft erhebliches Rauschen und Migrationsartefakte hervorruft. Die Vorteile der Fresnelzonen-Migration gegenüber der Kirchhoff-pre-stack-Tiefenmigration werden anhand synthetischer und realer Datenbeispiele dargestellt.

Contents

List of Figures

List of Tables

List of Abbreviations

CB	Cheb Basin gas escape center
ECRIS	European Cenozoic Rift System
FZI	Fresnel zone imaging
GRSN	German Regional Seismological Network
KV	Karlovy Vary gas escape center
KL	Konstantinovy Lázně gas escape center
KPSDM	Kirchhoff pre-stack depth migration
ML	Mariánské Lázně gas escape center
NK	Novy Kostel
TWTT	Two way travel time

A Seismic imaging of the geodynamic activity at the western Eger rift in central Europe

A.1 Introduction

The Alpine foreland hosts a series of rift zones stretching over a length of over 1000 km, collectively known as European Cenozoic Rift System. Graben structures are formed on top of massifs originated during the European Variscan orogeny in the late Paleozoic along with traces of Tertiary and Quarternery intraplate volcanism (primarily alkaline). Surface expressions of present day magmatic activity can be observed at the French Massif Central (Matthews et al., 1987), the east and west Eifel volcanic fields at the Rhenish Massif, Germany (Griesshaber et al., 1992) and the western Eger rift at the Bohemian Massif located at the Czech Republic-German border (Weinlich et al., 1999) in the form of CO_2 degassing fields. The rifting and volcanism has been modeled mostly as the effect of the Alpine orogene. However, geochemical and geophysical studies suggest that a single or a series of small-scale mantle plumes originating from a thermally and geochemically anomalous layer beneath the European lithosphere may be responsible (Goes et al., 1999; Granet et al., 1995).

Along with the CO_2-rich fluid emission fields which are commonly observed at all three

active parts of ECRIS at the French, Rhenish and Bohemian Massifs, the western Eger rift area at the Bohemian Massif is characterized by frequent small-magnitude earthquakes often in large swarms. The majority of the seismicity in the region is concentrated to an area at the Czech village Nový Kostel close to the Czech-German border where intermittent earthquake swarms of magnitude less than 3.5 occur. Documented changes in the regional fluid activity during and after the swarms (Bräuer et al, 2008), seismological studies of the spatiotemporal evolution of the swarm activity (Fischer et al, 2014) and also numerical modeling of the recent swarms in 2000 and 2008 (Hainzl et al., 2005, Parotidis et al., 2003) point to pressurized fluids as being responsible for the earthquakes.

Isotopic analysis of the emitted fluids at different locations at the western Eger rift shows that they have a significant portion of the upper mantle derived components. In addition, high gas flux and high crustal transport velocity suggests direct degassing channels along deep-reaching faults. These observations indicate existence of a magmatic fluid source in the upper mantle (Weinlich et al, 1999). Receiver function imaging of the area reveals an updoming of the Moho up to a depth of 27 km with an average depth of 31 km in the surrounding region (Geissler et al., 2005). Anomalies in the receiver functions and also high resolution teleseismic travel time tomography of the upper mantle suggest a velocity increase at 50 km depth followed by a decrease at 65 km depth (Geissler et al., 2005, Plomerova et al., 2007). This has been interpreted as either local updoming of the lithosphere-asthenosphere boundary (LAB), the existence of confined partial melt, or a combination of both.

Based on the above studies, the geodynamic activity of the western Eger rift area has been hypothesized to be caused by magma from a source in the upper mantle which rises to the bottom of the crust (Geissler et al., 2005). Then CO_2-rich fluid separates out from the magma and reaches the surface via a number of direct paths. The ascent of this fluid through the crust generates the observed micro-seismicity.

A number of reflection/refraction seismic profiles exist at the Bohemian Massif, collected in the 1990s to study its internal structure. Out of these, the Czech 9HR profile runs close to both the swarm earthquake and gas escape observations. The CMP processed migrated section of the profile shows an updoming of Moho and a number of upper mantle reflections indicating possible basalt intrusions below the swarm earthquake area. The part of the profile close to the swarm and fluid area is reprocessed here with modern advanced seismic imaging techniques to produce a higher resolution image of the subsurface up to a depth of 60km. The image is then correlated with seismicity and fluid observations to investigate traces of magma bodies, rising fluids and the circumstances under which they may produce earthquakes.

A.2. Study area

A.2.1 Geological setting

The 1100 km long European Continental Rift System (ECRIS) extends from the North Sea coast to the Mediterranean (Figure A.1) and is presumably formed due to compression of lithosphere in response to the Alpine and Pyrenean orogenies in the late Eocene (Dezes et al., 2004). Its northern part includes the Rhine Rift System (the Upper Rhine, Roer Valley and Hessian grabens) and its southern part, the Massif Central grabens (Limagne, Roanne, Forez), the Bresse Graben and the grabens of the lower Rhône Valley (e.g., Valence, Alès, Manosque, Camargue).

The Bohemian massif is a large massif occupying parts of Czech Republic, Germany, Poland and Austria surrounded by four ranges: the Ore Mountains in the northwest, the Sudetes in the northeast, the Bohemian-Moravian Highlands in the southeast, and the Bohemian Forest in the southwest. It originated in the Late Paleozoic during the collision between the paleocontinents Gondwana and Laurassia (European Variscan orogeny) and consists of four major geological units (Figure A.2): the Saxothuringian zone in the north-east, the Teplá-Barrandian zone, the Moldanubian zone in the centre and the microcontinent Bruno-Vistulian in the southeast (Kosmet, 1927). The easternmost part of the ECRIS affects the western part of the massif at the transition zone of the first three of the above units and the 300 km long and 50 km wide ENE–WSW trending Eger rift zone is formed (Figure A.1).

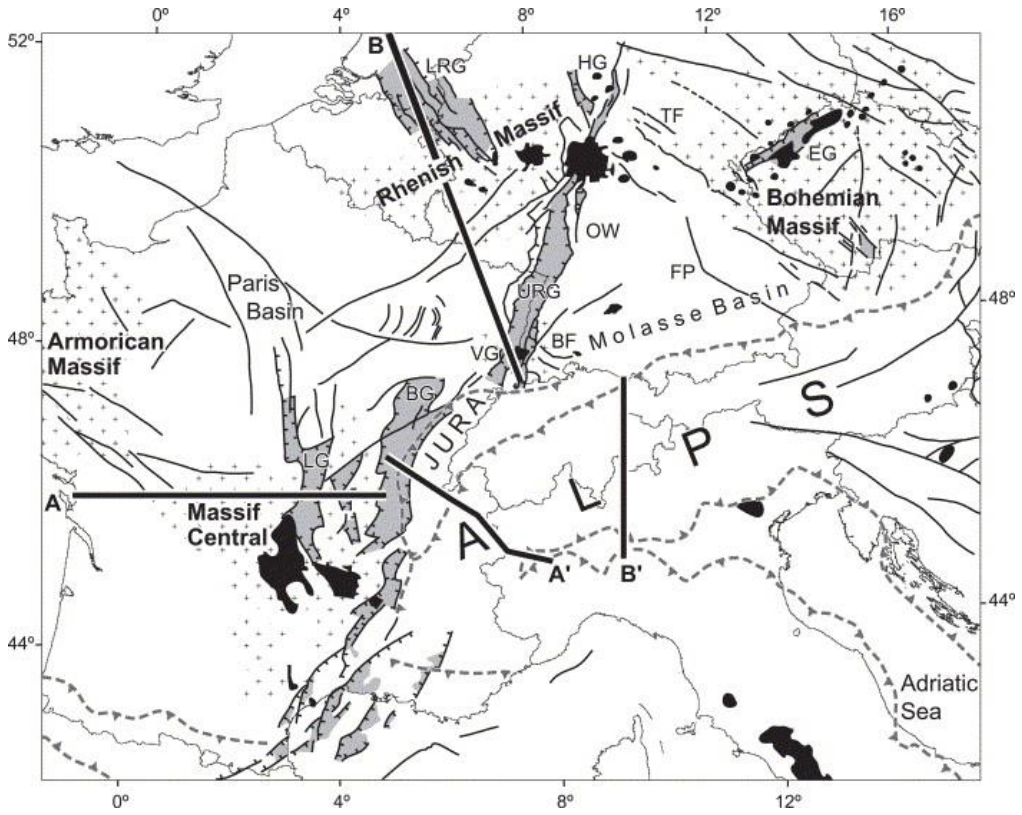

Figure A.1 Location of the European Continental Rift System in the Alpine foreland; light grey areas denote rift-related sedimentary basins, cross patterns the Variscan massifs and black areas the volcanic fields. BG: Bresse Graben, EG: Eger (Ohre) Graben, HG: Hessian Grabens, LG: Limagne Graben, LRG: Lower Rhine (Roer Valley) Graben, URG: Upper Rhine Graben. (De`zes et. al., 2005)

The study area is located on the western part of the Eger rift. The crust here is composed of magmatic and metamorphic rocks overlaid by unconsolidated sediments of Permo-Carboniferous, Jurassic, Cretaceous and Cenozoic ages. It has been affected by alkaline magmatism/volcanism since the Upper Cretaceous. Active volcanism, which is commonly associated with earthquake swarm activity in other parts of the world, is not present. However, Quaternary-aged volcanoes, Komorní Hůrka (0.45-0.9 Ma) and Železna Hůrka (0.17-0.4 Ma), and Mýtina Maar are situated within 15 and 25 km respectively from the swarm earthquake area (Wagner et al., 2002) on the flanks of the Eger rift. Numerous faults of different orientations exist in the area (Bankwitz et al., 2003) along with the morphologically

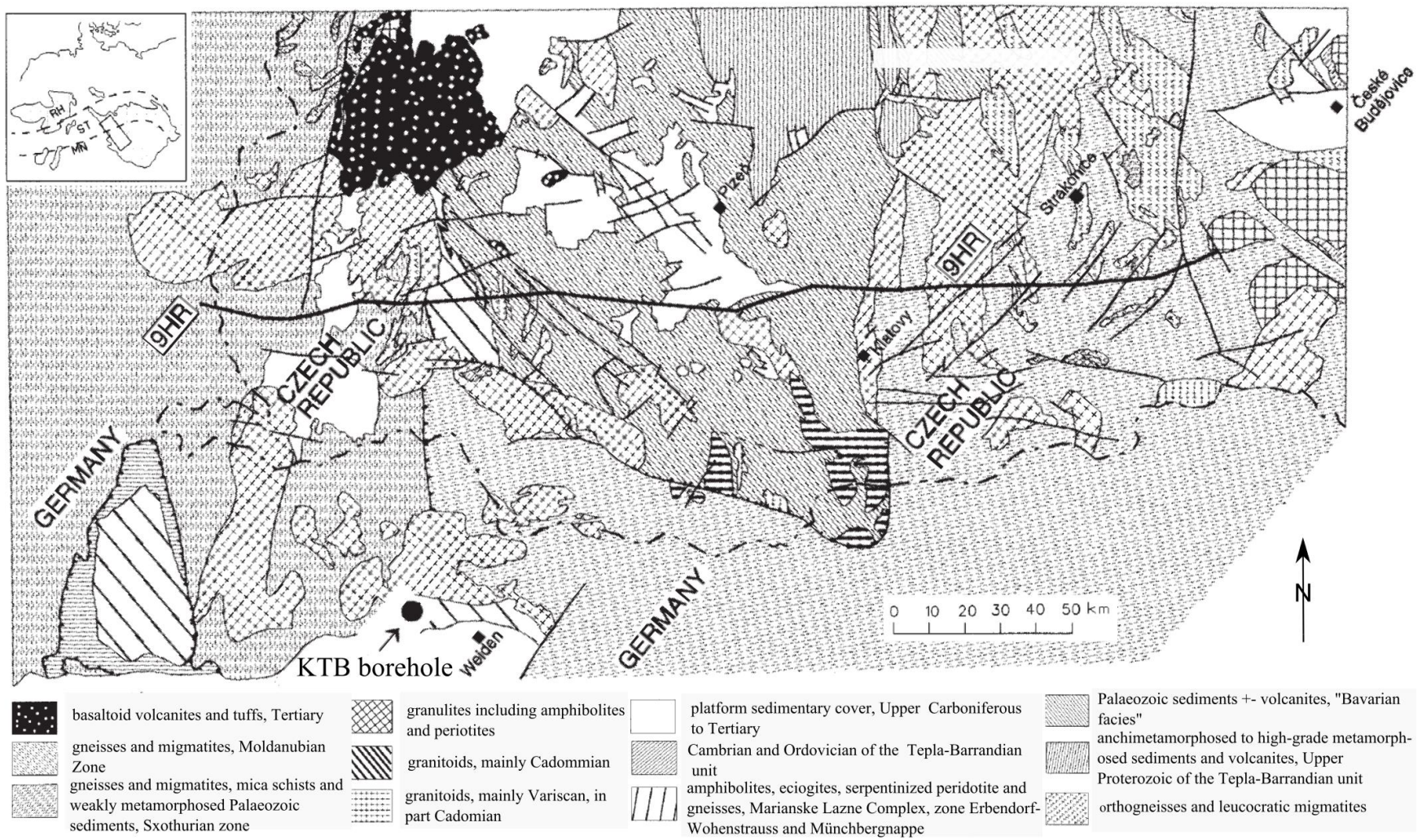

Figure A.3. Geological map along 9HR profile. Inset shows location of the area in Central Europe (enclosed in rectangle) along with Rhenohercynian (RH), Saxothuringian (ST) and Moldanubian (MN) Zones of the Variscan orogeny (Vrána and Štědrá, 1998).

prominent Mariánské-Lázně fault zone (MFZ) and the Počátky-Plesná fault zone (PFZ). Although MFZ and PFZ intersect each other at the main focal zone of regional seismicity, no direct relationship between the faults and the swarm and/or fluid activity has been proven so far.

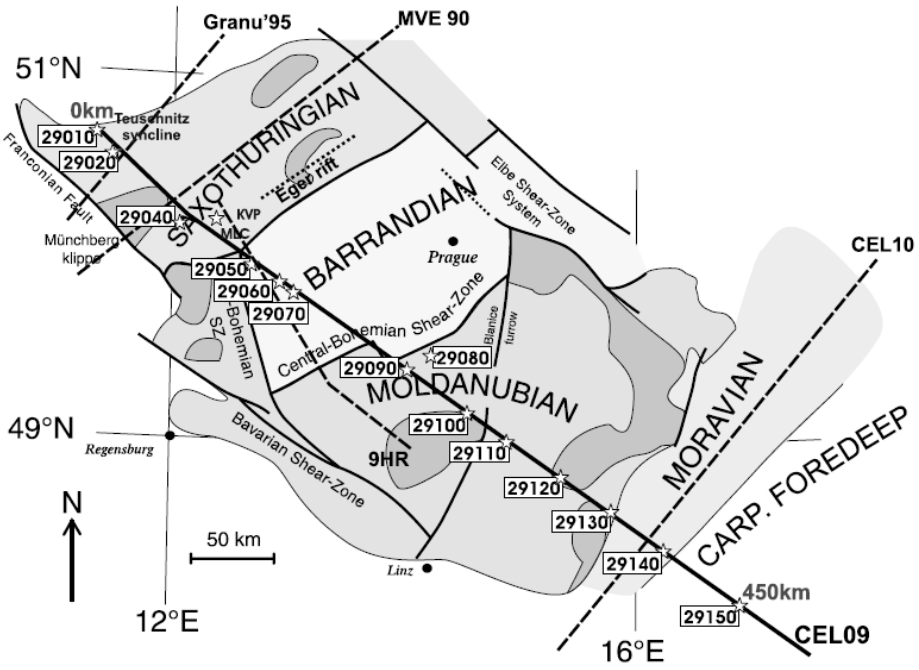

Figure A.2. Major tectonic units of the Bohemian Massif along with different reflection and refraction profiles located on it. (Hrubcova et al., 2005)

The 9HR profile starts in the Saxothuringian Zone unit of the Bohemian Massif (Figure A.2), continues to the SE across the Teplá-Barrandian unit (TBU) and into the Moldanubian Zone (Vrana and Sedara, 1998). The profile was originally acquired to investigate the internal crustal structure of the interior part of the Bohemian Massif. A detail geological map of the massif along the profile is given in Figure A.3.

A.2.2 Geodynamic activity

A.2.2.1 Fluid emissions

At the study area, the CO_2-dominated fluid is released from the subsurface in free or dissolved

state through eight moffette (dry gas vents) fields and more than 100 mineral springs spread all over the region (Figure A.4). The degassing points can be grouped into four major gas escape centers (Weinlich et al., 1999): Cheb Basin, Mariánské Lázné, Konstantinovy Lázné and Karlovy Vary. The Cheb Basin center and the Mariánské Lázné center are the largest in dimensions (~ 150 km^2) whereas the Karlovy Vary center dominates in terms of gas flux with approximately 356000 dm^3 per hour (Bräuer et al., 2008).

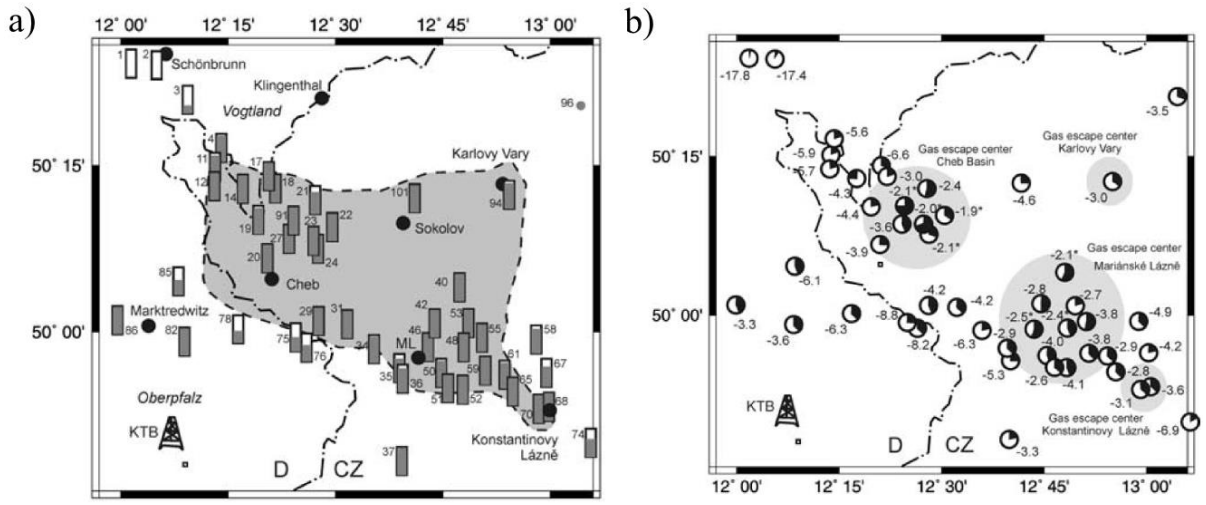

Figure A.4. a) The CO_2 concentrations of the emitted gas (represented by the amount of shading) at the western Eger Rift area at selected locations. The shaded area marks the region of nearly pure CO_2 escape (>99 %). b) Isotope ratios at the same locations. The solid quarters denote the MORB-type He (%), the numbers are $\delta^{13}C$ values (%), and shaded circular areas are gas escape centers. (Geissler et al., 2005)

The gas emitted at all the centers consists primarily of CO_2 (99%), N_2, He and CH_4. The range of $^{13}C/^{12}C$ ($\delta^{13}C_{CO2}$) values is nearly the same at all gas escape centers and varies between -1.8% and -4%. However, the air corrected $^3He/^4He$ ratio (measured ratio divided by atmospheric ratio) varies across different centers over a range between 2.4 to 6.1 with a maximum at the Cheb Basin center (Bräuer et al., 2008). These values are very high compared to a typical crustal value of less than 0.1. The approximate transport velocity of the fluid in the upper crust is estimated to between 50-400m per day (Bräuer et al., 2008).

During the weekly gas-isotope sampling carried out between May 2000 to December 2003 which included the year 2000 swarm, increasing presence of the mantle-helium was observed at Cheb basin center while at the Mariánské Lázné center, it did not vary much (Brauer et al., 2011). The former is adjacent to the swarm area and has more seismicity than the latter and thus the growth of $^{3}He/^{4}He$ ratio may indicate ongoing magmatic processes below that are also responsible for the earthquakes (Fischer et al., 2014). On the other hand, at locations such as Wettinquelle spring and at Bublák a decrease of the $^{3}He/^{4}He$ ratio was observed during the 2000 swarm. However, this is speculated to be related to the strain changes of the rocks at the initiation stages of the earthquakes (Brauer et al., 2008).

A.2.2.2 Earthquakes

An earthquake swarm is a series of a large number of relatively comparable, small-magnitude earthquakes with a short time interval between consecutive events, and with no main shock-aftershock sequence as usually observed with fault displacement earthquakes. Earthquake swarms occur at a very heterogeneous stress field and/or a weakened crust, which lacks a single well-developed fault and thus cannot maintain higher strain (Mogi, 1963). They are often observed in volcanic areas, geothermal fields and ocean ridges (e.g. Wyss et al., 1997; Lees, 1998; Dreger et al., 2000).

The seismic activity of the study area is predominantly earthquake swarms with quiet periods of occasional micro-seismicity in between. This is an example of intra-plate earthquake swarms without active volcanism as in other continental rifts like Rio Grande, Kenya (Fischer et al., 2014). The report of swarm activity in the area dates back to 1552 (Grünthal, 1989). The earliest activity analyzed is the series of more than 100 macro-seismic earthquakes in 1824 by Knett (1899). The strongest known earthquakes occurred on March 6, 1872, and November 3, 1908, both of magnitude 5. In recent times, major swarms were observed in

1962/63, 1968, 1973, 1974/75, 1982/83, 1984, 1985/86, 1997, 2000, 2008 and 2011.

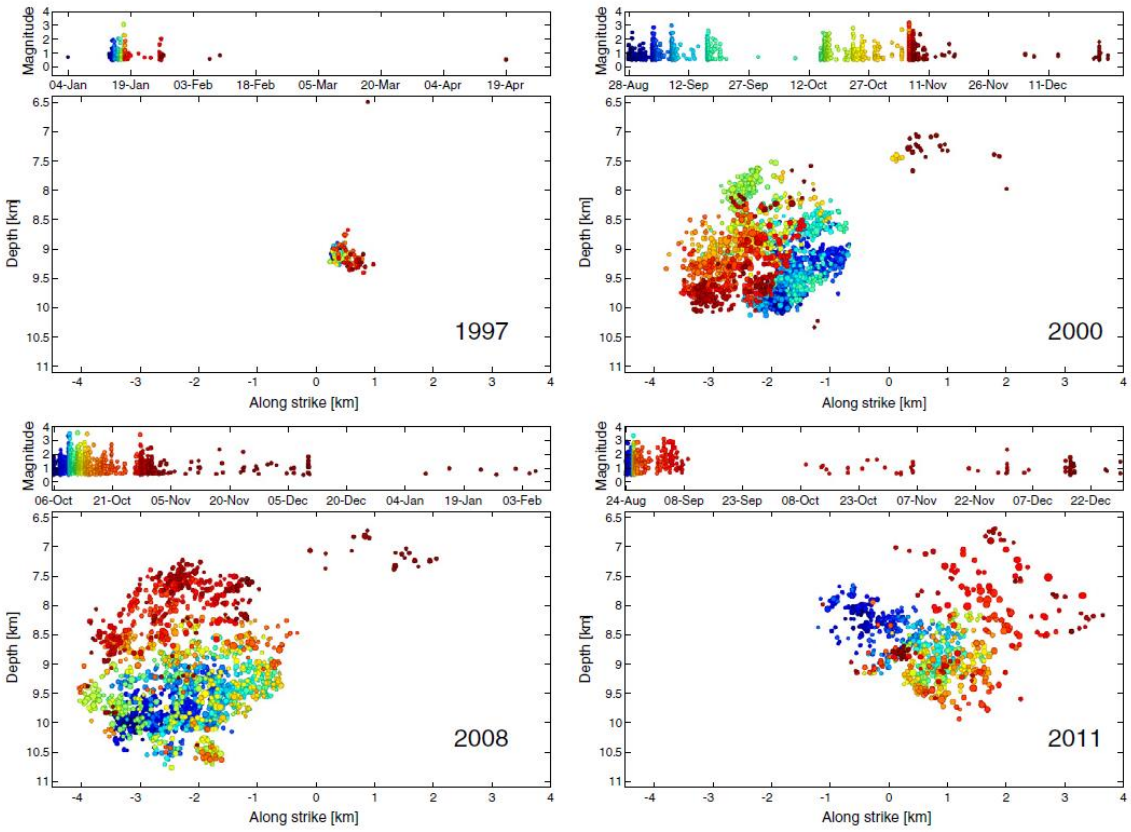

Figure A.5. The spatiotemporal evolution of the swarms of year 1997, 2000, 2008 and 2011 in the fault plane view (bottom) and their magnitude–time plots (top). Colors represent the event order in time. (Fischer et al., 2014)

The seismicity in the period 1991-2011 spreads over an area of approximately 40 x 60 km with the majority of the earthquakes occurring within 20 km from the surface. During this time span, three massive earthquake swarms took place in August-December 2000 (M_L 3.3), October-November 2008 (M_L 3.8) and August-September 2011 (M_L 3.5) with around 7000, 10000 and 25000 events, respectively with a magnitude range between -2.0 to 3.8. These three recent swarms show subsequent increased speed of release of seismic moment with durations of 10 weeks, 4 weeks and 2 weeks respectively (Fischer et al., 2014). The hypocenters of the swarms cluster on a near-vertical plane (70^0-80^0) to the West between depths of 7 to 10 km

beneath the village Novỳ Kostel (NK) in the Czech Republic (Horalek and Fischer, 2008). The swarm activities of year 2000 and 2008 coincide on the same region of the NK focal zone whereas that of year 2011 shifts towards the north (Figure A.5).

Precise hypocenter locations of the year 2008 swarm obtained with the double-difference location method (accuracy less than 20m) reveals (Vavryčuk et al., 2013) that the fault active during the swarm is composed of a number of fault segments with different orientations (Figure A.6a). Stress analysis using the same events shows that the events can be assigned to two principle fault planes (Figure A.6b). The seismicity distribution can be divided into two interconnected major segments that are located along these planes. A study of the source time functions of selected events of magnitude range 1.7-3.7 from the same year 2008 swarm indicate that the focal mechanisms are frequency dependent (Vavryčuk et al. 2011). The low frequency band source time functions are produced by shear rupturing along a fault whereas the high frequency functions are caused possibly by weak tensile vibrations of the fault.

Analysis of the spatio-temporal distribution of earthquake hypocenters in the study area shows that the seismic activity occurs at a number of focal zones at different times as well as at a number of focal zones at the same time (Fischer et al., 2014). Inter-event time distribution of the year 2000 swarm shows that it obeys a power law except for the starting phase which shows an exponential distribution (Hainzl and Fischer, 2002). This is interpreted as triggering of the swarm by an increase in fluid-pore pressure followed by self-organization due to local stress transfer.

Migration of foci is common for earthquake swarms and observed in all recent swarms of 2000, 2008 and 2011. The year 2000 and 2008 shows a similar pattern. The swarm initiates at the bottom of the near-vertical plane and migrates upwards and stops at similar depths. The spatio-temporal evolution of 2011 swarm starts at the north edge of the 2008 swarm cluster

and then migrates upward stepwise to the north. Such migration of hypocenters suggests movement of pressurized fluid (Spicak and Horalek, 2000) causing earthquakes due to changes made to the local stress distribution. This is supported by numerical modeling of the year 2000 swarm (Parotidis et al, 2003) which shows that the starting phase of the swarm activity could be explained by diffusion of pressurized fluid into a poro-elastic zone.

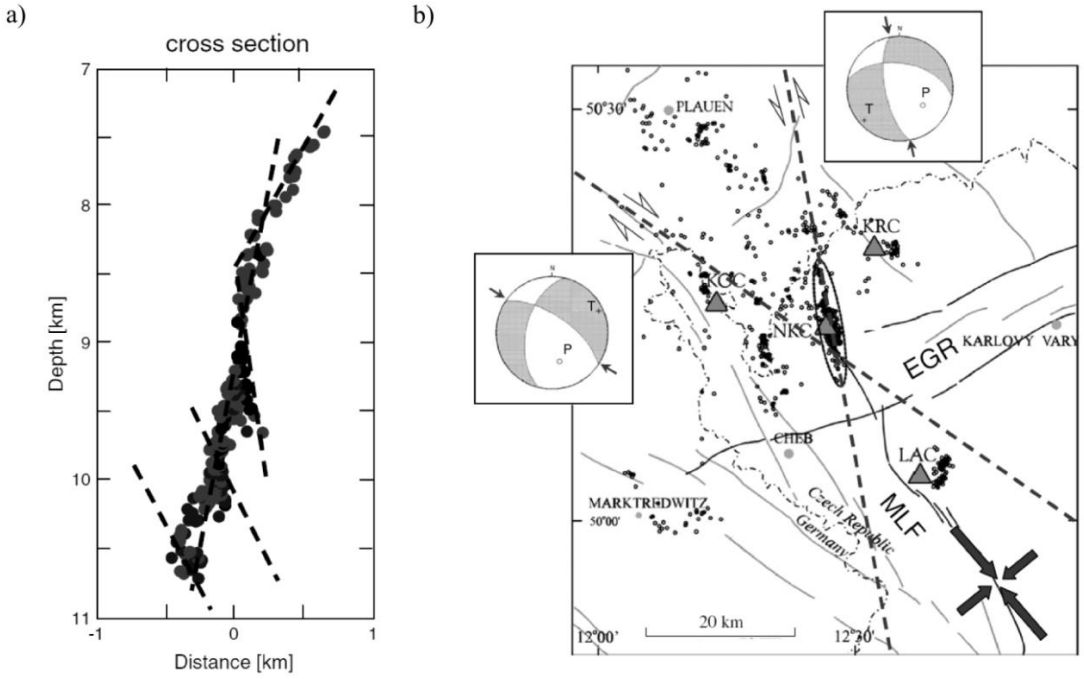

Figure A.6. a) Locations of the hypocenters of year 2008 swarm with double difference technique. Different segments of the active fault are indicated by dashed lines, b) Orientations of the principal faults from stress analysis of the same events (denoted by dashed lines). The arrows represent the orientation of maximum and minimum compressive stress axes. The dots represent the epicenters of micro-earthquakes that occurred in 1991–2008. The most active fault zone is enclosed in ellipse. MLF: Mariánské–Lázně fault and EGR: Eger Rift. (Vavryčuk 2011)

The $\frac{V_P}{V_S}$ ratio at the focal zone for all the swarms in year 1997, 2000 and 2008 sharply decreases before and during the primary phases of the swarm activity from 1.7 down to 1.3 and returning to the background value at the end of the swarms (Dahm and Fischer, 2014).

This is interpreted as presence of oversaturated fluids degassing during the beginning phases of the swarm activities.

A.2.2.3 Hypothesis

An upwelling of the Asthenosphere below the western Eger Rift is indicated by numerous studies (Plesinger et al., 1994; Passier and Snieder, 1996; Babuska and Plomerova, 2001 etc.) along with a Moho updoming (Geissler et al., 2005). In addition, an upper mantle seismic entity exists at depth of 50-60km (Tomek et. al., 1997; Geissler et al., 2005) which has been interpreted as base of a highly metasomatic mantle volume that has been intruded by melts. Considering the upper mantle origin of the fluid emitted at the surface revealed by the isotope studies, this entity could be the magma/fluid reservoir that supplies the fluids. Tomography studies and seismological observations reveal a complex transition zone at the Moho boundary (Giese, 1976; Hemmann et al., 2003, Geissler et al., 2005). The crust-mantle boundary can provide resistance to the ascending magmas which may cause the magma to pond at the base of the crust with occasional intrusions into the lower crust creating such a broad and complex zone at the Moho. Compiling all these observations a conceptual model of the Geodynamic activity at the study area may be constructed as (Geissler et al., 2005),

1) A magma reservoir exists in the upper mantle at depth of 50-60km beneath the western Eger Rift area
2) CO_2 dominated magma is released from this reservoir at depth of 60-30km which ascends via a number of channels
3) As it reaches the bottom of the crust, the intrusion causes an active up doming of the Moho from 31km to 27km
4) At a depth 29-21 km, the CO_2 dissolved in the magma separates out and transported through crust via deep reaching channel-like paths

5) Beneath the swarm area, high pressure of the ascending fluids causes micro-earthquakes at depths of 15km-6km

6) At the gas escape centers, the fluid paths rise up to the surface and causes fluid emissions.

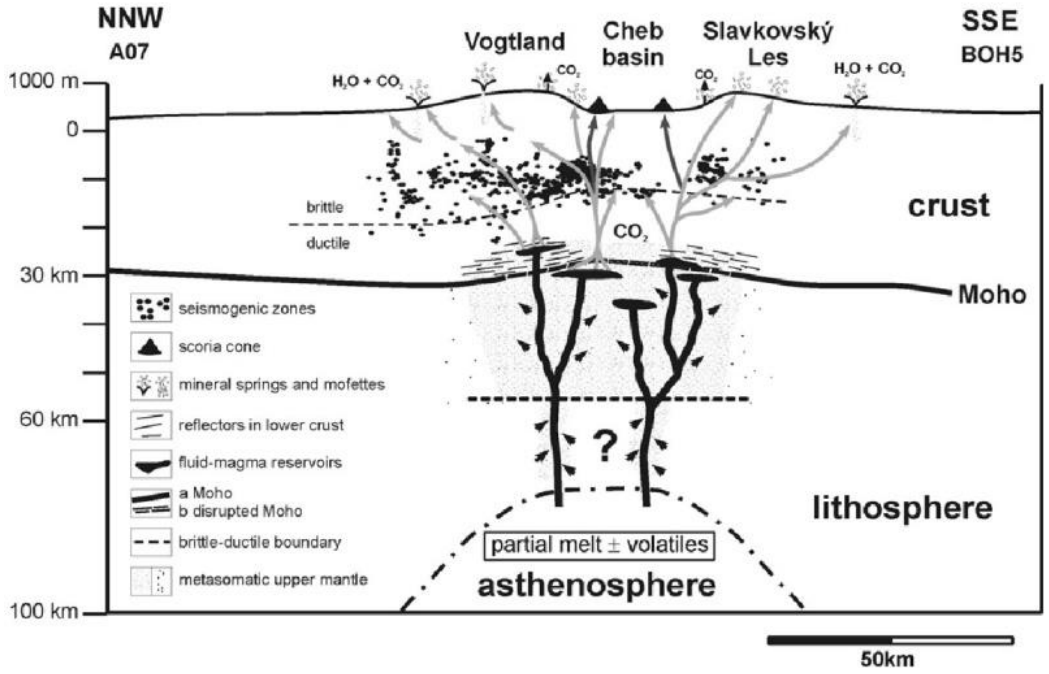

Figure A.7. Hypothetical geodynamic processes at the western Eger Rift.

A.3. Reprocessing of 9HR profile

A.3.1 Seismic migration

Active reflection seismic is one of the major geophysical techniques to investigate the subsurface of the Earth. Elastic waves are generated at the Earth's surface by means of an artificial source such as blasting dynamite in drilled holes or shaking the ground with a seismic vibrator (Figure A.8a). As the elastic wave travels downward and meets subsurface structures with certain impedance (product of density and velocity) contrast, a part of it is reflected upward and the rest is refracted/transmitted and continue downward. The reflected wave-field is recorded by a number of receivers at the surface starting from the time of triggering of the source.

The record of the reflected wave-field at each receiver consists of the reflected source pulse at time equal to the two way travel time (TWTT) from source to the reflection point and back to the receiver and is called a seismic section (Figure A.8b). E.g. in case of non-zero offset (source and receiver is not coincident) acquisition over a plane reflector, the arrival time of the reflected wave at increasing distance from the source increases in a hyperbola. Consequently, the seismic section comprises of the recorded source wavelets arranged along a hyperbola. The horizontal shift of the tip of this hyperbola from the source position depends upon the dip of the reflector. A seismic section can be utilized many ways (e.g. migration, full waveform inversion, amplitude vs offset analysis, tomography etc.) to find various information about the

subsurface such as its structure, seismic velocities, density, porosity etc.

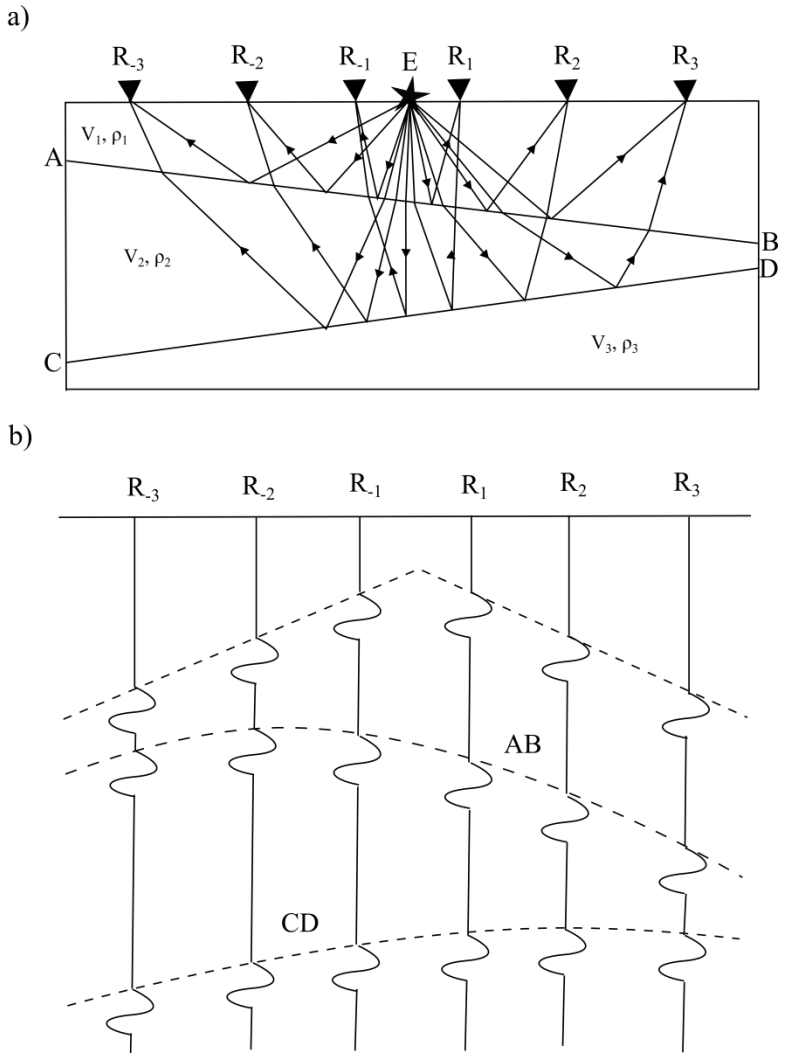

Figure A.8. a) Acquisition geometry of an active seismic survey in split spread configuration with three receivers R_{-1}, R_{-2}, R_{-3} and R_1, R_2, R_3 on either side of the shot E. The subsurface contains two inclined plain reflectors AB and CD; b) Record of the direct wave from E and reflected waves from the reflectors AB and CD at the receivers. Note the hyperbolic shape of the reflected arrivals and the shift of the reflection hyperbolas up the dip of the corresponding reflectors.

Seismic migration is the process to produce an image of the subsurface structures by placing the recorded reflection events in a seismic section to the location where they originated. To present a simple technique of migration, we consider a zero-offset seismic acquisition

experiment which consists of three sources E_1, E_2 and E_3 triggered at regular intervals at three points A, B, C along a straight survey line (Figure A.9a). The subsurface contains an inclined straight reflector AB at dip α and a constant velocity V_1 above the reflector. Single receivers R_1, R_2 and R_3 coincident with the sources record the reflected waves from AB. The seismic section in this case consists of reflected source wavelets recorded at times t_1, t_2 and t_3 at points A, B, C respectively along a straight line at dip β (Figure A.9b).

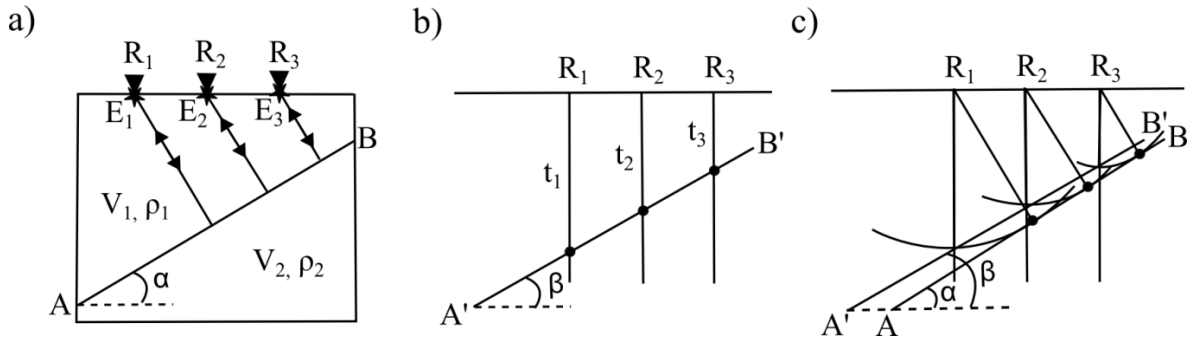

Figure A.9. A simple technique of seismic migration with zero-offset data; a) acquisition geometry with a subsurface reflector at dip α , b) recorded seismic section with reflector at apparent dip β, c) migrated section with reflector at the correct dip α.

The recorded seismic section gives the impression that the dip angle of the subsurface reflector AB is β. To obtain the actual reflector dip, we note that, 1) the reflection point for a reflected wave recorded at the zero-offset receiver at time t can be any point of the subsurface on the circular arc of radius V_1t with the source-receiver point as center of the arc and 2) all the reflection points lie along the same straight line along the reflector AB. Thus, the true reflector at the true dip α can be determined by drawing circular arcs from the points A, B, C with radii V_1t_1, V_1t_2, V_1t_3 respectively and finding their common tangent line (Figure A.9c).

Seismic migration was developed in the 1960s for surface seismic and later extended in 1980s and 1990s to vertical and cross-well seismic as well. Early migration techniques were based on the concept of common mid-point (CMP). Tthe recorded signal is sorted into groups or

gathers that share the same midpoint between source and receiver. Then migration is performed on this sorted data on the assumption that the subsurface reflectors are horizontal and velocity varies only in depth. However, such assumption is valid only in simple geological environments such as sedimentary basins and often fails in more structurally complex areas. This led to development of generalized seismic migration techniques that are based on seismic wave propagation.

A.3.2 Kirchhoff pre-stack depth migration

Kirchhoff pre-stack depth migration (KPSDM) is a seismic migration technique based on integral solution of the high frequency approximation of the wave equation (Schneider 1978). The wave field recorded at a number of source and receiver pairs is back propagated into the subsurface and reflectors are imaged by constructive interference of the back propagated waves. The image value M (**r**) at a subsurface point **r** is given in a general form as,

$$M(\mathbf{r}) = \int \int_A W(\mathbf{r}, \mathbf{r_0}).\acute{U}\left(\mathbf{r_0}, t_{ER}(\mathbf{r}, \mathbf{r_0})\right) dr_0 \qquad \ldots.(A.1)$$

where $\mathbf{r_0}$ is a vector describing the source and receiver locations, t_{ER} (**r**, $\mathbf{r_0}$) is the travel time from source to the point **r** plus the travel time from the point **r** to receiver for a source-receiver pair at $\mathbf{r_0}$, U($\mathbf{r_0}$, t_{ER} (**r**, $\mathbf{r_0}$)) is the recorded wave field at the time t_{ER} for the same source-receiver pair and W(**r**, $\mathbf{r_0}$) is a weighting factor that corrects the amplitudes of the back propagated wave field for geometrical spreading and obliquity. The domain of the surface integral A is a surface on which sources and receivers are distributed.

All points in the subsurface at which a wave originating from a source is reflected and reach a receiver at a certain time is referred to as the isochron for that time. Computing the surface integral of equation A.1 at all subsurface points is equivalent to smearing the magnitude of the time derivative of the recorded wave field U at each source-receiver pair along the

corresponding isochron surfaces at the respective recording times, scaled by the weight W (Figure A.10a). At the true reflector points, the back projected reflected waveforms interfere coherently and destructively elsewhere (Figure A.10b). This accumulates the back projected reflection energy along the reflecting structures (bright spots) and generates an image of the subsurface. The calculation of time derivative of U and the weight W is often omitted if the goal is solely to image structures and relative reflection strengths of the reflectors are not necessarily required.

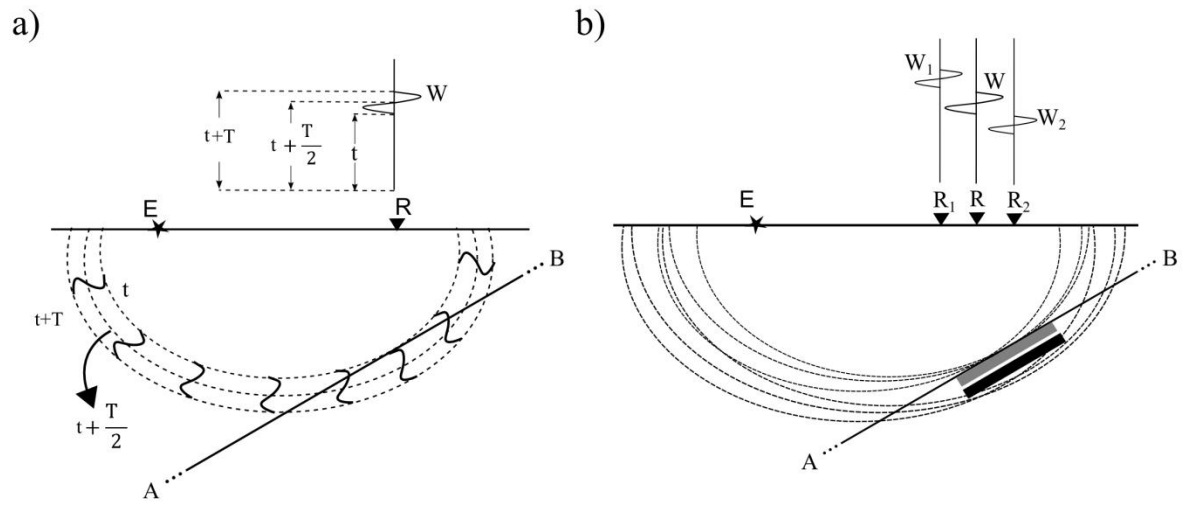

Figure A.10. Working principle of Kirchhoff pre-stack depth migration; a) seismic wave generated by a source E is reflected from a reflector AB and recorded at a receiver R as waveform W. W is back projected to the reflector AB by smearing the recorded wave-field along isochrons at respective recording times, b) reflector AB imaged by constructive interference of back projected reflected waveforms W, W_1 and W_2 which are recorded at the receivers R, R_1 and R_2 respectively. The black and grey solid rectangles represent positive and negative intensities formed by constructive interference of individual reflected waveforms.

KPSDM is the generalized and analytic approach to the heuristic “ruler and compass” seismic migration technique (Hagedoorn, 1954) for locating reflectors as envelope of equal travel time curves (Bleistein 1999). It is one of the most widely applied seismic imaging methods and has been successful in imaging subsurface with high structural complexities. Although an

alternative method, the wave equation pre-stack migration (WEM) generally produces images of higher quality, KPSDM has been popular (particularly over the course of last two decades) due to its lower computational resource requirements, being capable of working with irregular source receiver geometry and better imaging of the strongly dipping reflectors. Moreover, the technique can be applied to any arbitrary subsets of data which makes it preferable for target-oriented migration.

A.3.3 9HR profile

The 9HR profile (Tomek et al, 1997) is approximately 200 km long, starting at Klingenthal, 2.7km inside Germany in western Bohemia in the north-west to Horazdvice in south-western Bohemia stretching to Prachatice in southern Bohemia in the south-east (Figure A.11). The profile was originally aimed at imaging the subsurface of the Bohemian massif and crosses through three of its major Geological units, the Saxothuringian zone, the Tepla-Barandian unit and the Moldanubian.

EQUIPMENT	2 X SN 338HR, 192 Channels
SOURCE	- Dynamite - Average charge weight of ~ 20kg - Average drill hole depth of ~ 20m
RECORD LENGTH & SAMPLE INTERVAL	24s & 4ms
SHOTPOINT SPACING	200m
GEOPHONE SPACING	50m
RECEIVER SPREAD LENGTH	10km
PROFILE LENGTH	200km
TOTAL NUMBER OF SHOTS	678

Table A.1. Acquisition parameters of 9HR profile

The acquisition took place in two stages; first in 1991 and second in 1993-94. Dynamite sources were employed at 20 m deep drill holes in a split-spread geometry with maximum offset of 5 km of single vertical component receivers on each side of the shot point. The shot and geophone spacings were 200 m and 50 m, respectively. A total recording length of 24s

with a sampling interval of 4ms was used.

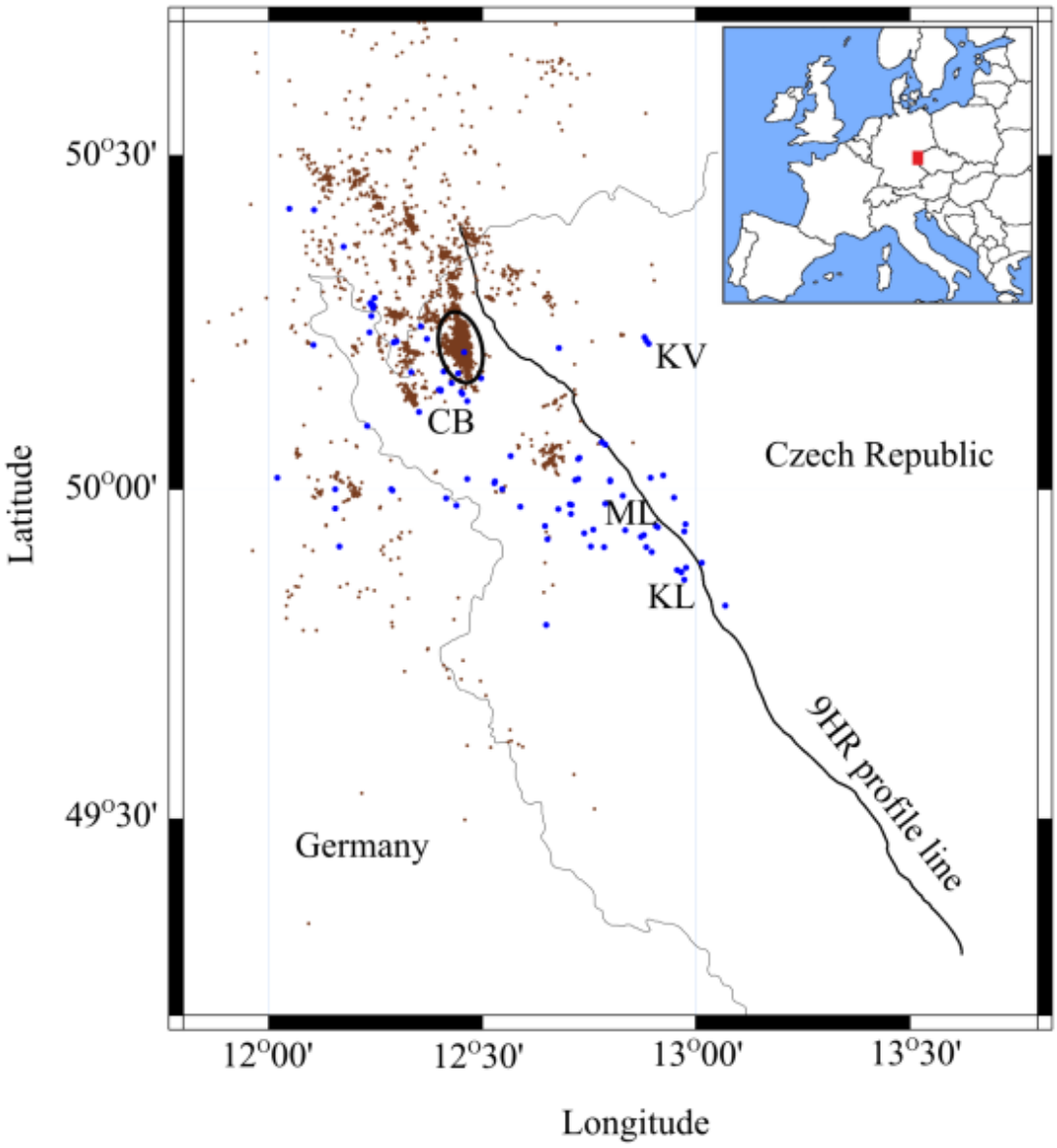

Figure A.11. Map of the study area showing the 9HR profile line (1991 part) along with the regional seismicity during 1991-2011 (brown dots) and fluid escape points (blue dots) at the western Eger Rift. Black ellipse represents the swarm area; major gas escape centers are marked as CB (Cheb Basin), ML (Mariánské Lázně), KV (Karlovy Vary), and KL (Konstantinovy Lázně).

The 9HR profile passes by the main focal zone of the regional swarm seismicity at a distance of about 4 km; then it runs directly through two of the four major degassing fields, the

Mariánské Lázně and Konstantinovy Lázně gas escape centers. The location of the profile is therefore well-suited to study the geodynamically active subsurface below these observations. It was originally processed with post-stack migration technique (Tomek et al., 1997). Below the swarm earthquake area, an upwelling of the Moho was seen along with indications of basaltic intrusions (Figure A.12). Additionally, a number of reflectors could be identified in the upper mantle at depths of 35, 42 and 56km that coincide with these observations. However, the migrated section did not present any significant feature(s) that may be directly related to the fluid or earthquake activity.

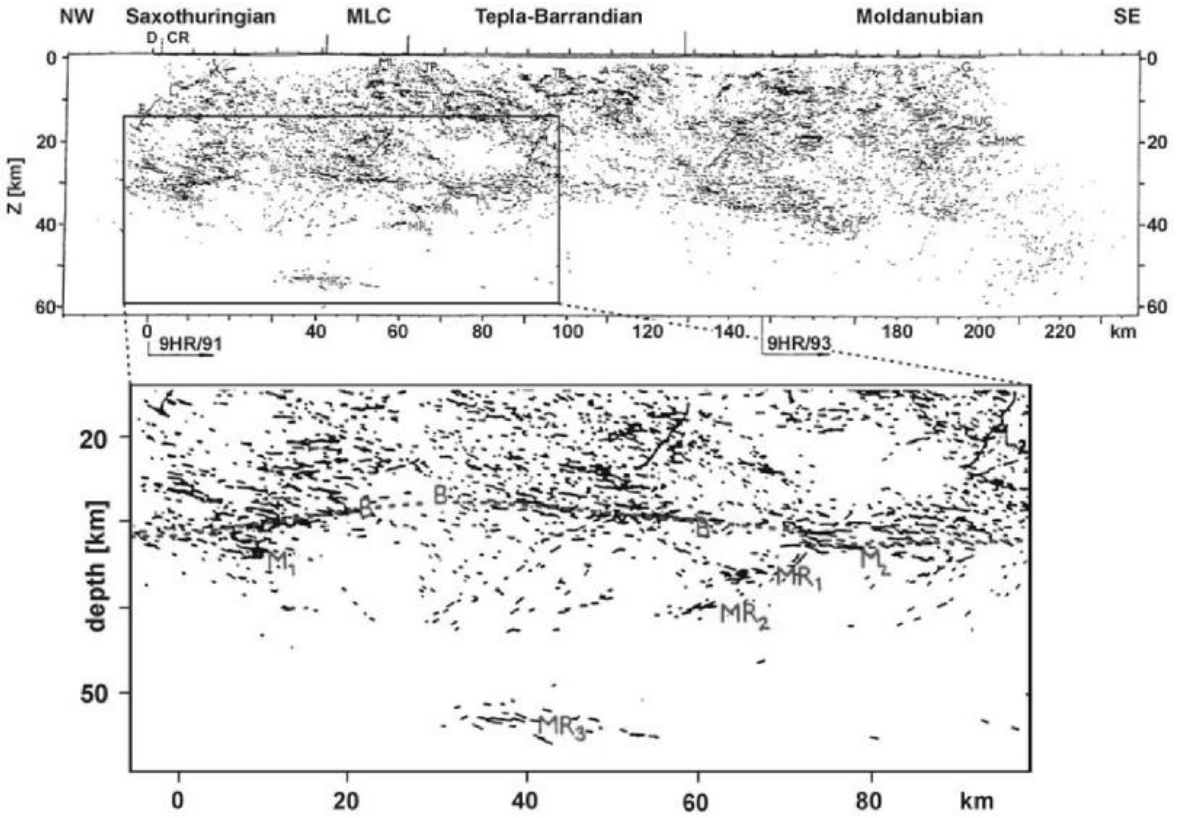

Figure A.12. Post-stack migrated section of 9HR profile and its main interpreted features. (Tomek et al., 1997)

The 1991 part of the 9HR profile (~140km from the north-western end) is close to the swarm earthquake and fluid observations. This part is reprocessed here with modern techniques and imaged using Kirchhoff pre-stack depth migration. Since pre-stack migration is more

appropriate for the crystalline crust in the area, it is expected to provide new information over the post-stack method used previously. The subsurface reflectivity distribution is then correlated with the earthquake hypocenters and fluid escape points to understand the geodynamic activity of the western Eger Rift area.

A.3.4 Data pre-processing

The 9HR profile data is provided in SEG-Y format files that contain 678 shot records from the whole profile (i.e. both 1991 and 1993-94 parts). The data is first converted to Seismic Unix format which is the standard format used for all data pre-processing and migration procedures. The coordinates of the source and receivers are provided separately which are inserted into the trace headers at this stage. The data is finally sorted in common shot gathers and individual shot gathers from the 1991 part of the profile are extracted and saved into separate files.

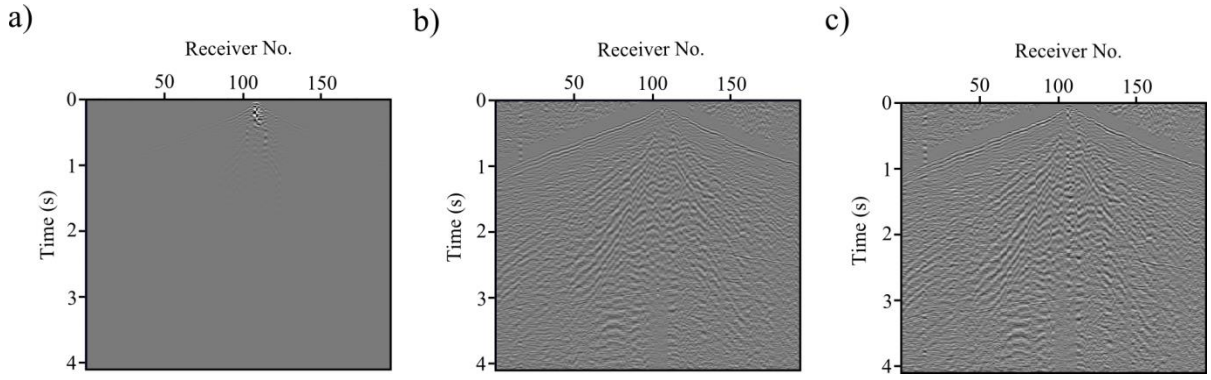

Figure A.13. a) A raw shot gather of 9HR profile, b) same shot gather after application of AGC, c) same shot gather after application of AGC and trace normalization.

Each shot gather consists of records at 192 receivers. In an individual raw shot gather, at far offsets and late arrival times, the recorded signal is too weak relative to that at near offset and early arrival times owing to different attenuation effects (Figure A.13a). To correct this, automatic gain control (AGC) is first applied to the record at each receiver. At each time, the RMS value of the samples over a 0.4s window is calculated. A gain curve is then constructed

with the inverse of these RMS values as function of the recording time. The gain curve is then applied to the record to perform the AGC (Figure A.13b). Next, the record at each receiver of the AGC corrected shot gather is divided by its maximum sample value to perform trace normalization (Figure A.13c). The signal is then visible over the whole length of 24s at all receivers.

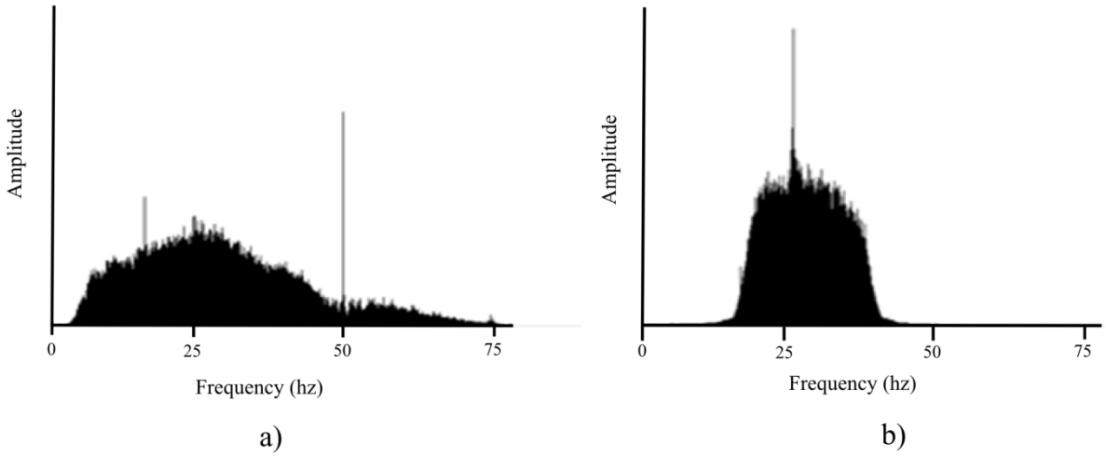

Figure A.14. Frequency spectrum of a shot gather from the 9HR profile, a) before and b) after band pass filtering (15-20-35-40 Hz).

Each AGC-corrected and normalized shot gather is first inspected for its suitability to be used for migration, given a quality rating and any prominent reflections if visible is noted (Figure A.15). The data quality is in general very good except for only a few shot gathers that are too noisy or corrupted and unusable for further processing. The primary noises present in the shot gathers are the surface waves and the direct wave (Figure A.16). The amplitude spectrum of the 9HR data shows a frequency range of 4-80 Hz with a dominant frequency of 25Hz (Figure A.14). In order to get rid of the low frequency surface waves and the high frequency noises, a band pass filter is applied at 15-20-35-40 Hz (Figure A.17). This removes the noises successfully while preserving the reflections along the whole length of the shot records (Figure A.16-A.17). The first arriving direct wave and noises appearing at earlier times are then eliminated by top muting (Figure A.18).

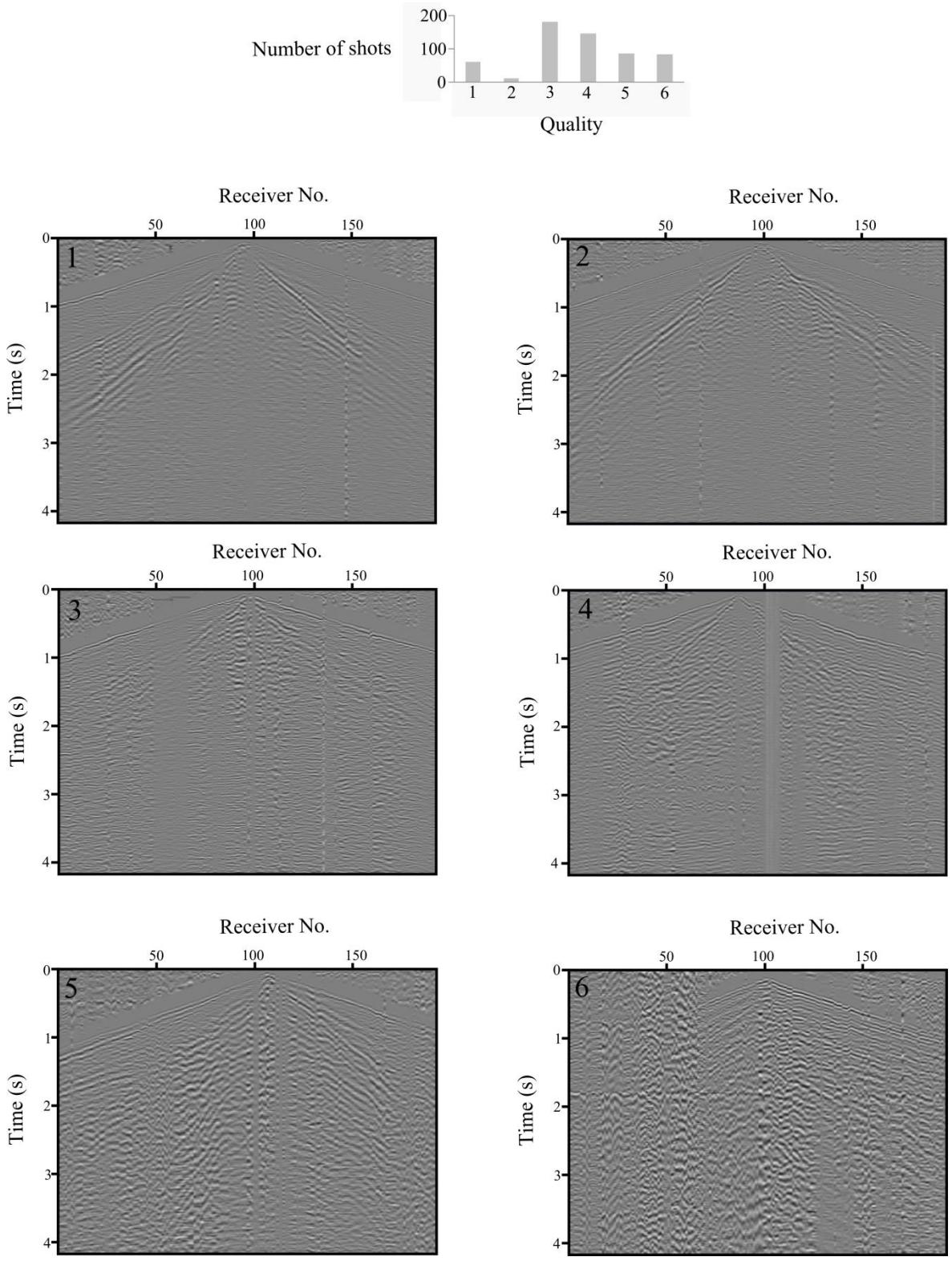

Figure A.15. Example raw shot gathers (AGC and trace normalization applied) of 9HR profile with different qualities.

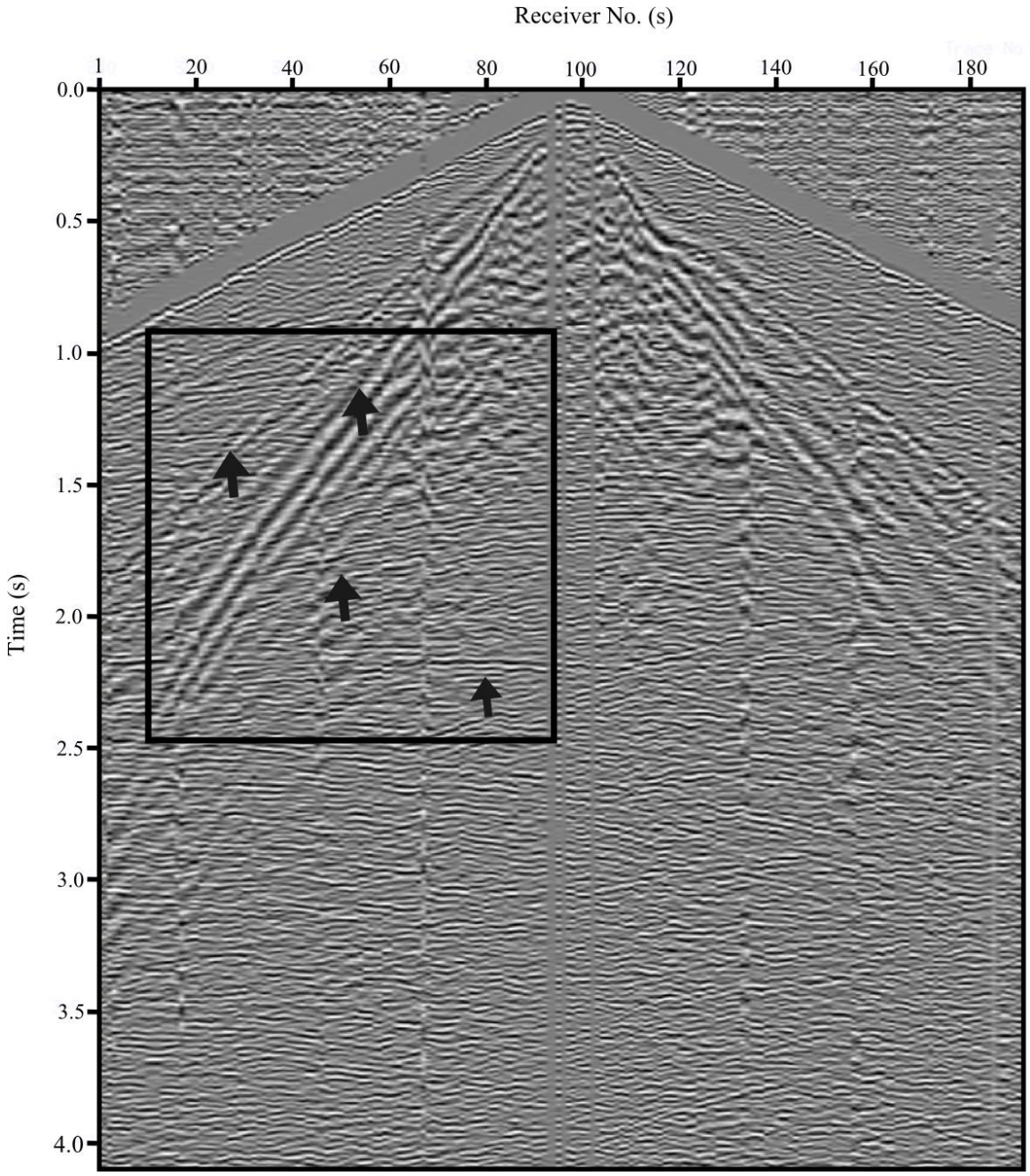

Figure A.16. Example raw shot gather of 9HR profile (with AGC and trace normalization applied). Arrows mark some of the prominent reflections.

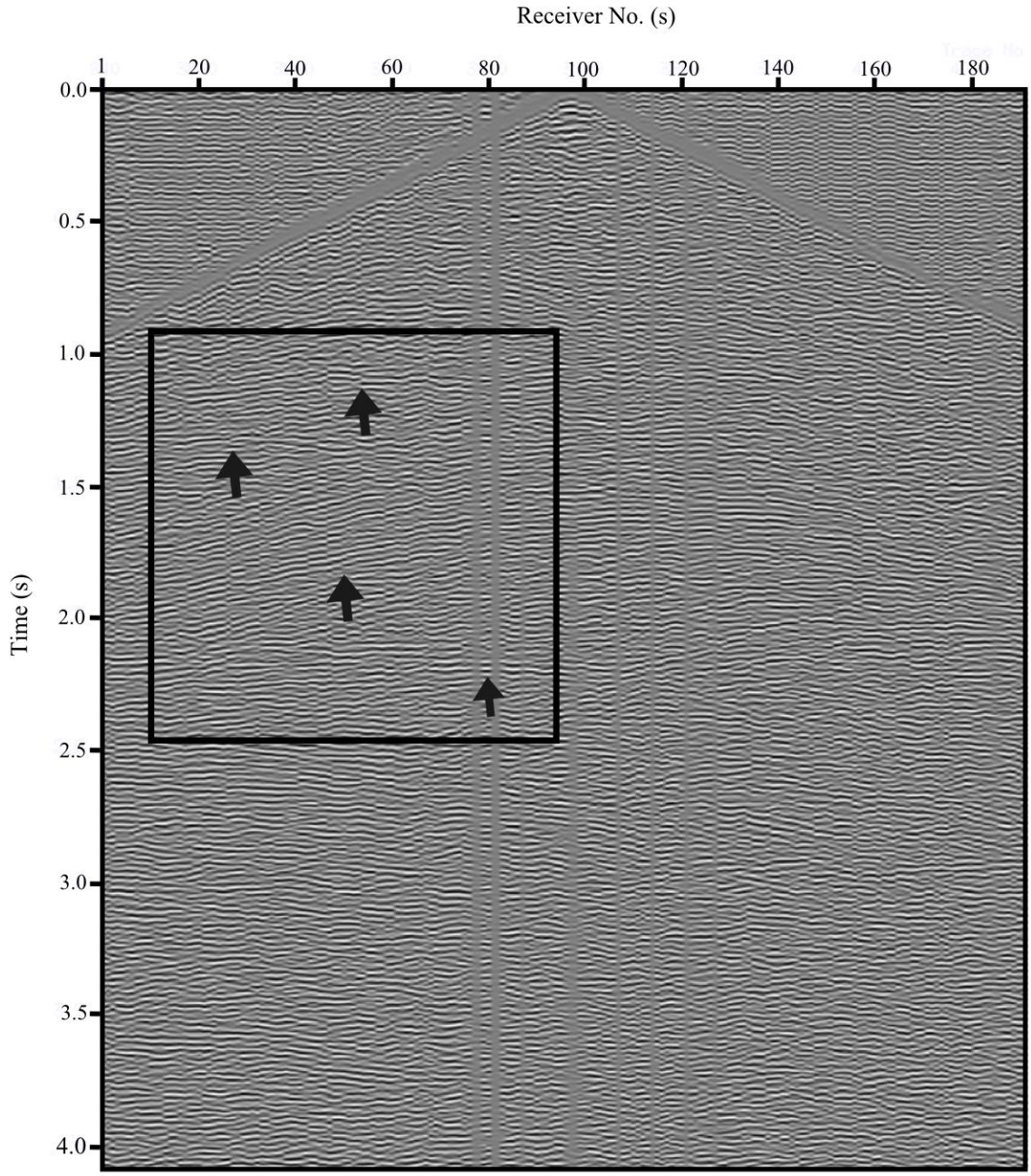

Figure A.17. Same shot gather of Figure A.16 after band pass filtering (15-20-35-40 Hz). Arrows mark the same prominent reflections seen in the raw shot gather.

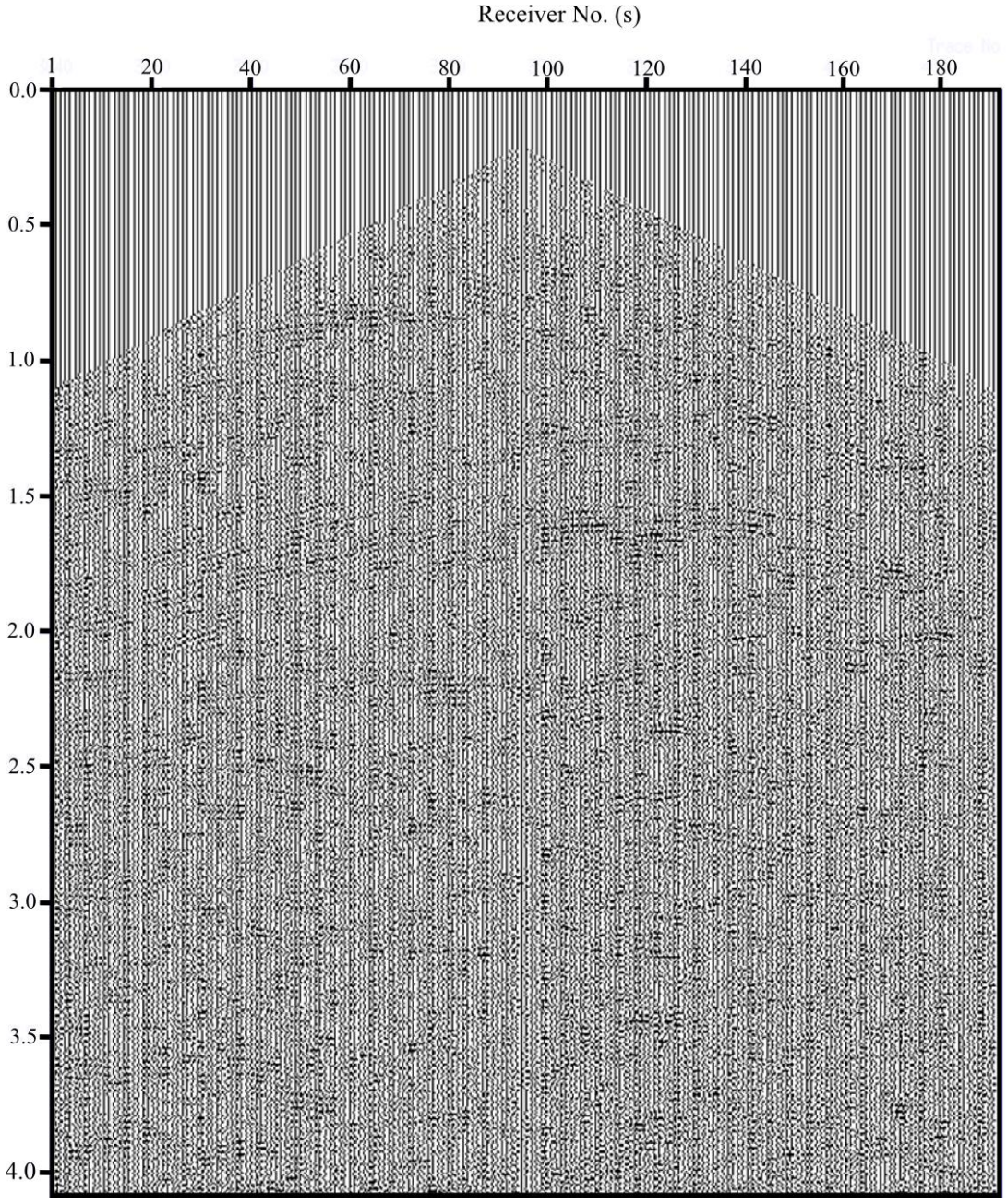

Figure A.18. Same shot gather of Figure A.16 after band pass filtering and first arrival muting.

A.3.5 Migration of the whole profile (1991 part)

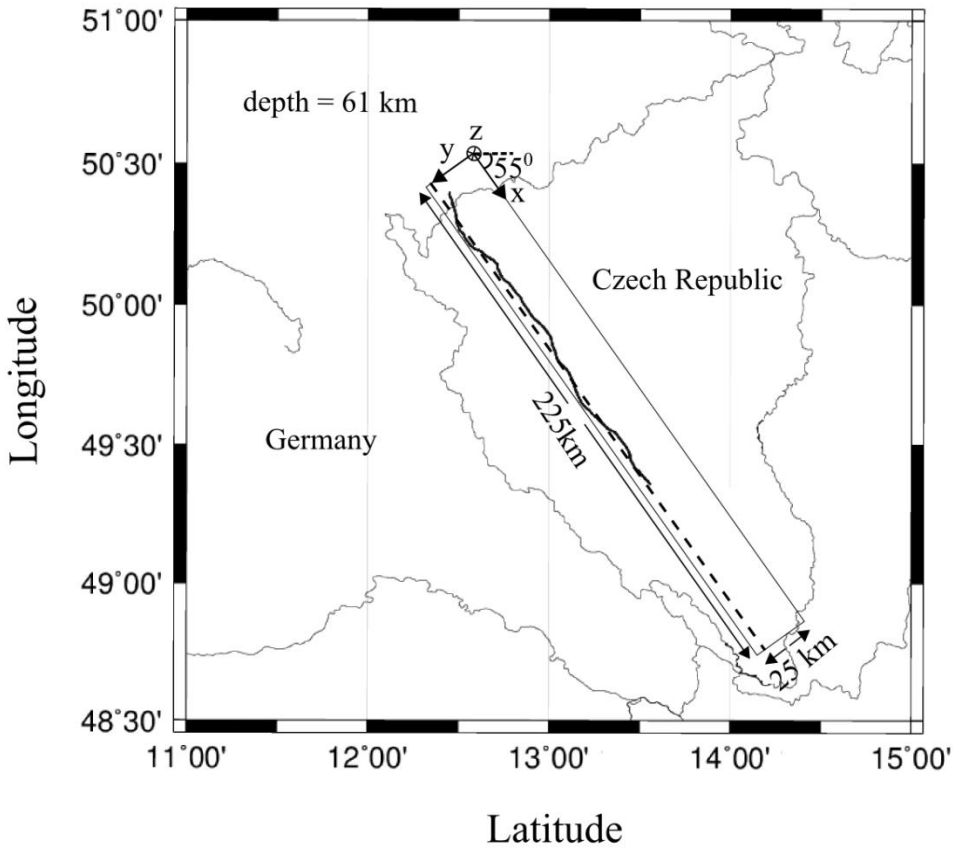

Figure A.19. The grid used to perform Kirchhoff pre-stack depth migration of 9HR profile. The dashed line represents the location of the vertical slice of the final 3D migrated section which is taken as the reflectivity image below the profile.

To migrate the 9HR profile, a 3D grid is defined with width (x) 25km, length (y) 225km and depth (z) 61km and uniform grid spacing of 250m along all axes (Figure A.19). The length of the grid is chosen such that the 1993-94 part of the profile can be adopted as well if required in the future. Velocities are assigned to each point of this grid according to the velocity model to construct a velocity grid. The source and receiver coordinates are transformed from the global coordinate system (UTM) to the local grid coordinates. For each of the source and receiver locations within the velocity grid, the first arrival times to every grid point are computed. The isochron for a source and receiver pair at a certain time can be then obtained

by finding all grid points at which the sum of first arrival times from the source and the receiver equals that time. The migration of the record at a receiver for a source is then performed by smearing the amplitude of the record along the isochrons of the source and the receiver pair at the respective recording times.

A.3.5.1 Velocity Models

Three velocity models are investigated for migration of 9HR profile; a constant velocity of 6 km/s, a 1D velocity model from the nearby refraction seismic profile CEL09 (Hrubcová et al., 2005) and another 1D velocity model by Málek et al. (2005) that is used by the local seismological network (WEBNET) to locate the swarm seismicity.

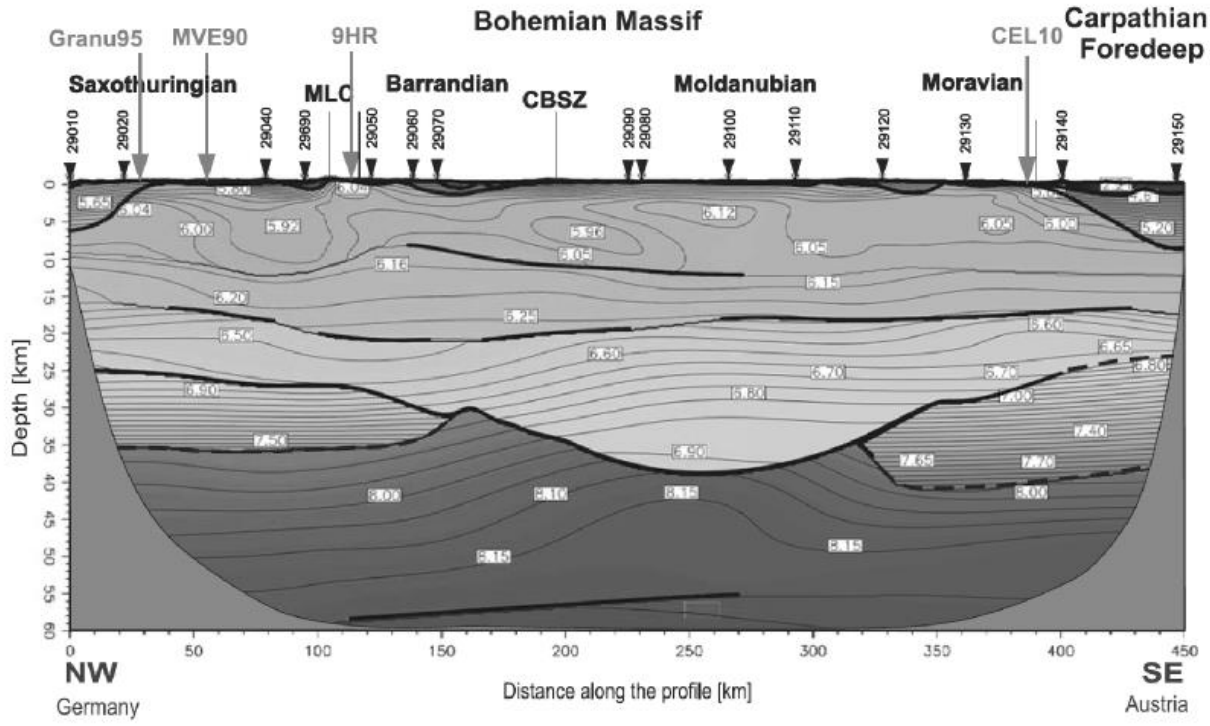

Figure A.20. 2-D model of the P wave velocity below the CEL09 profile. Bold lines mark boundaries constrained by reflections and well-constrained interfaces in the uppermost crust; dashed bold lines mark layer boundaries where no reflections were observed. Thin lines represent velocity isolines spaced at intervals of 0.05 km. MLC: Maria´nske´ La´zneˇ Complex, CBSZ: Central Bohemian Shear Zone. (Hrubcova 2005)

The NW-SE oriented refraction and wide-angle reflection profile CEL09 was part of international seismic refraction experiment Central Europe Lithospheric Experiment Based on Refraction 2000, CELEBRATION and was aimed at studying the structure of the Bohemian massif (Figure A.2). The velocity model (Figure A.20) is based on tomography and two-dimensional trial-and-error forward modeling of P and S waves of the first 450km of the profile that starts in the Saxothuringian and ends at the contact of the Bohemian Massif with the Carpathian Foredeep. This subset of the CEL09 comprises of 20 explosive shots with average distance between the shots of 30 km with a station spacing of 2.7 km. The northern part of the profile intersects 9HR profile and a 1D model (Figure A.22a) is extracted from the 2D velocity model at this intersection point to be used for the migration of the 9HR profile.

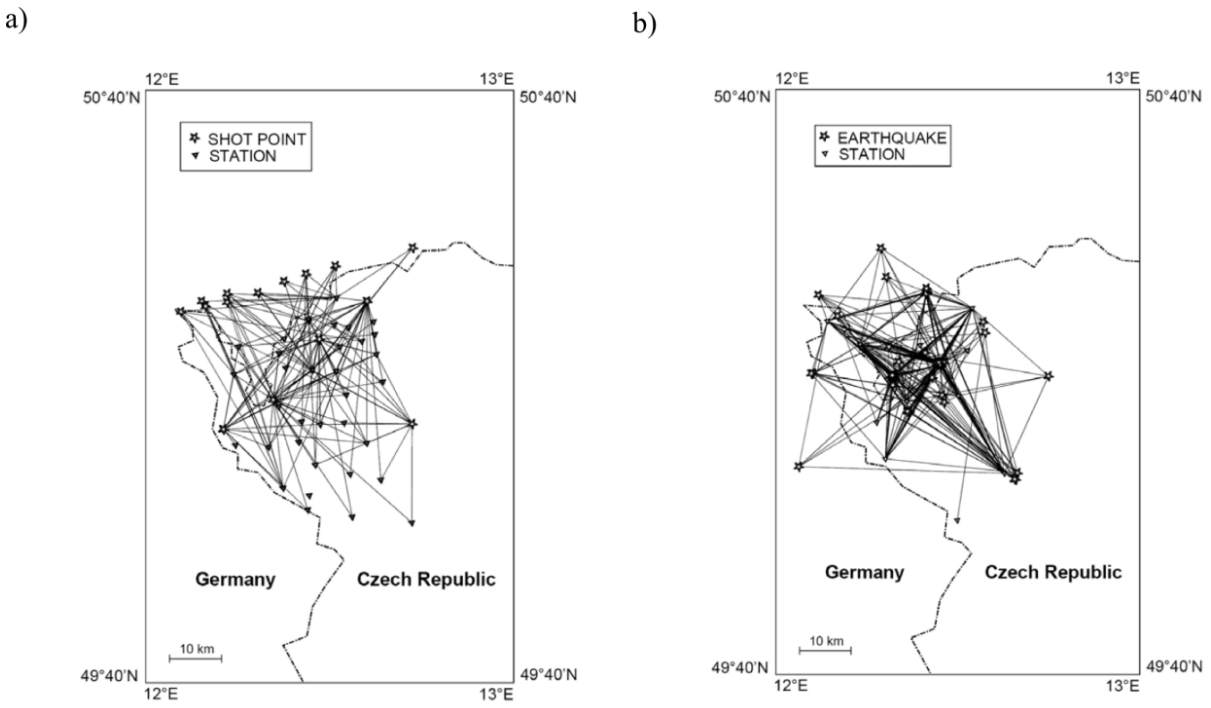

Figure A.21. Source (stars) and receiver (inverted triangles) locations for the datasets used to derive the Malek et al. (2005) velocity model; a) controlled shots and digital stations; b) micro-seismic events and the WEBNET stations. (Malek et al., 2005)

The Malek et. al (2005) velocity model is obtained by joint inversion of two independent datasets. The first dataset comprises of 181 P_g-wave travel times obtained from record of 15

controlled shots of seismic profiles A/89, B/89, C/91, D/91 and MVE/90 at 34 digital stations deployed at various epicentral distances and azimuths in 1989−1991 (Figure A.21a). The second dataset comprises of 424 P and 320 S wave arrival times of 65 local micro-earthquakes recorded by nine seismic stations of the WEBNET network in the period 1996−1999 (Figure A.21b).

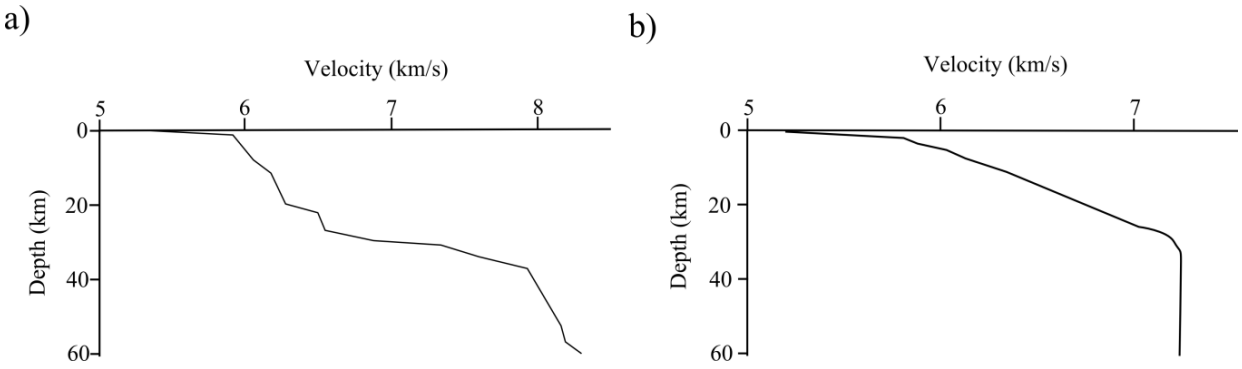

Figure A.22. a) Velocity model from refraction seismic profile CEL09, b) Velocity model from Malek et. al. (2005).

To fit the 1D models to the 3D velocity grid v(x, y, z), velocity values at different depths at the interval of the grid spacing of 250m are first calculated by linear interpolation. The velocity value at each depth is then assigned to all grid points at that depth.

A.3.5.2 Travel time computation

The first arrival times from the sources and receivers to each grid point are computed using an eikonal solver by Podvin and Lecomte (1991). This involves positioning a point seismic source at a source or receiver point within the velocity grid and use a finite difference scheme to calculate first arrival times to each grid point by numerical solution to the eikonal equation,

$$(\nabla t)^2 = s^2$$

Where t(**r**) and s(**r**) are the arrival time of a wave front and the slowness of the medium respectively, at point **r**.

The first arrival time grids $t_E(x, y, z)$ and $t_R(x, y, z)$ give first arrival times from the source E and receiver R respectively to each grid point (x, y, z) and are referred to as travel time tables. The sum of the first arrival times $t_{ER} = t_E + t_R$ at a grid point gives the two way travel time (TWTT) from the source E to that point and back to R. The grid points with a certain TWTT forms the isochron surface for the source and receiver pair E and R for that time (Figure A.23). In contrast to the uniform velocity grid, the grid spacing of the first arrival time grids is only 2500m along y. This reduces the computation cost of migration but is sufficient to detect any major reflectivity variation in the y direction which is perpendicular to the profile.

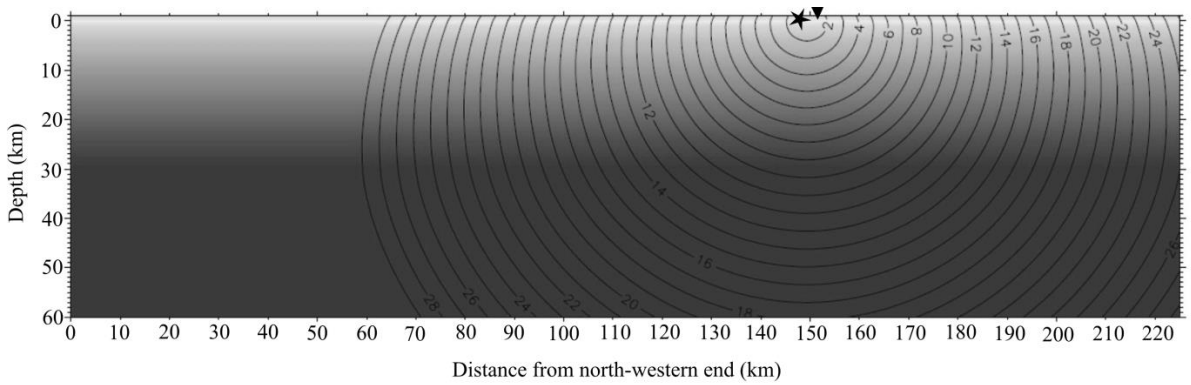

Figure A.23. P-to-P reflection isochrons for a source (star) and receiver (inverted triangle) pair of 9HR profile plotted on top of the Malek et al. (2005) velocity model.

A.3.5.3 Migration

Kirchhoff pre-stack depth migration is implemented on each pre-processed shot gather of the 9HR profile separately. The migration grid m(x, y, z) has same grid spacing as the travel time grid along x and y but the spacing is reduced to 25m along z in the vertical direction to avoid aliasing artifacts. The travel time values at the new grid points are computed from the pre-calculated travel time tables by linear interpolation.

To migrate the record of the shot E at the receiver R, the absolute value of the record at time t is smeared along the isochron at time t i.e. at all points of the migration grid m(x, y, z) that has TWTT t (Figure A.23). The above smearing process is repeated for records at every receiver

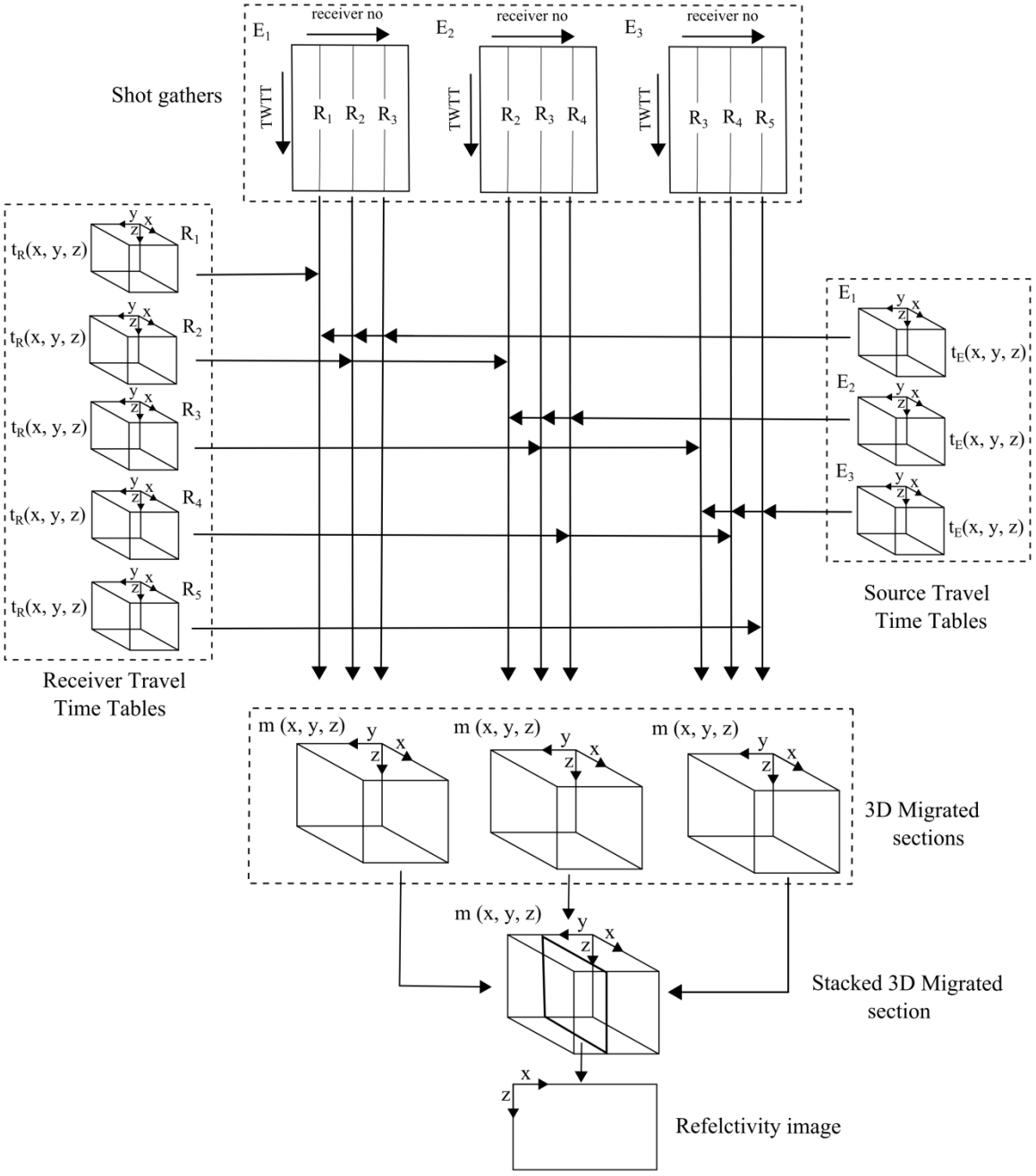

Figure A.24. Work flow for Kirchhoff pre-stack depth migration using three shot gathers each with records at three receivers R_1-R_2-R_3, R_2-R_3-R_4 and R_3-R_4-R_5. The shots E_1, E_2 and E_3 are coincident with the receivers R_2, R_3 and R_4 respectively.

of the shot E to obtain the 3D migrated section for the shot (Figure A.25). 3D migrated sections from all shots of the 1991 part of the 9HR profile are thus computed separately.Finally, all the individual 3D migrated sections are stacked together to obtain the 3D migrated section of the whole profile. A vertical slice of this final 3D migrated section

along the profile line at y = 20 km (Figure A.19) is taken as the reflectivity image below the 9HR profile.

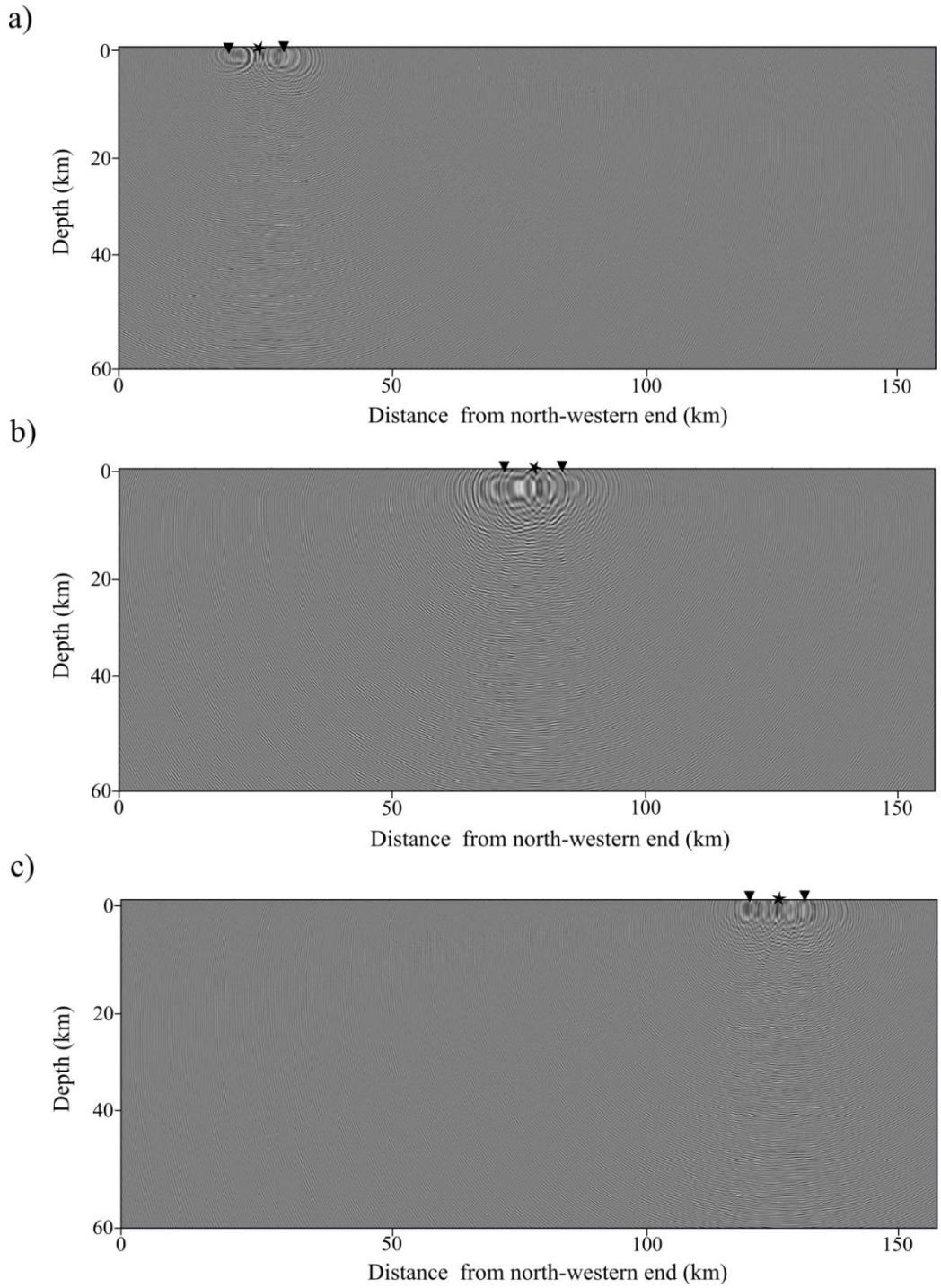

Figure A.25. Migrated sections of three shots of the 9HR profile at its a) northern end, b) middle and c) southern end. The star represents source and the inverted triangles represent last receivers of the receiver spread on either side of the source.

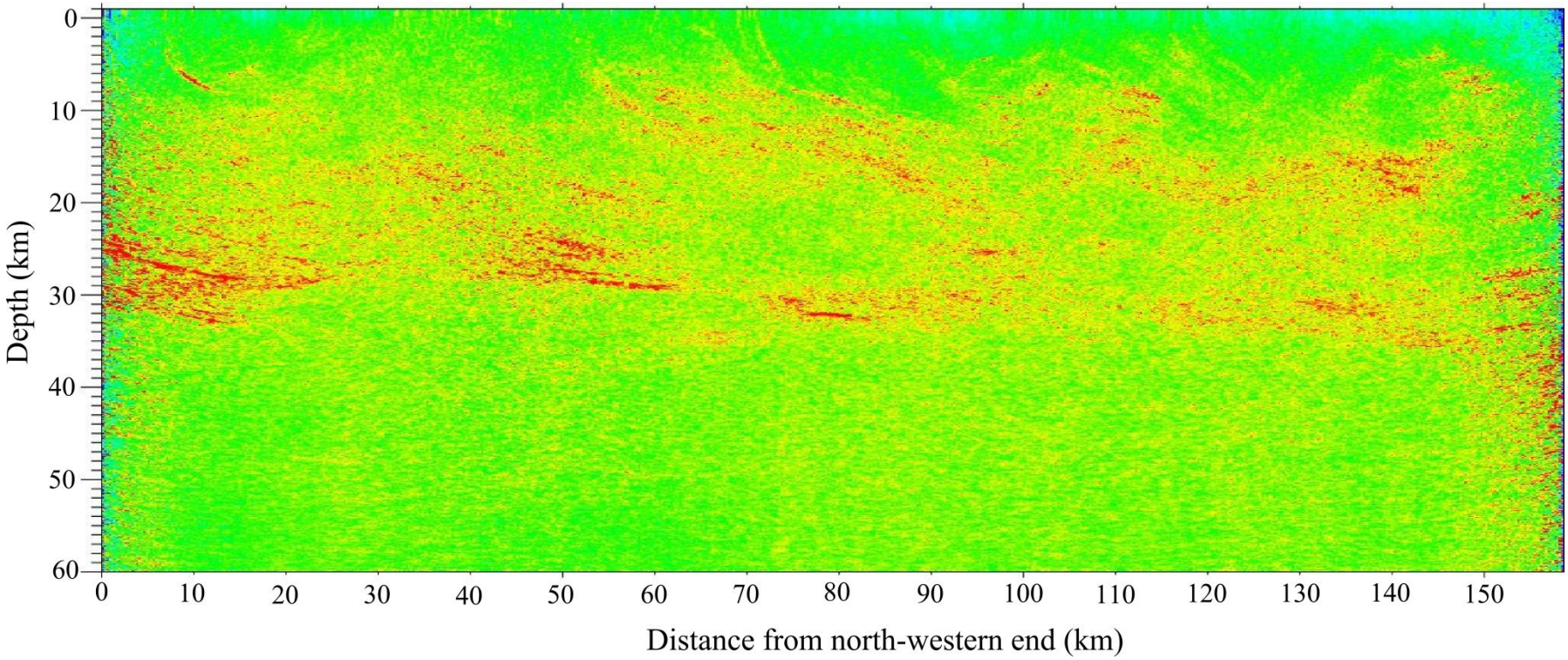

Figure A.26. Migrated section of 9HR profile using constant velocity of 6km/s

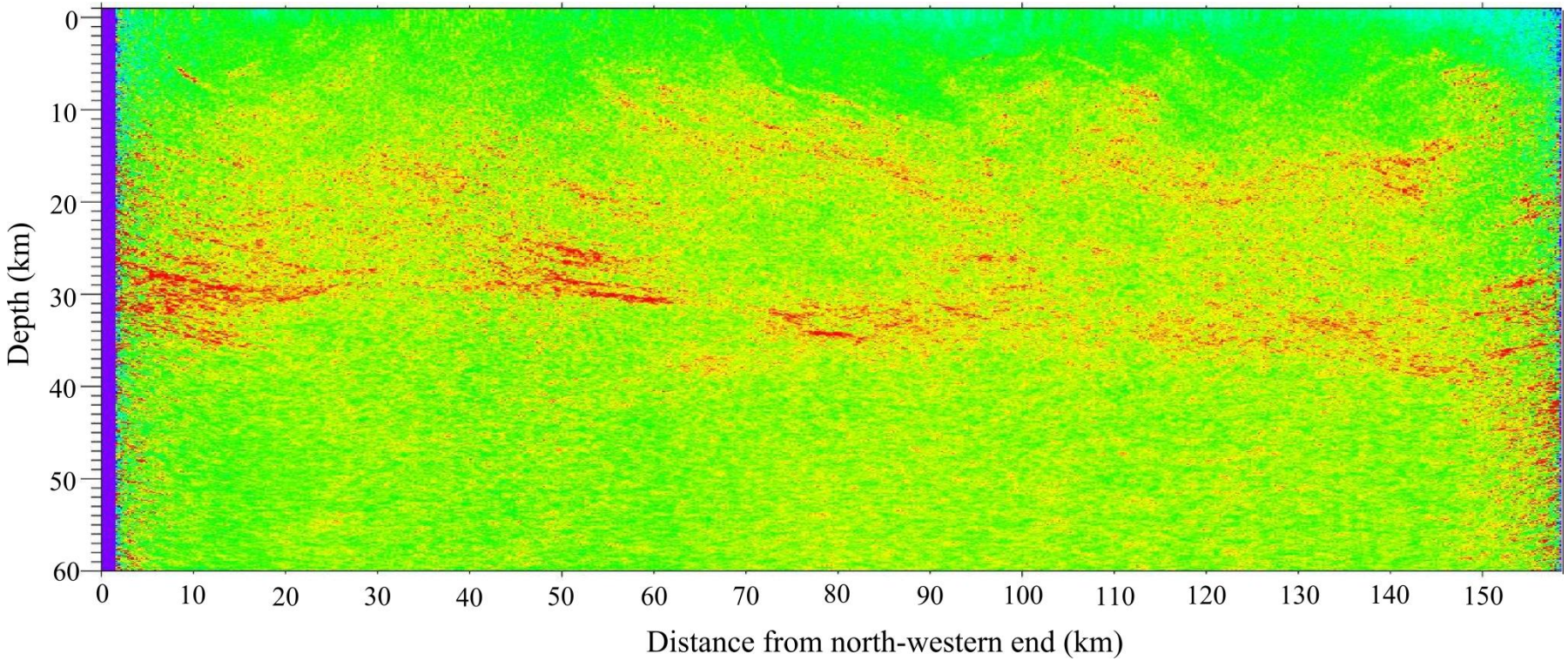

Figure A.27. Migrated section of 9HR profile using velocity model from the CEL09 refraction seismic profile.

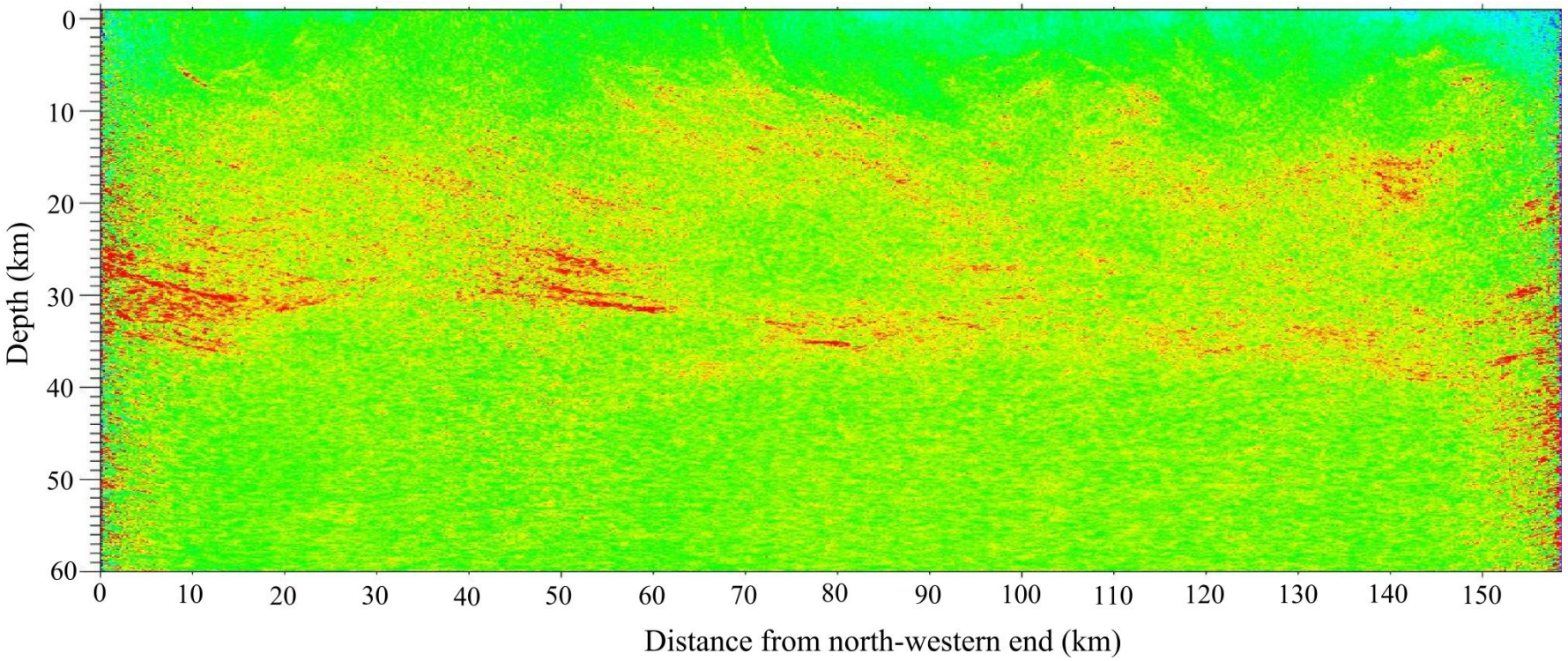

Figure A.28. Migrated section of 9HR profile using velocity model of Malek et. al. (2005).

Migration of the 9HR profile is performed separately using all three velocity models (Section A.3.5.1). The reflectivity images (Figure A.26-28) do not vary a lot for different velocity models with only nominal differences in reflector depths. Since, the reflectivity distribution is to be investigated against the regional seismicity, only the image obtained from the velocity model of Málek et al. (2005) is chosen for the later analysis. Then, a direct comparison of the reflectivity and the seismicity is justified because the same velocity model is used for reflection imaging and locating the earthquakes.

A.3.6 Migration of subset of 9HR profile at the swarm area

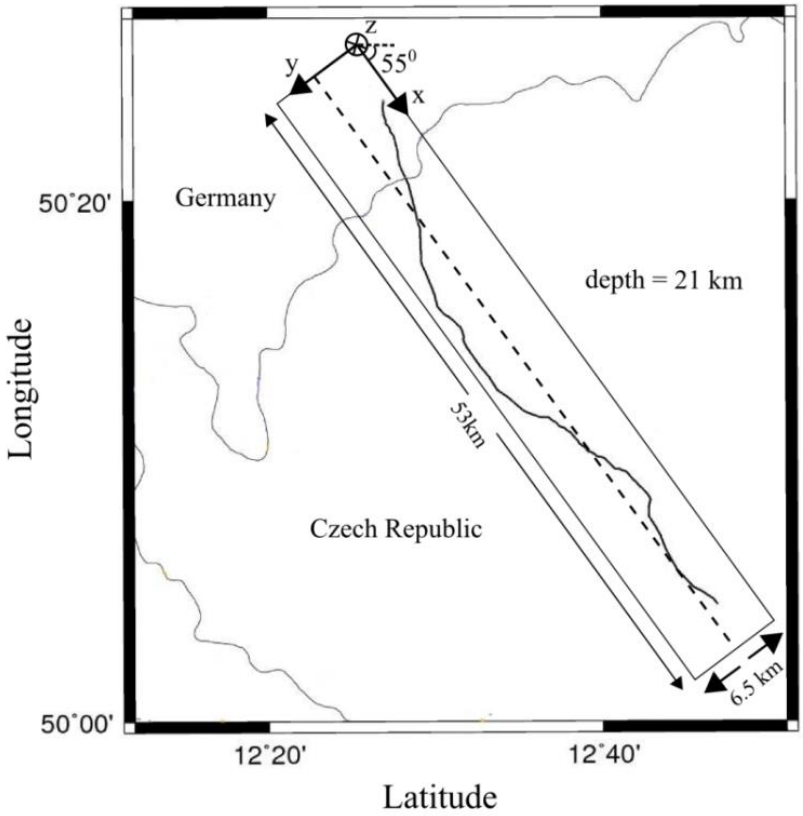

Figure A.29. 9HR profile subset close to the swarm area and the grid used to perform Kirchhoff pre-stack depth migration on it. The dashed line represents the location of the vertical slice of the final 3D migrated section which is taken as the reflectivity image below the profile subset.

In addition to migration of the whole 9HR profile (1991 part), a subset of it at the swarm area is separately migrated (KPSDM) with a denser grid in order to inspect the reflectivity of the shallow subsurface below the swarm earthquake area in higher resolution in greater detail. This subset is up to ~40 km from the north-western end of the profile that passes close to the swarm earthquake area.

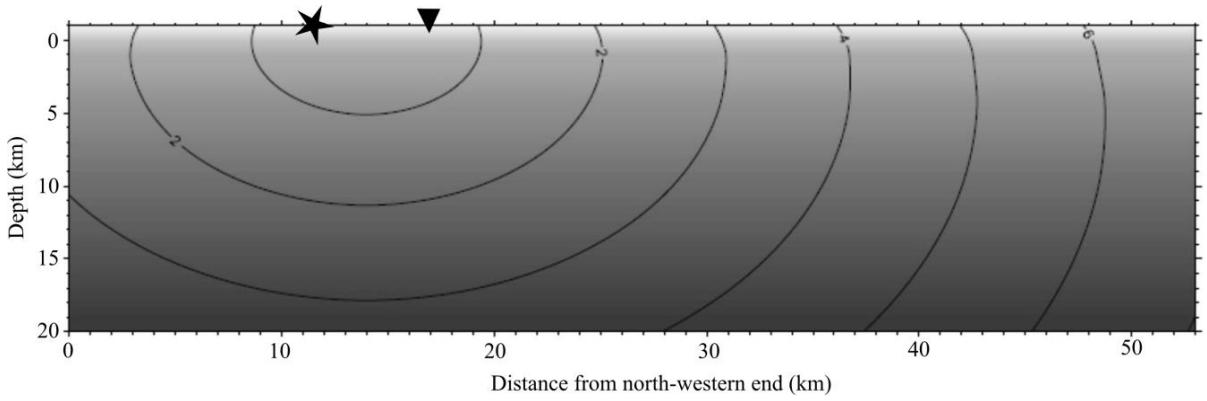

Figure A.30. P-to-P reflection isochrons for a source (star) and receiver (inverted triangle) pair of the 9HR profile subset close to the swarm area plotted on top of the Malek et al. (2005) velocity model.

In this case, the migration grid is defined with width 6.5km, length 53km and depth 21km (Figure A.29). The grid spacing for the velocity grid is uniform along all axes at 100 m, for travel time grid 650m along y and 100m along x, z and for the migration grid 100m along x, 650m along y and 5m along z. Only the Malek et al, (2005) velocity model (Figure A.22b) is used. Travel time tables are computed for each source and receiver of the chosen subset following identical procedure (Section A.3.5) as in case of the whole profile (Figure A.30). The absolute value of the amplitude of the recorded reflected wave-field at each source-receiver pair is then smeared along the isochron surfaces at respective recording times to perform Kirchhoff pre-stack depth migration. For each shot, the migration is performed separately and the individual migrated sections are then stacked to obtain the final migrated section. The vertical slice of the stacked 3D migrated section along the profile line at y =

3250m (A.29) is taken as the image of reflectivity distribution below the 9HR profile subset.

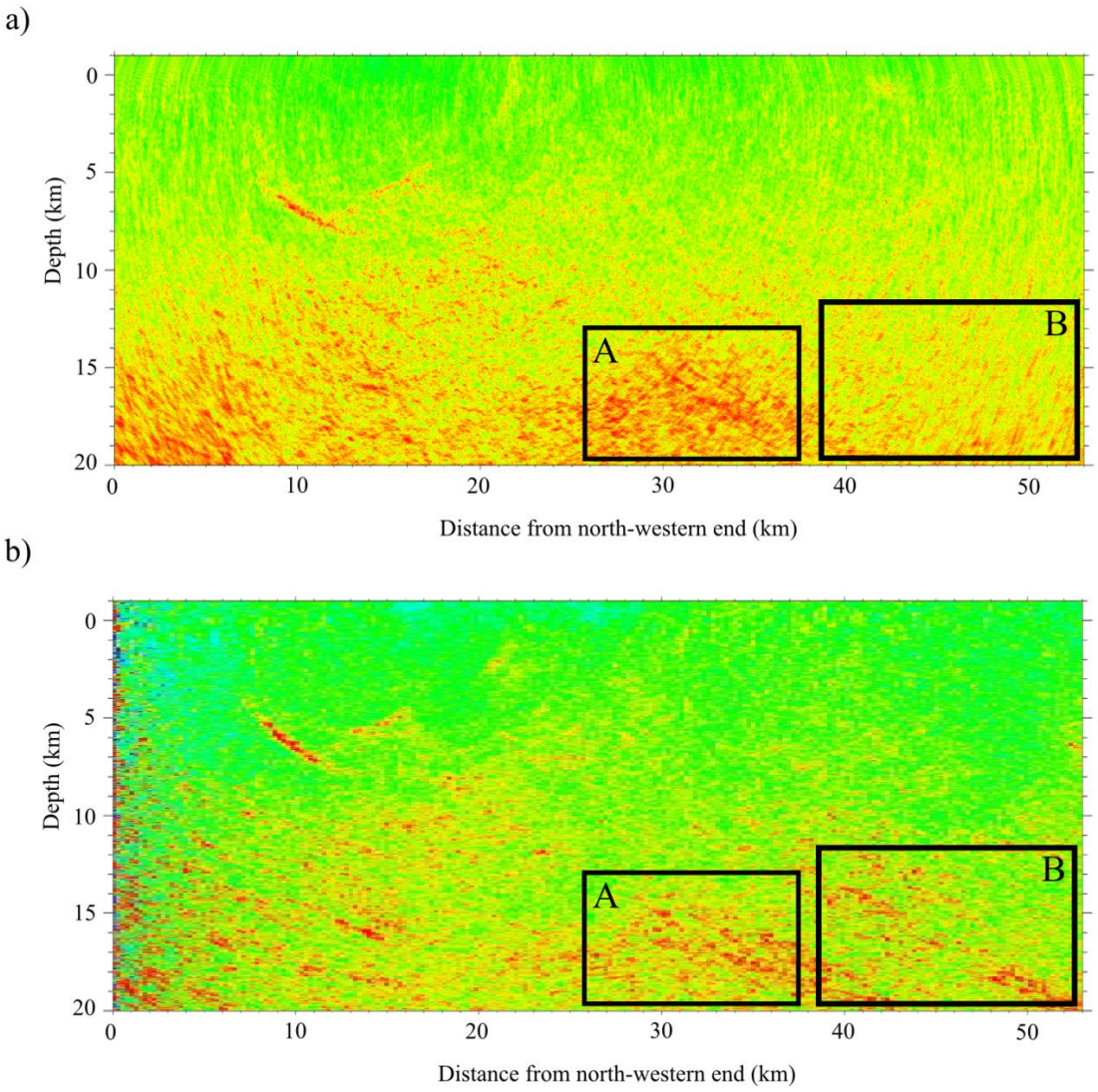

Figure A.31. a) Migrated section of the 9HR profile subset close to the swarm area using the velocity model of Malek et. al. (2005). b) Reflectivity image of the same part of the crust from the migrated section of the whole 9HR profile (using the same velocity model).

The reflectivity image of the subset does show reflectors in higher resolution due to denser grid spacing (Figure A.31, rectangle A). However, it does not provide any significantly new information on the subsurface reflectivity. Instead, as compared to the image from the whole profile, some reflectors are absent (Figure A.31, rectangle B) due to lesser source and receiver coverage. This image is thus not used directly in any of the further analysis.

A.3.7 Subsurface reflectivity along 9HR profile

In the reflectivity images, the red-yellow colors represent points of high reflectivity and the green with low reflectivity. The reprocessed seismic reflectivity image from the 9HR profile (Figure A.32a) reveals a strongly reflective upper and lower crust with a number of distinct reflective zones. The Moho can be identified as the bottom of the reflective lower crust at depths of about 29-40 km which agrees with the reflective lower crust obtained by Hrubcová et al. (2005, 2013) from refraction and micro-earthquake waveform modeling studies. The shallower Moho is observed at a distance between 20 and 40 km along the profile with an updoming to a depth of around 29 km. This is in good agreement with the results obtained from receiver functions (Geissler et al, 2005). No prominent reflector can be observed in the upper mantle as well as in most parts of the profile from the surface down to a depth of approximately 3-4 km. However, the latter is caused by the generous muting of the first arrivals and lack of a reliable and detailed near-surface velocity model.

Directly below the main focal zone of regional seismicity, two distinct reflectors dipping at -20^0 and 20^0 from horizontal (bright spots A and B) are visible at a distance of 7-18 km along the profile at a depth of about 7 km (Figure A.32b). Another less pronounced reflector (bright spot C) is visible at a distance of about 17 km along the profile at a depth of 8 km. Furthermore, significant but more diffuse crustal reflectivity dominates the area at depths greater than 10 km along with occasional strong sub-horizontal reflectors at various depths. The upper edge of this diffuse reflectivity zone below the bright spots A, B, and C is indicated as D. Similar to that below the earthquake area, a diffusely reflective zone appears at a depth of 5 km immediately below the Mariánské Lázně and Konstantinovy Lázně gas escape centers (Figure 32a, 32c) with frequent strong reflectors. Its upper boundary is marked as Q. Also, beneath the Konstantinovy Lázně gas escape center, a prominent near-vertical reflector P can be observed dipping at 10^0 from vertical.

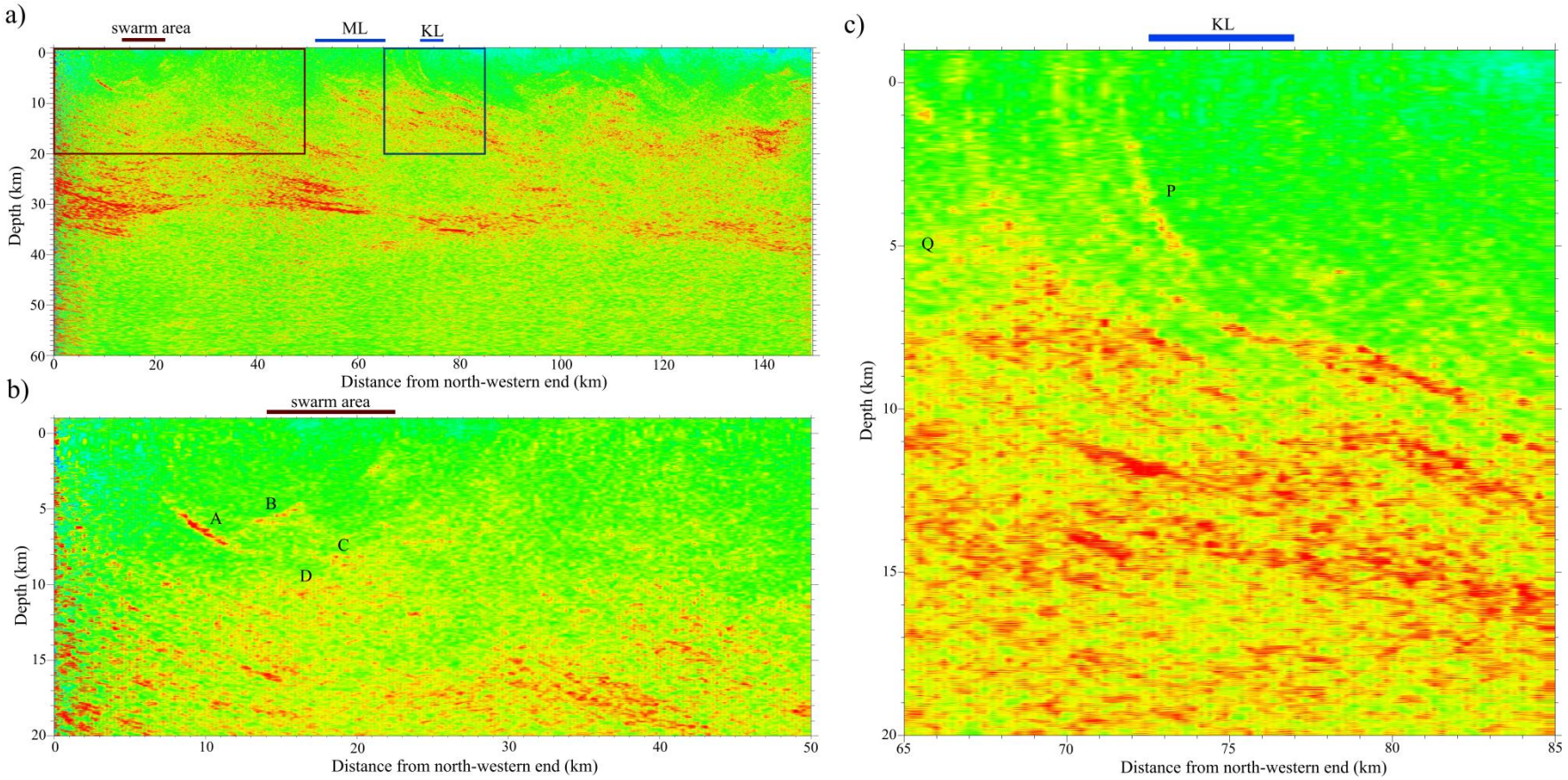

Figure A.32. a) Reflectivity image from the 9HR profile (using velocity model of Malek et. al. (2005). b) Enlarged part close to the swarm area (brown rectangle in (a)). c) Enlarged part near the Konstantinovy Lázně (KL) gas center (blue rectangle in (a)).

In comparison to the post-stack migrated image by Tomek et al. (1997), the reprocessed image shows a significant amount of new structural information. Majority of the features described above are not traceable in the former image. In fact, such high resolution is rarely achieved in the crystalline crust. In this regard the reprocessing was highly successful and provides ample scope for investigating the geodynamic activity in the study area in relation to the newly imaged reflectors.

A.4 Subsurface reflectivity and the geodynamic activity

Below to the imaging depth of 60 km, no reflection is detected from the mantle that may hint towards the existence of a magma body. However, Moho updoming is clearly observed in accordance with other imaging studies directly below the area where the majority of the regional seismicity is confined. The prominent multiple sub-horizontal reflectors at the upwelled Moho, together with the highly diffuse reflectivity arranged in an anticline structure immediately above it (Figure A.32a), possibly relate to the crustal deformation caused by the tectonic forces generated by the Moho updoming.

A.4.1 Subsurface reflectivity vs earthquake observations

Down to a depth of 10 km below the main focal zone of the regional seismicity, the crust is characterized by diffuse reflectivity with many strong sub-horizontal reflectors appearing at various depths (Figure A.33a). This reflectivity may be interpreted as a highly fragmented permeable middle and lower crust below a rather intact and less-permeable upper crust. If a fluid reservoir exists in the lower crust or upper mantle, then the fluids can rise up through such a strongly fragmented crust producing even more diffuse reflectivity, accumulate at some discontinuity at depth of 10 km (bright spot D in Figure A.33a) and develop a zone of over-pressured fluid (Figure A.33b). The presence of such a fluid trap is supported by the

occurrence of many gas escape points adjacent to the swarm area, which confirms active fluid flux below but none directly above it. The sub-horizontal reflectors within the diffusely reflective crust can be further interpreted as local interruptions of the ascending fluid at different tectonic fractures or lineaments, thereby producing higher reflectivity due to the presence of high-pressure fluid.

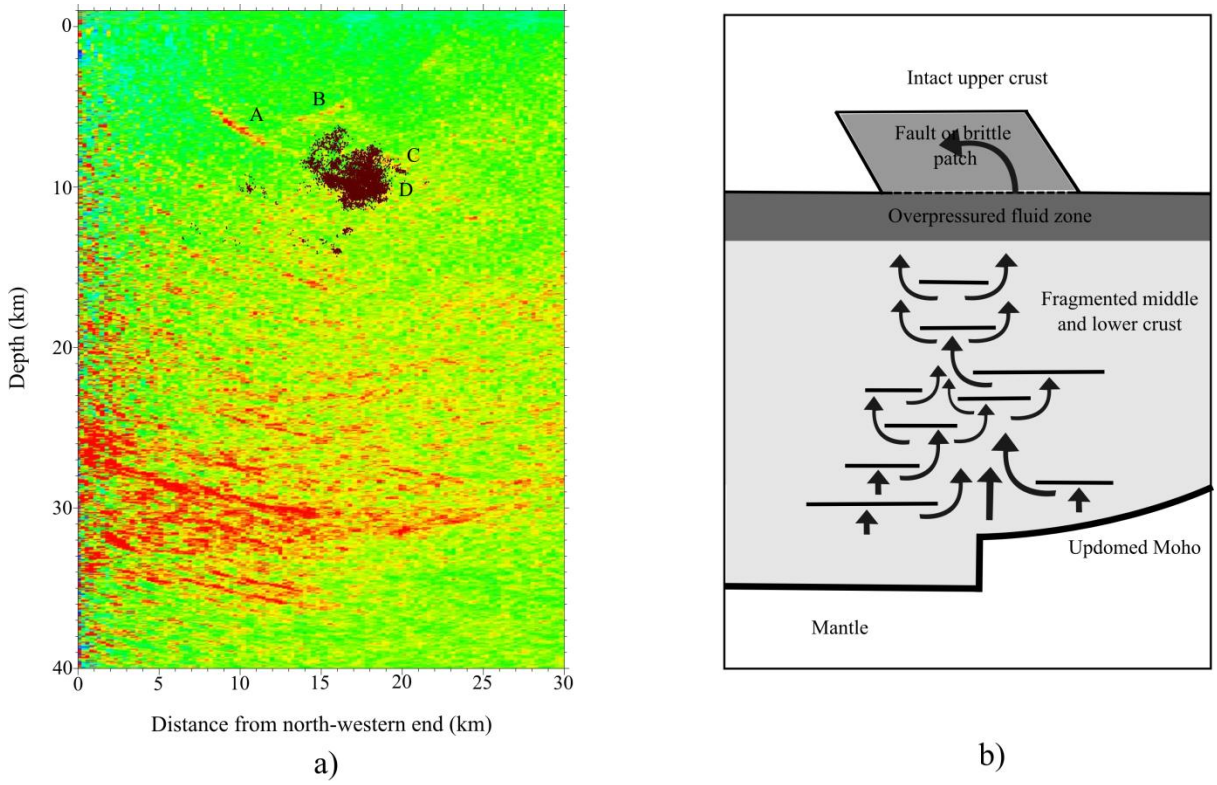

Figure A.33. a) The seismicity of the swarm area from year 1991 to 2011 (brown dots) plotted on top of the reflectivity image. b) Schematic sketch with the main interpreted features.

The hypocenters recorded during the recent massive earthquake swarms in the years 2000 and 2008 against the seismic reflectivity image shows that the swarm activity initiates at bright spot D with a sudden spontaneous upward movement of a large number of hypocenters (magenta dots in Figure A.34a, A.34e). Although the foci migration is rather complex in detail, a prevailing upward spreading is observed in both swarms (Fischer et al., 2014). Considering a supposed existence of an over-pressured fluid zone immediately below bright

spot D, it gives the impression of a sudden release of critically-pressurized trapped fluids into less permeable rocks above it by simultaneously fracturing and intruding into an overlying zone of weakness and redistributing the local stresses in the zone. Such a hypothesis linking pressurized fluids with the micro-earthquakes is in accordance with the observed influence of swarm activity on the fluid activity (Bräuer et al., 2008), models of swarm hypocenter migration in terms of fluid movement (Fischer et al., 2014) and numerical modeling of the swarms as diffusion of a pressurized fluid injected into a poroelastic medium (Hainzl et al., 2005; Parotidis et al., 2003).

The further evolutions of the two swarms are also similar and can be explained by the fluid migration concept. After the initial sudden upward movement, the hypocenters ascend further with another sudden large number of events occurring at bright spot C (blue dots in Figure A.34b, A.34f) followed by an immediate downward movement in the case of year-2000 swarm (dark blue dots in Figure A.34b). This may indicate the existence of a relatively strong barrier that obstructs the ascent of the fluids. In the later periods of both swarms (since the second half of November 2000 and 2008, respectively), the upward hypocenter migration is stopped beneath bright spot B and it then spreads in a cluster aligned with the local inclination of the bright spot (black dots in Figure A.34c, A.34g). This may be interpreted as the ascending highly-pressurized fluids being blocked by a non-permeable boundary above and having no alternative but to turn and follow the boundary, further generating earthquakes until losing all of its energy. After the termination of both swarms, the seismicity appears randomly throughout the swarm volume (black dots in Figure A.34d, A.34h). Such additional earthquakes should naturally be generated as the system returns slowly to equilibrium.

Although the hypocenters of the year 2011 swarm does not follow the exact migration pattern as that of year 2000 and 2008 swarms, their spatio-temporal evolution does show the same general trend. The swarm activity starts at the left edge of the bright spot D with an explosion

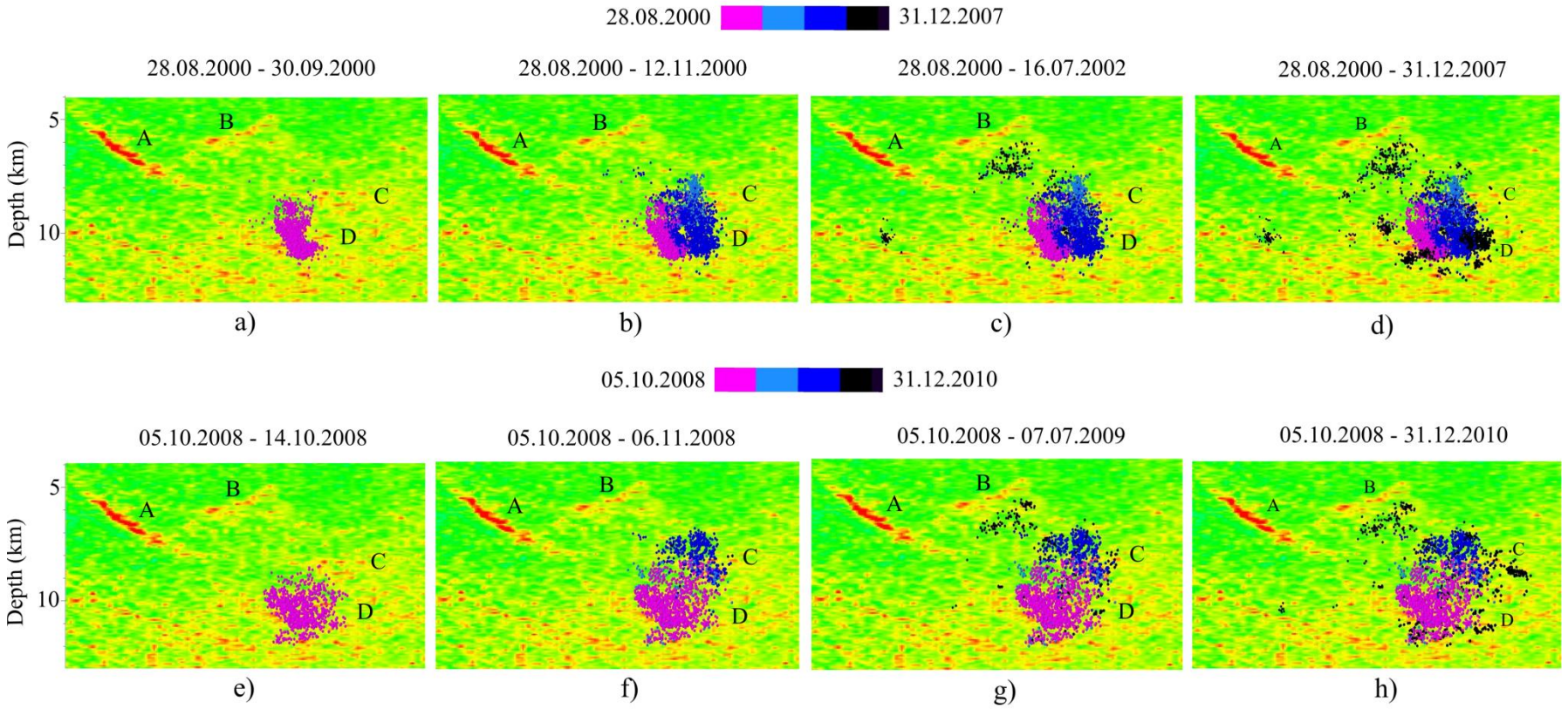

Figure A.34. Spatiotemporal evolution of the swarms 2000 (top) and 2008 (bottom) with respective subsequent seismicity plotted on top of the reflectivity image (events plotted in a cumulative manner).

like distribution of the events (Figure A.35a). This is accompanied by a few events along the whole length of the bright spot D. Then the hypocenters migrate upward and are restricted below the bright spot B (Figure A.35b). There is also random distribution of seismicity throughout the swarm volume during the whole duration of the swarm.

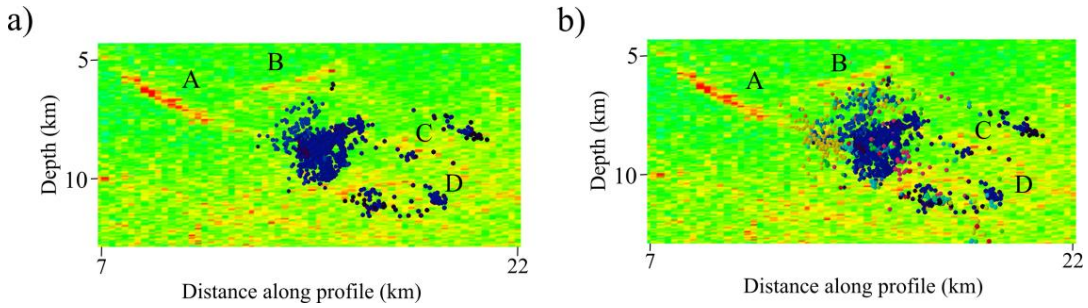

Figure A.35. Spatiotemporal evolution of the swarm of year 2011 plotted against the reflectivity image (events plotted in a cumulative manner).

The main cluster of the regional seismicity (including the swarms of years 2000; 2008 and 2011) is restricted primarily along a sub-vertical plane (Horalek et al., 2008). Therefore, the intrusion of the fluids from the over-pressured fluid zone could possibly have taken place along a relatively permeable planar zone such as a fault or a brittle patch that extends from the fragmented permeable middle crust into the less-permeable units above it (Figure (Figure A.33b). Bright spot (A) and the adjacent reflector (B) define the upper boundary of the seismicity and may then be identified as the upper edge of this semi-permeable zone. Existence of such a zone is also supported by the observation that the ascending swarm activity in both years 2000 and 2008 could not penetrate above the bright spots and instead spreads along them (Figure A.34c, A.34g, A.35b) suggesting a blockage of the earthquake-producing ascending fluids by a non-permeable boundary overhead. Particularly, the highly reflective and laterally-limited bright spot A can be well explained by entrapment of highly pressurized fluid.

Based on the above arguments the following driving mechanism for the frequent swarm

earthquakes at the western Eger rift area may be hypothesized (Figure A.33b). Fluids from a reservoir in the upper mantle rise through fragmented lower crust and are blocked by less-permeable units in the upper crust developing an over-pressured fluid zone. After a critical pressure state is reached, fluid from this zone forces its way into a semi-permeable fault zone above. This alters the stress distribution in the zone and produces swarms of micro-earthquakes. After relieving the critical energy this way, the system then returns to equilibrium until the critical pressure state is reached again due to the continuous ascent of fluid from the reservoir below. A similar concept of swarm-generating fluid migration has been proposed recently by Shelly et al. (2013) at the Yellowstone caldera.

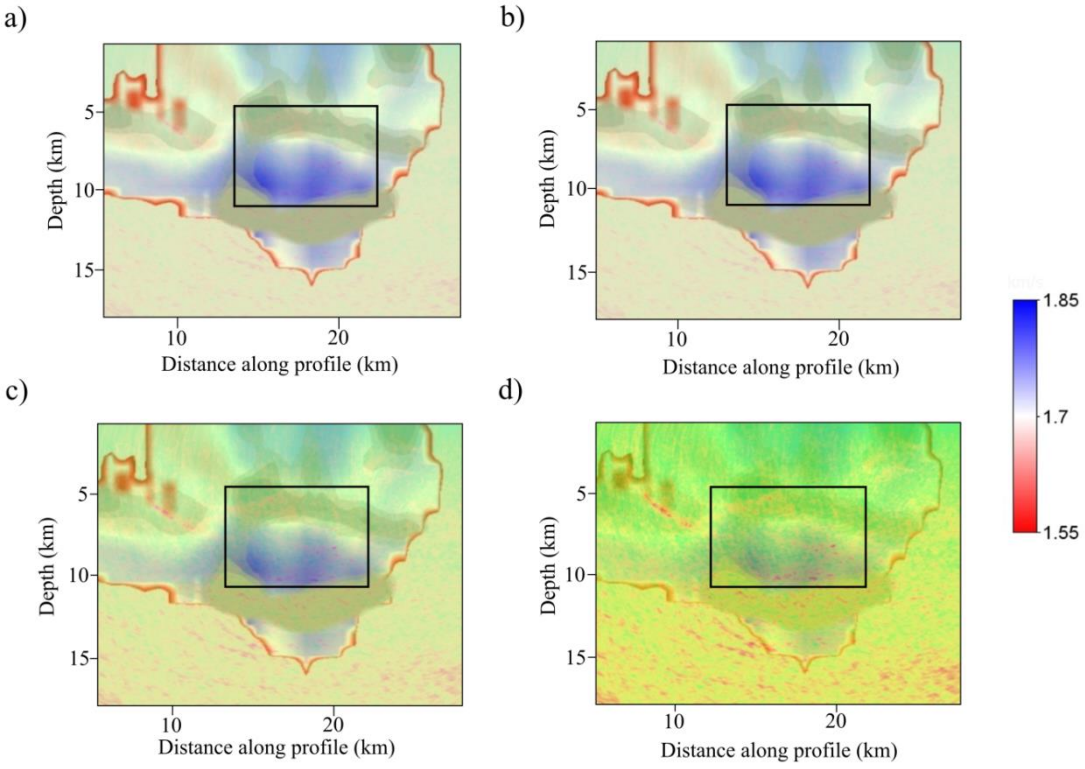

Figure A.36. $\frac{V_p}{V_s}$ ratio distribution below the swarm area (Alexandrakias et. al., 2015) at different transparencies on top of the reflectivity image.

The results of the stress analysis using year 2008 swarm events (Vavryčuk et al., 2013) which show that the seismicity distribution of year 2008 swarm can be placed along two principle

planes on which the events can be assigned (Section A.2.2.2), agrees well with the hypothesis of fluid intrusion though a fault zone causing the earthquakes. Additionally, the $\frac{V_p}{V_s}$ ratio obtained with double difference tomography employing the swarm earthquake records at the WEBNET stations (Alexandrakias et. al., 2014) reveals that the region between the bright spots C and D has a high $\frac{V_p}{V_s}$ ratio of ~1.8 (Figure A.36). This high $\frac{V_p}{V_s}$ zone has been interpreted as over pressured fluid-filled fractured rocks and is consistent with the existence of a semi-permeable zone that contains high pressure migrating fluids.

A.4.2 Subsurface reflectivity vs fluid observations

The diffusely reflective crust from a depth of 5 km directly below the Mariánské Lázně and Konstantinovy Lázně gas centers (upper edge marked by Q) hosts characteristic strong reflector segments dipping at -40^0 to -45^0 from horizontal (Figure A.37a). The overall reflectivity pattern is similar to that observed at the earthquake area (below 10 km depth) and the diffuse reflectivity can be again interpreted as fragmented permeable crust through which fluid can migrate and the reflector segments as local interruptions of the ascending fluid at small-scale discontinuities. Considering the alignment of the reflectors, they may represent parts of tunnel-like structures that can act as fluid conduits and allow for the direct transport of fluids as was indicated by the fluid studies (Weinlich et al., 1999). The region continues down to Moho with the reflector segments now oriented sub-horizontally, and has a connection to the updomed part of Moho. Fluids from a reservoir in the upper mantle can rise along such fragmented crust and accumulate and possibly produce an over-pressured zone similarly as at the earthquake area, at a depth of 5 km below the gas escape centers (Figure A.37b).

Immediately below Konstantinovy Lázně degassing center, which has several degassing

points directly on the 9HR profile (Figure A.11), some indications of sub-vertical fault-like structures can be identified (e.g. bright spot P in Figure 32c, 37a), which appeear to merge at greater depths into the underlaying region of diffuse reflectivity (upper edge marked by Q). Such features may represent local near-surface channels that can transport accumulated fluid from an over-pressured fluid zone below to the surface (Figure 37b). Unfortunately, due to the large-scale nature of the 9HR survey, the resolution in the shallow subsurface is limited and only some hint of these fluid transport features can be seen here. Directly below the Mariánské Lázně degassing center, any near-surface features similar to the bright spot P are absent. However, considering its widely distributed fluid emission points over a large area, this can be only due to the corresponding near-surface transport channels do not reflect seismic energy detectable by the 9HR source-receiver geometry.

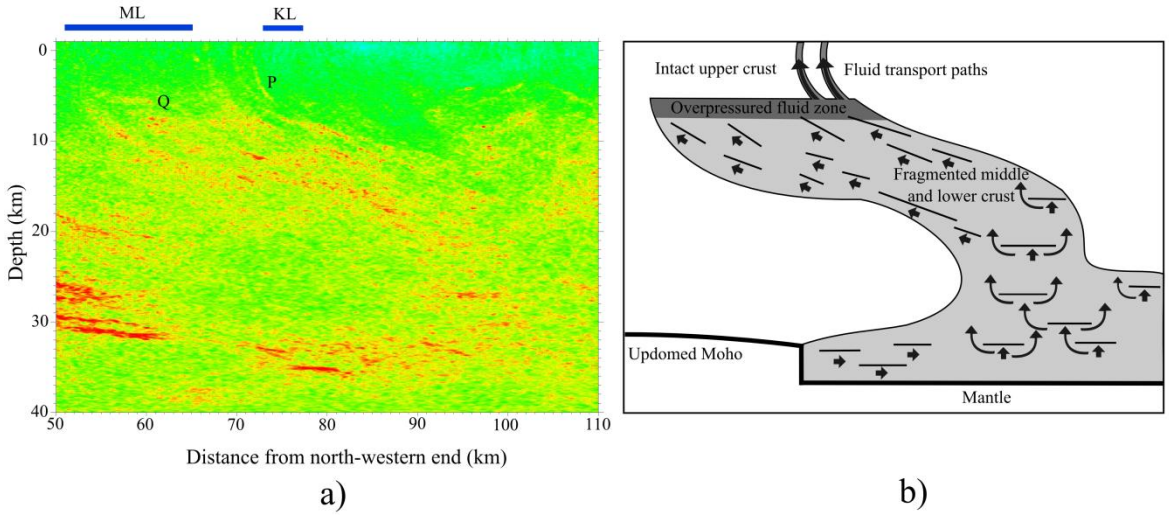

Figure A.37. a) Reflectivity image below Mariánské Lázně (ML) and Konstantinovy Lázně (KL) gas escape centers. b) Schematic sketch with the main interpreted features.

A.5 Converted wave imaging of swarm earthquake waveforms

A.5.1 Introduction

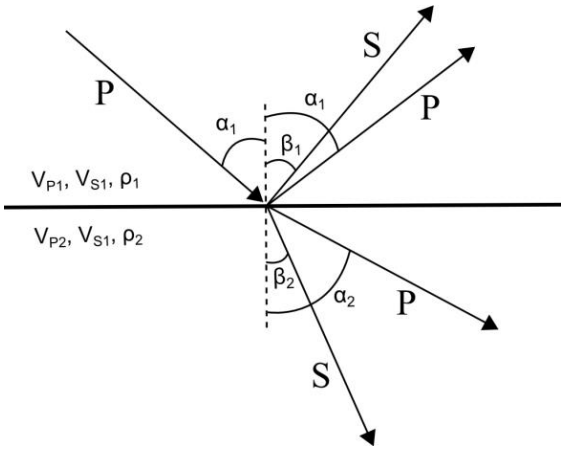

Figure A.38. Incidence of a P wave on an interface between two media with different acoustic impedances and generation of P-to-S reflected and transmitted converted waves.

For non-normal incidence of seismic wave on an interface between two media with different acoustic impedances, mode converted reflection and transmission events occur along with the normal reflection and transmission events e.g. a P wave reflected and transmitted as S wave (Figure A.38). In addition to the commonly used P-to-P reflection events, the P-to-S or S-to-P reflected and transmitted conversion events can also be migrated to produce an image of the subsurface. Due to their different wave propagation properties from the P-P reflection event, these events can provide additional imaging advantages. E.g. a vertical interface between the

source and receiver is invisible to P-P reflection events but accessible to P-to-S or S-to-P transmitted conversion events (Shelly & Schuster, 2003).

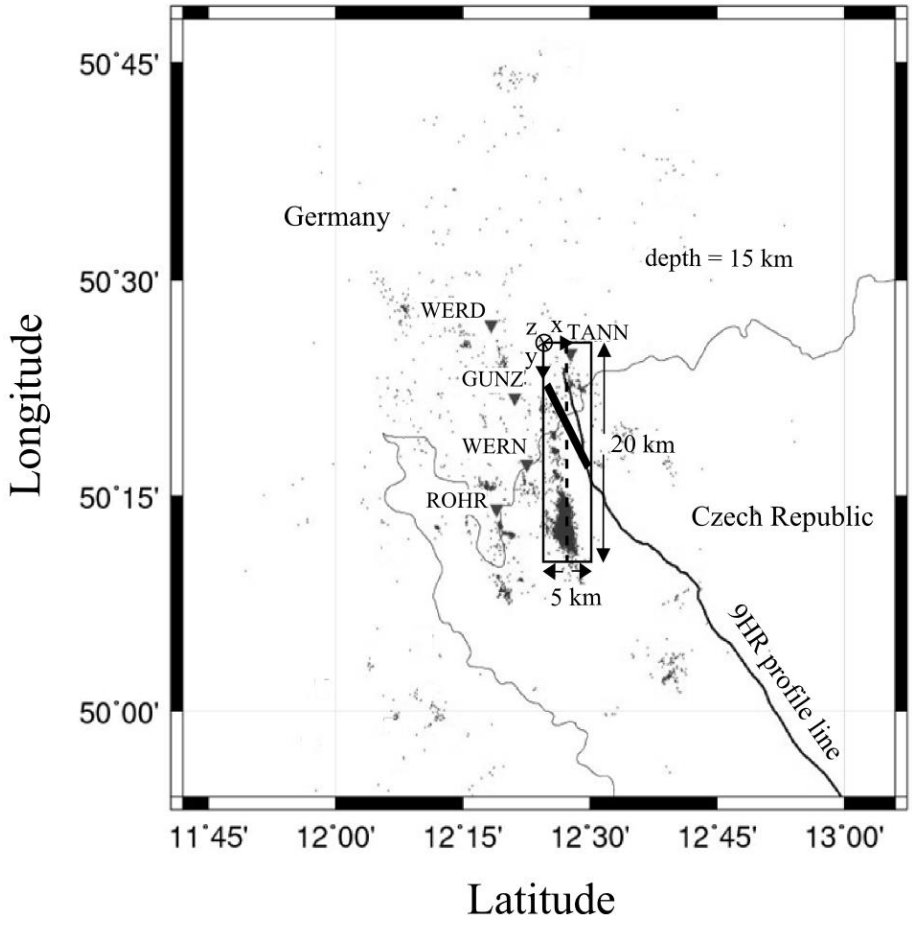

Figure A.39. Stations of GRSN Network (inverted triangles) close to the swarm area, the regional seismicity in the year 2008 (dots), the 9HR profile line and the grid used to perform migration of the P-to-S transmitted waves recorded at the station TANN. The thick line within the grid represents approximate location of the bright spots A and B in the reflectivity image of 9HR profile from Figure A.32b. The dashed line represents the location of the vertical slice of the migration grid taken as the P-to-S conversion image at the station TANN.

The bright spots A and B in the reflectivity image of the 9HR profile lies just above the swarm seismicity cluster (Figure A.33a) and is interpreted as upper boundary of a semi-permeable zone or a fluid trap. These prominent reflectors apparently represent an interface with strong impedance contrast. As the P and S waves produced by the micro-seismic

earthquakes transmit through the interface, they are expected to generate mode converted transmitted waves. These converted waves should be recorded at a seismological station located north of the swarm area (Figure A.39).

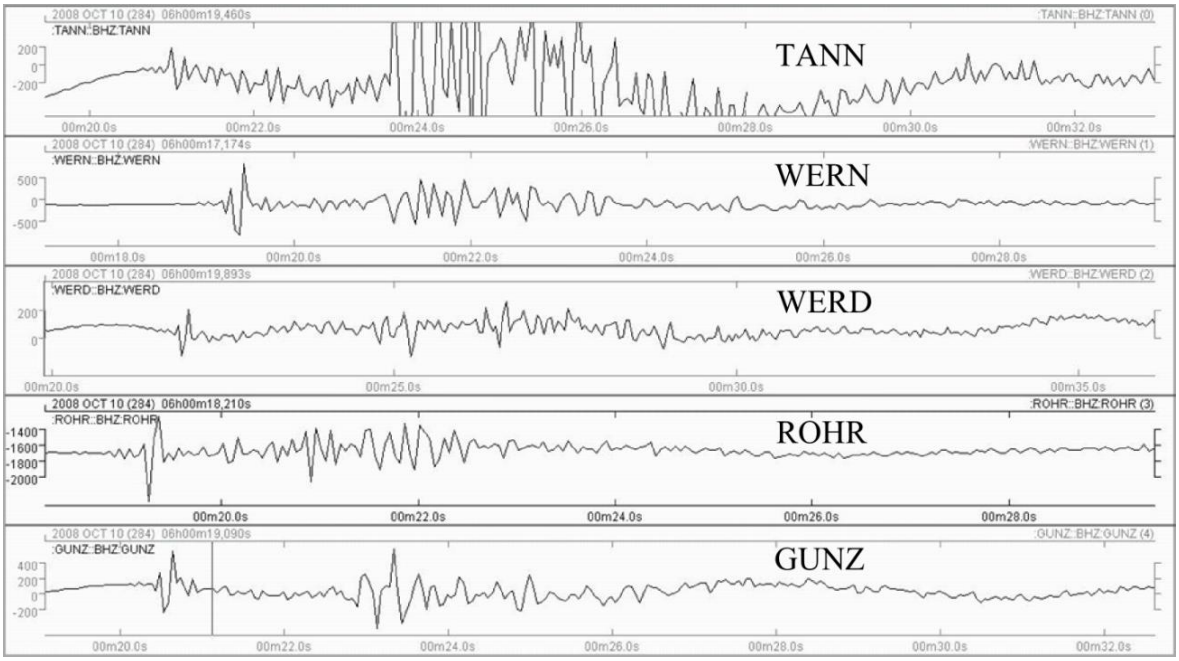

Figure A.40. Record of an event from year 2008 swarm at different stations of the GRSN Network close to the swarm area.

A number of earthquake monitoring stations are located west to north of the swarm area at the Czech-German border (Figure A.39) belonging to the German Regional Seismic Network (GRSN). These stations regularly monitor the swarm earthquakes from the Novy Kostal focal zone and the data is available publicly. The record of the events at some of these stations do show phases in the window between direct P and S that may represent the converted waves from the subsurface structure represented by bright spots A and B of Figure A.33b (Figure A.40).

Considering the location of the swarm seismicity cluster relative to the location of the bright spots A and B in the reflectivity image, the station ‘TANN’ located at the north-western end of the 9HR profile have the greatest possibility to receive the above mentioned converted

waves (Figure 39). An imaging experiment is performed here to attempt to image the converting boundary with the P-to-S converted waves generated by it using the swarm earthquakes as the sources and the station TANN as receiver. This will confirm the existence of the boundary seen in the reflectivity image from another independent seismic dataset. Additionally, new structural information may be obtained as well.

A.5.2 Methodology

Although seismic migration was originally developed for active seismic surveys, it can be also employed to passive seismic data from natural sources such as earthquakes or ambient noise (Shelly & Schuster, 2003). While in active seismic, the source can be positioned, repeated and its source impulse specified as desired, passive seismic has no such control and thus it may involve more complex processing. However, passive seismic can be advantageous for reasons such as larger bandwidth, absence of near surface distortions, ability to utilize transmitted conversions (e.g. receiver functions) etc.

The same concept of smearing of recorded wave-field along isochrons as in the Kirchhoff pre-stack depth migration can be adopted to migrate the P-to-S converted events as well (Shelly & Schuster, 2003). In case of constant velocity, the P-P reflection isochrons are in the shape of concentric ellipsoids which always enclose both the source and receiver (Figure A.41a). In contrast, the P-S conversion isochrons are oblate ellipsoids always enclosing the receiver but not necessarily the source (Figure A.41b). The points of one such oblate ellipsoid represent possible subsurface points from which a P wave originating from the source can convert to S either by transmission or reflection and reach the receiver at a specific time. The near tip part of the P-S isochrons that enclose the receiver only (indicated by dashed line in Figure A.41b) correspond the P-S transmitted conversions.

To migrate P-to-S converted events, the amplitude of the recorded wave field at a source and

receiver pair is smeared along the P-S conversion isochrons of that pair at respective recording times. When this is done with records at a number of source and receiver pairs, at actual converters the back-projected P-to-S converted waveforms interfere constructively and destructively elsewhere. Conversion energy is thus accumulated along the converters producing an image of them.

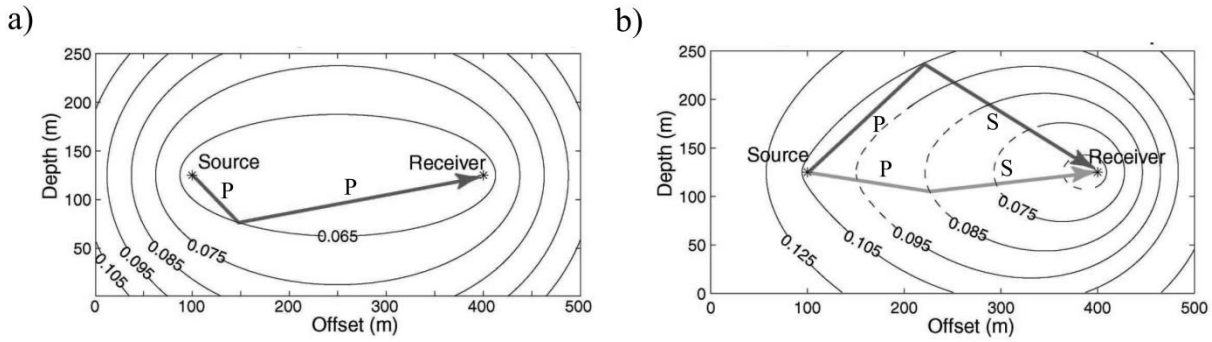

Figure A.41. a) P-to-P reflection and b) P-to-S conversion isochrons for a source and receiver pair. (Shelly & Schuster, 2003)

A.5.3 Data pre-processing

An earthquake generates both compressional wave P and shear wave S in general. At a recording station on the surface, the faster P wave arrives first followed by the slower S wave. In between these two direct waves both P to S and S to P converted waves at various interfaces between the earthquake hypocenter and the station arrives (since their travel time is between the direct P and direct S waves). The three component record of an earthquake ZNE (Z=Vertical, N=North, E=East) can be transformed to the ray coordinate system LQT (L=Direction of direct P, Q=Perpendicular to L component in the same plane as Z & L components, T=Perpendicular to both L and Q components) to separate out P and S type waves from an earthquake (Vinnik, 1977; Langston, 1979). The P and SP waves appear mainly on the L component and the S and PS waves mainly on the Q component. Instead of this rigorous coordinate rotation process, we simply use the record at the horizontal north

component of the station TANN for the imaging experiment. Considering the position of the sources located in the Novy Kostel focal zone and the bright spots A and B of the reflectivity image, this component is likely to record the P-to-S converted waves in larger amplitude than the S-to-P converted waves.

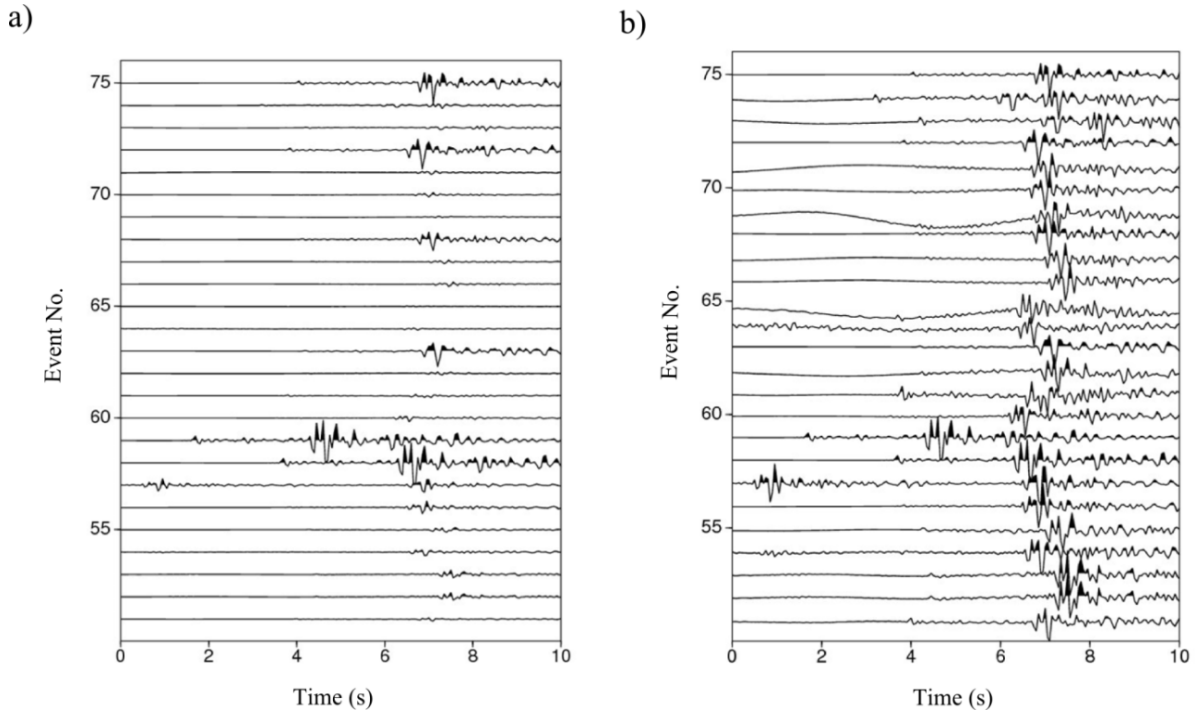

Figure A.42. a) Records of events from year 2008 swarm at the north component of station TANN. b) Same records after normalization.

Records of 146 events at the north component of station TANN that have magnitude greater than 1.5 are chosen for the experiment (Figure A.42a). Each of these records contains 10s following the occurrence of the corresponding event. Each event is checked so that it is well separated in time from other events to avoid any overlapping of records. The records are first normalized dividing by individual maximum amplitudes, to roughly compensate for the difference in magnitudes of the events (Figure A.42b). Then, they are band pass filtered with pass band of 1Hz – 9Hz to remove the low and high frequency noises (Figure A.43a).

Earthquakes are natural events with different source mechanisms and therefore each event has

its own unique source waveforms in general. To equalize these source signatures, the direct P waveform on L component can be deconvolved with all the L, Q and T components. However, in this experiment, simply the events which have similar waveforms of the direct P wave (from which the P-to-S converted waves originate) are picked. The event records with ambiguous direct P phases are also killed at this step (Figure A.43b). This results ultimately in records of 55 events that are suitable to be used for further processing. Finally, all signals outside the time window between direct P and S phases are muted to retain only the part of the records which contain the P-to-S converted waves.

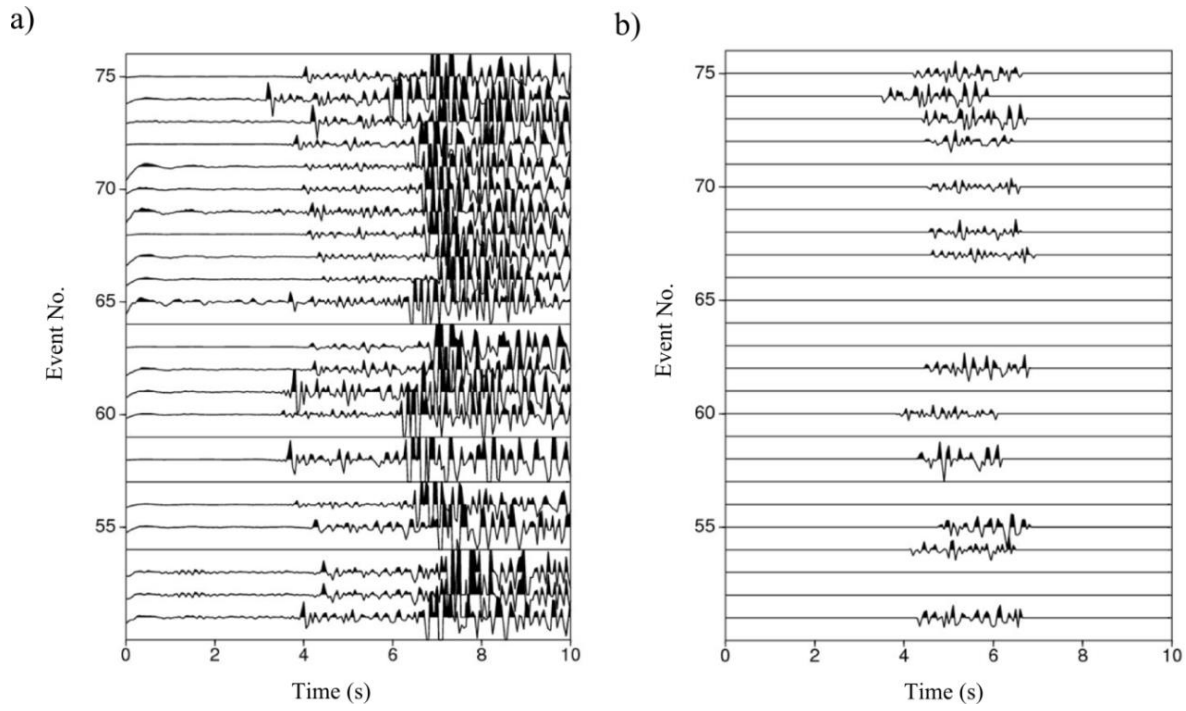

Figure A.43. a) Records of events from year 2008 swarm at the north component of station TANN after normalization and band pass filtering. b) Same records after trace killing and top and bottom muting.

A.5.4 Migration

To migrate the micro-seismic earthquake records at the north component of the station TANN, a 3D grid is defined with length (x) 20km, width (y) 5km and depth (z) 15km and a

uniform grid spacing of 100m along all axes (Figure A.39). Velocities are then assigned to the grid points according to the 1D velocity model of Malek et al. (2005) to construct a velocity grid v(x, y, z) (as in Section A.3.5). The event and station coordinates are transformed to the local grid coordinates. Then, the first arrival times to each grid point (x, y, z) from the station, t_R^S is calculated with S wave velocity and from each event, t_E^P with P wave velocity using the eikonal solver of Podvin and Lecomte (1991). The resulting travel time grid spacing is 500m along y and 100m along x, z. The P-S isochron at a time t for an event and TANN is obtained by finding all grid points of the travel time grid that have the sum of the first arrival times from the event and the station, $(t_R^S + t_E^P) = t$ (Figure A.44b).

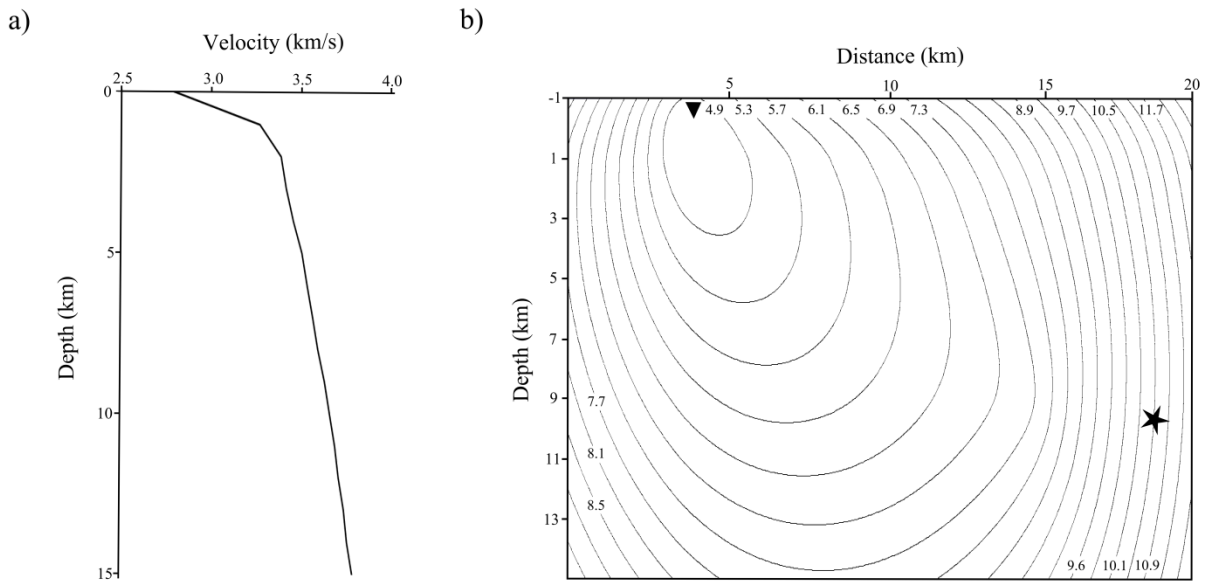

Figure A.44. a) S wave velocity model at the western Eger rift from Malek et al. (2005). b) P-to-S conversion isochrons for station TANN (inverted triangle) and an event (star) from year 2008 swarm.

The migration grid has spacing of 100m along x, 500m along y and 5m along z. To migrate the record of an event E, the recorded amplitude in the window between direct P and S (Figure A.43b) at time t is smeared along the P-S isochron for E and TANN at time t. Since, the focus in this experiment is on P-S transmission events, the smearing is limited roughly to

the tip of the oblate P-S isochron ellipsoids by restricting the smearing to 30^0 angle around the straight line connecting the source and receiver. The records of all the 55 events are thus migrated to produce a 3D migrated section. A vertical slice of this grid midway between the station and the event cluster at x = 2.5km (Figure A.39) is taken as the P-to-S transmitted conversion image for the station TANN.

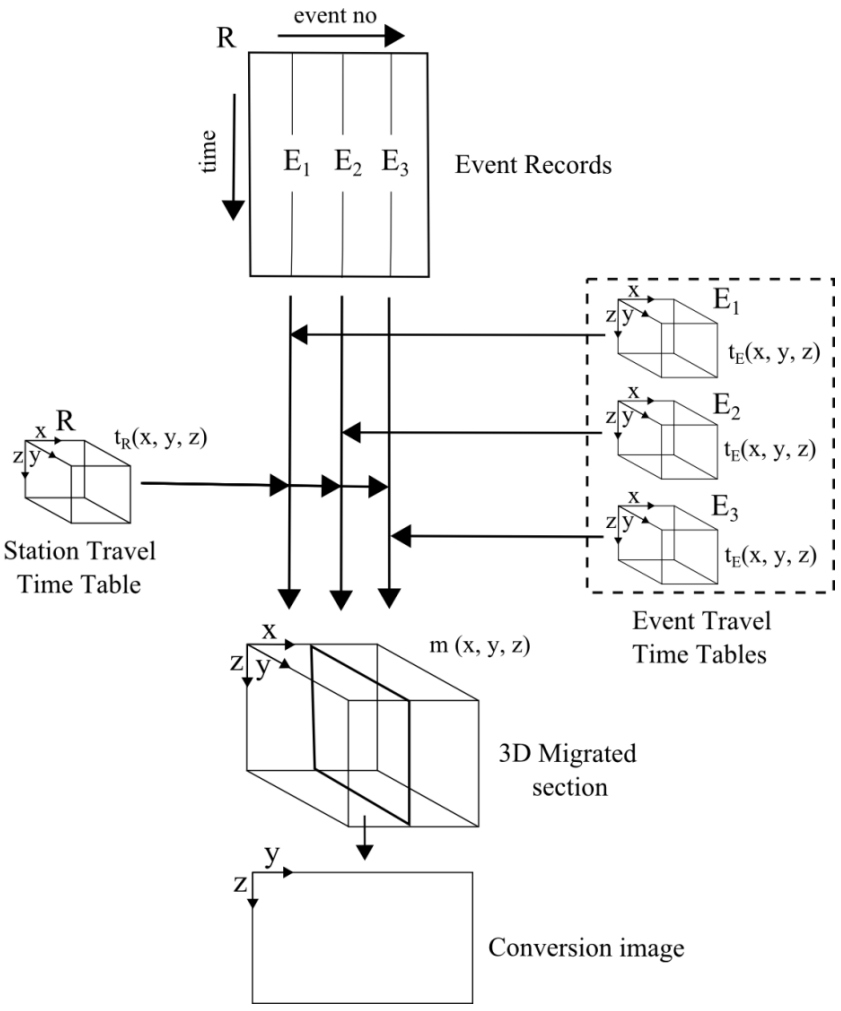

Figure A.45. Work flow for Kirchhoff pre-stack depth migration of P-to-S converted waves for three events E_1, E_2, E_3 recorded at a single station R.

A.5.5 Results

Analogous to the reflectivity image, in the P-to-S conversion image, the red-yellow colors represent points of high conversion. In the P-S conversion image at the station TANN using

the records of the Novy Kostel focal zone micro-seismic earthquakes, two prominent conversion bright spots L and M can be clearly identified (Figure A.46a). However, it is to be noted that the geometry of the events and the station is inadequate here to generate the actual geometry of the converters.

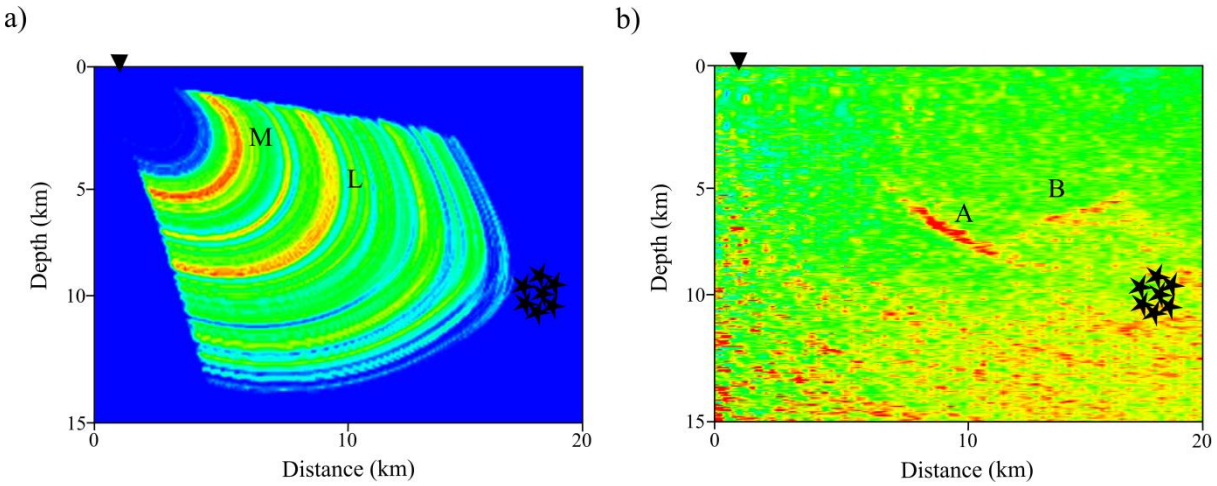

Figure A.46. a) P-to-S transmitted conversion image at the station TANN using records of events from year 2008 swarm. b) Reflectivity image of the same part of the crust from the 9HR profile. The stars and inverted triangle represent the events and the station respectively.

Comparison of the PS conversion image with the reflectivity image (Figure A.46b) suggests that the deeper converter L may represent the same interface as the reflectors A and B. No reflector is visible in the reflectivity image that may correspond to the shallower converter M. This could be due to 1) the rough direct wave muting applied in the pre-processing of the 9HR data or 2) the 3D structure of the interface does not reflect energy detectable by the 9HR source and receiver layout.

In this imaging experiment, the source events are clustered within a small region and the number of receiver is only one. Thus, as mentioned previously, this source-receiver geometry is unsuitable for the whole isochron smearing approach of the KPSDM. Although the existence of the two converting boundaries L and M can be definitely confirmed, the exact shape and location of the converters could not be obtained. This is the primary motivation for

the development of the Fresnel zone imaging technique (FZI) which is presented in the second part of this thesis. The FZI method restricts the sample smearing process of KPSDM to the potential Fresnel zones on all possible converters at which the recorded P-S conversion events can occur and is more appropriate for the lower source-receiver coverage available here. Using FZI on the same dataset, both the location and the shape of the converters may be obtained. Moreover, the new imaging technique can be applied to the swarm earthquake records at all other GRSN stations and local dedicated seismological network stations that monitors the swarm activities in the Novy Kostel area to investigate the 3D subsurface around the swarm seismicity in greater details.

A.6 Conclusions

The seismic reflectivity image of the western Eger rift obtained by reprocessing the deep reflection seismic profile ‘9HR’ reveals a number of new and significant subsurface features apparently related to the geodynamic activity at the area. Up to the maximum depth of 60 km of the image, no direct evidence of presence of any magma body in the upper mantle or lower crust is detected. However, patterns of reflecting structures can be identified that may indicate that magmatic fluids from a common root, possibly corresponding to the upwelled Moho, ascend through regions of fragmented crust and accumulate at a depth of 10 km below the main earthquake zone and 5 km below the major degassing fields and form over-pressured fluid zones. Below the earthquake area, a semi-permeable zone may exist into which critically over-pressured fluids intrude, produce the observed micro-seismicity. The upper boundary of this zone is non-permeable and prevents the fluids to rise up to the surface. In contrast, below the degassing fields the over-pressured fluid may further rise along near-surface channels and cause the observed fluid emissions. A mantle plume(s) below the western Eger rift, as suggested by receiver functions and tomography studies, may act as the source for these magmatic fluids.

Despite the fact that the reprocessed 9HR profile sheds considerable light on the crustal structure beneath the study area, it is only a 2D line. Therefore, it does not represent the 3D situation beneath the area (e.g. the swarm area has a lateral offset of several kilometers from it). New reflection seismic studies could be useful in this regard, in particular to see how the

structures imaged by the 9HR profile extend laterally and how they agree with the conclusions drawn here.

The P-to-S transmitted conversion image using swarm earthquake records at station TANN shows two prominent converters between the station and the swarm seismicity cluster. One of these converters closely correspond the reflectors in the reflectivity image from 9HR profile that represent the non-permeable fluid trapping boundary above the swarm earthquake zone. This provides further evidence on the existence of such a fluid trap. However, the exact location and shape of the converters could not be obtained due to the inappropriate source-receiver coverage and the limitations of the imaging technique used. This raises the need to develop a new seismic imaging technique that can effectively image the P-to-S conversion events using the same dataset. The new method can be then employed on swarm earthquake records at the numerous seismological stations located in the area to examine the 3D subsurface in the vicinity of the swarm seismicity.

B Fresnel zone imaging

B.1 Introduction

Imaging the Earth's interior is essential for exploration of natural resources as well as for understanding Earth's processes. A variety of seismic imaging techniques have been developed over the last decades that employ seismic waves to obtain structural information of the crust and mantle. These techniques are applied either to datasets obtained from controlled-source experiments or to seismological datasets from natural or induced earthquakes.

The compressional wave (P) or shear wave (S) excited in Earth by a seismic source is reflected by different subsurface discontinuities. Using the record of these reflection events at a number of receivers, the events can be geometrically re-located to the location where they occurred in the subsurface and thereby produce a map of the subsurface. This method of seismic imaging is known as seismic migration. Although P-to-P reflection events are used primarily (for reasons such as, it is the first arriving wave, generally have high signal-to-noise ratio, easily generated by a variety of sources, propagate in a marine environment etc; Stewart et al., 1999), the mode converted S-to-P or P-to-S reflection and transmission events are also common to be employed for this purpose. Consequently, seismic migration is applicable in numerous imaging geometries that include reflection seismic profiling, vertical seismic

profiling (VSP), cross-well seismic profiling (CSP) and earthquakes (e.g. receiver function technique).

In this part of the thesis, a new seismic migration imaging method is presented called Fresnel zone imaging (FZI). The method works by back projecting records of reflected/converted seismic waves at a number of receivers to all potential Fresnel zones on all possible reflectors/converters from which the recorded waves may originate. The back projected reflected/converted waveforms interfere constructively at the true reflectors/converters and destructively elsewhere to generate an image of the subsurface. This imaging approach is based on the same core imaging principle as the Kirchhoff pre-stack depth migration (KPSDM); a robust seismic migration technique based on the integral solution of the elastic wave equation (Schneider, 1978). However, in KPSDM, the back projection is not focused to the Fresnel zones on the reflectors/converters and a lot of back projected energy is placed away from the subsurface structures to be imaged. This results in considerable noise and artifacts.

A number of techniques have been developed already to restrict the above-mentioned back projection process of KPSDM in the vicinity of specular rays (e.g. Hill, 1990, Schleicher et al., 1993;Sun and Schuster, 2003; Hua and McMechan, 2005; Lüth et al., 2005; Buske et al., 2009) which would produce similar effect as FZI. However, while KPSDM is applicable to mode converted waves as well, these techniques are usually designed for the P-to-P reflection events only and may not be readily extended to the case of conversion events. In contrast, FZI can make use of both P-to-P/S-to-S reflected and P-to-S/S-to-P reflected or transmitted mode converted waves and at the same time it is relatively simpler to implement and computationally faster than some of the existing techniques.

In the following text, the principle of FZI is described in full details for S-to-P converted

transmitted waves followed by a brief account of how it can be applied to P-to-P reflected waves. The synthetic and real data tests presented are also limited only to these waves. The imaging principle can be extended to the case of the other wave types straightforward following these examples. The tests are all carried out with both FZI and KPSDM techniques to illustrate the difference in their working principles and to demonstrate what this difference enables the FZI technique to achieve over the KPSDM technique.

B.2 Methodology

B.2.1 Origin of an S-to-P converted transmitted wave

Let AB be an interface between a source at position E at a certain depth and a surface receiver at position R (Figure B.1a). An S wave with a period T_c is generated at E. As this S wave propagates and meets AB, a part of it converts to P, transmits through the interface, reaches R in time t_C and gets recorded as waveform W_C. This S-to-P converted wave is superposition of the S wave diffracted as P from all points within the Fresnel zone CD on the converter AB. The earliest of these diffracted waves arrives at R from the specular conversion point F with travel time t_C along the path EFR. It is then followed by diffracted waves from the points M in the vicinity of F within CD with travel times t_M (where $t_C < t_M \leq t_C + \frac{T_C}{2}$) along the paths EMR.

All points in the subsurface at which an S wave originating from E can convert to a P wave and reach R at a certain time form an oblate ellipsoid (in the case of constant velocity) and is referred to as the SP isochron for that time (Figure B.1a). If we draw the SP isochron at time t_M, it will intersect the converter AB at multiple points. This is because, the travel times of S waves from E that diffracts at AB as P wave and reach R can be identical along multiple paths. E.g. the SP isochron at time $t_C + \frac{T_C}{2}$ intersects AB at points C and D since the travel along both ECR and EDR is $t_C + \frac{T_C}{2}$. However, the SP isochron at time t_C will intersect AB

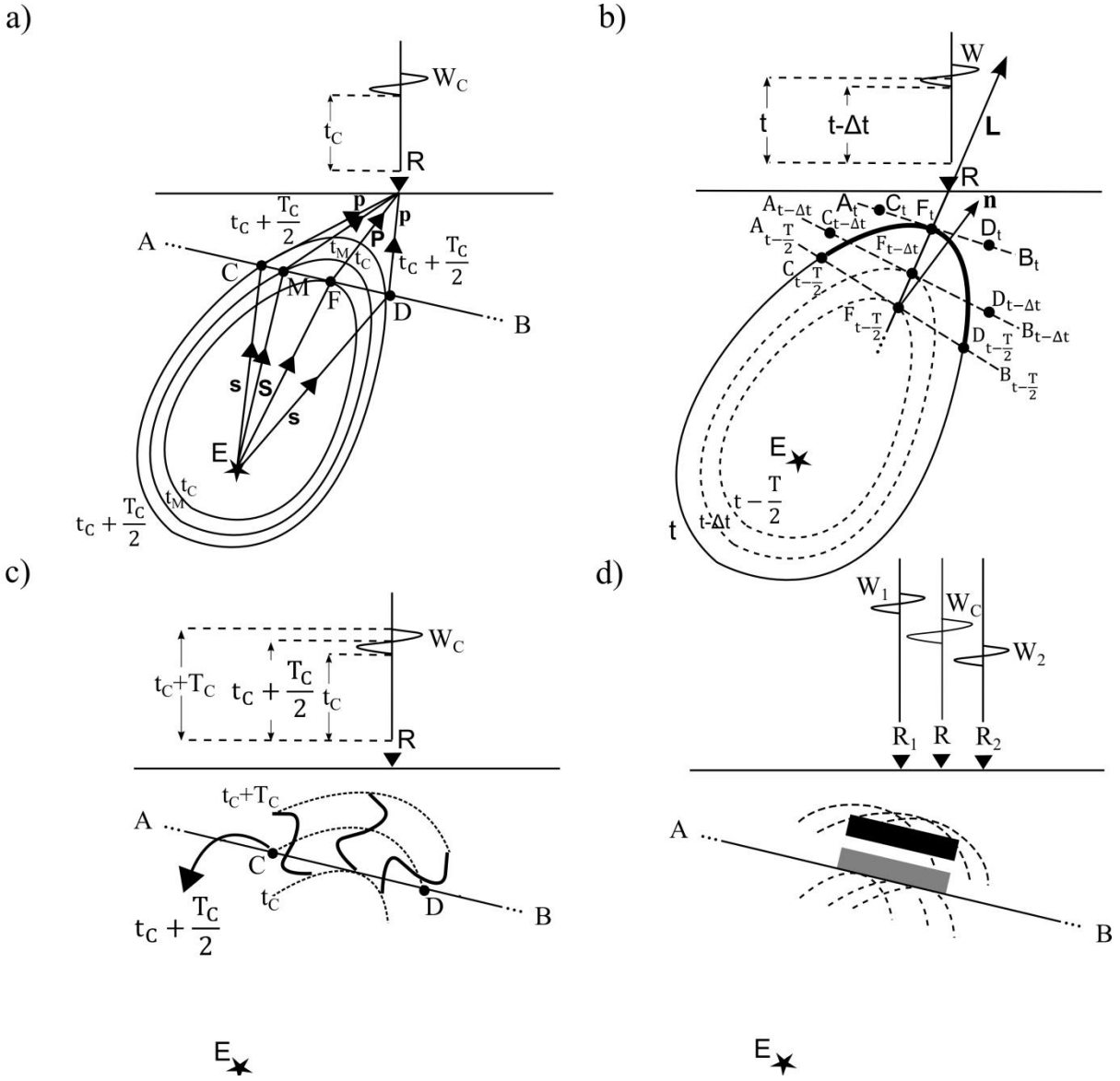

Figure B.1. Principle of Fresnel zone imaging with S-to-P converted transmitted waves, a) origin of an S-to-P converted transmitted waveform W_C recorded at time t_C at a receiver R from a source E, b) possible points of the S-to-P conversion isochron at time t from which an S-to-P diffracted wave may originate and contribute to an S-to-P converted transmitted waveform W recorded at time t-Δt at R, c) W_C projected back to the Fresnel zone part of the converter AB at which it is produced, d) converter AB generated by constructive interference of the back projected S-to-P converted transmitted waveforms recorded at stations R, R_1 and R_2. The black and grey solid rectangles represent positive and negative intensities formed by constructive interference of individual converted waveforms.

only at a single point which is the specular conversion point F. This is because the travel time of the S-to-P diffracted wave along the specular ray path EFR, t_C is the minimum among all possible paths from E to R and is unique. We note that this implies that the converter (AB) is tangent to the SP isochron which corresponds to the travel time along the specular ray path (t_C), at the specular conversion point (F). We also note that the travel time along the specular ray path (t_C) is the time of arrival of the S-to-P converted wave (W_C).

B.2.2 Principle of Fresnel zone imaging

We consider the record of the event E at the receiver R that contains the S-to-P converted waveform W_C at time t_C (Figure B.1a). We aim to project W_C back to the Fresnel zone CD on the converter AB from which it originated.

We take an arbitrary time t on the record at R (Figure B.1b). We assume that at this time, an S-to-P diffracted wave arrives at R from E via conversion at a certain converter and takes part in forming an arbitrary S-to-P converted waveform W of period T recorded at time t-Δt at R. We further assume that the specular conversion point that corresponds W is $F_{t-\Delta t}$ and the Fresnel zone that generates W is $C_{t-\Delta t}D_{t-\Delta t}$. We attempt to locate $F_{t-\Delta t}$ and $C_{t-\Delta t}D_{t-\Delta t}$.

Let **L** be the vector that points towards the direction of incidence of the S-to-P converted wave represented by W. The specular ray path of the wave can be traced by tracing back a ray in the direction reverse of **L**. The specular conversion point $F_{t-\Delta t}$ must be located on this ray. Again, since the waveform W is recorded at R at the time t-Δt, the travel time along the specular ray path must be t-Δt. Therefore, $F_{t-\Delta t}$ must also be located on the isochron at time t-Δt. Thus, $F_{t-\Delta t}$ is the intersection point of the ray traced back in the direction reverse of **L** with the SP isochron at time t-Δt.

We now recall that the converter is tangent to the isochron that corresponds to the travel time

along the specular ray path, at the specular conversion point (Section B.2.1). Thus the converter that produces W is tangent to the isochron at time t-Δt at $F_{t-\Delta t}$. Assuming that the curvature of the Fresnel zone $C_{t-\Delta t}D_{t-\Delta t}$ which is located on this converter is negligible, $C_{t-\Delta t}D_{t-\Delta t}$ is part of the plane $A_{t-\Delta t}B_{t-\Delta t}$ that is tangent to the isochron at time t-Δt at $F_{t-\Delta t}$ (Figure B.1b).

For Δt = 0, the Fresnel zone $C_{t-\Delta t}D_{t-\Delta t} = C_tD_t$ is located along the tangent plane $A_{t-\Delta t}B_{t-\Delta t} = A_tB_t$ to the time t isochron at the specular conversion point $F_{t-\Delta t} = F_t$. This is the case when the diffracted wave that arrives at R at time t comes from the specular conversion point of a Fresnel zone which is located on a certain possible converter. For $\Delta t = \frac{T}{2}$, the Fresnel zone $C_{t-\Delta t}D_{t-\Delta t} = C_{t-\frac{T}{2}}D_{t-\frac{T}{2}}$ is located along the tangent plane $A_{t-\Delta t}B_{t-\Delta t} = A_{t-\frac{T}{2}}B_{t-\frac{T}{2}}$ to the time $t-\frac{T}{2}$ isochron at the specular conversion point $F_{t-\Delta t} = F_{t-\frac{T}{2}}$. This is the case when the diffracted wave that arrives at R at time t comes from the edge of a Fresnel zone which is located on another possible converter. By considering all values of Δt between 0 and $\frac{T}{2}$, all potential Fresnel zones located on all possible converters at which the diffracted wave that arrives at R at time t is produced can be thus traced. We define the subset of the time t SP isochron that lies on the potential Fresnel zones $C_{t-\Delta t}D_{t-\Delta t}$ $(0 \leq \Delta t \leq \frac{T}{2})$ as its Fresnel zone portion. This subset represents the subsurface points from which the S-to-P diffracted wave that arrives at R at time t may originate and can possibly take part in forming an S-to-P converted waveform (W) at the record at R.

To back project the S-to-P converted waveform W_C recorded at time t_C at R to the Fresnel zone CD (Figure B.1a), we take the amplitudes of the recorded wave-field at R at different recording times and smear them on the Fresnel zone portions of the SP isochrons at the respective times (Figure B.1c). At time t_C of the record, a real diffracted wave arrives at R from the specular conversion point F of the real Fresnel zone CD. In this case, out of all

possible S-to-P converted waveforms W at t_C-Δt ($0 \leq \Delta t \leq \frac{T}{2}$) to which a diffracted wave arriving at time t_C may contribute, W at $\Delta t = 0$ represent the real waveform W_C and the corresponding possible Fresnel zone $C_{tc}D_{tc}$ represent the real Fresnel zone CD. As the record at R at time t_C is smeared along the Fresnel zone portion of the time t_C isochron (Figure B.1c), it is placed at the specular conversion point F on the converter AB which corresponds W = W_C at $\Delta t = 0$ as well as at different other points on the same isochron that corresponds other possible but non-existing waveforms represented by W at $\Delta t > 0$. The first sample of the waveform W_C at time t_C is thus smeared exactly below the Fresnel zone CD along the time t_C isochron touching the converter AB only at the specular conversion point F.

Similarly, at time $t_C + \frac{T}{2}$ of the record, real diffracted waves arrive at R from the edges of the real Fresnel zone CD. In this case, out of all the possible waveforms W at time $t_C + \frac{T}{2} - \Delta t$ ($0 \leq \Delta t \leq \frac{T}{2}$) to which a diffracted wave arriving at time $t_C + \frac{T}{2}$ may contribute, W at $\Delta t = \frac{T}{2}$ represent the real waveform W_C and the corresponding possible Fresnel zone $C_{tc-T/2}D_{tc-T/2}$ represent the real Fresnel zone CD. As the record at R at time $t_C + \frac{T}{2}$ is smeared along the Fresnel zone portion of the time $t_C + \frac{T_C}{2}$ isochron, it is placed on the edges of the Fresnel zone CD on the converter AB which corresponds W = W_C at $\Delta t = \frac{T}{2}$ plus at different other points on the same isochron that corresponds other possible but non-existing waveforms represented by W at $\Delta t < \frac{T}{2}$. The sample of the waveform W_C at time $t_C + \frac{T_C}{2}$ is thus smeared exactly above the Fresnel zone CD along the time $t_C + \frac{T_C}{2}$ isochron touching the converter AB at the edges of CD (Figure B.1c).

The samples of W_C between time t_C and $t_C + \frac{T_C}{2}$ are placed similarly at different points of CD where the Fresnel zone portions of the SP isochrons at the respective times intersect AB. The

samples at times greater than $t_C + \frac{T_C}{2}$ are not placed directly on any point on the converter but the smearing is limited to the area above the Fresnel zone CD. The waveform W_C is thus projected back to the Fresnel zone CD on the converter AB (Figure B.1c).

If we execute the above procedure on a sufficient number of records at different event-station pairs which all have recorded S-to-P converted wave from AB, the back projected waveforms will interfere constructively along the converter and the back projected energy will accumulate (bright spot) to generate an image of the converter. E.g. if we back project the S-to-P converted waveforms from AB, W_C, W_1 and W_2 recorded at the receivers R, R_1 and R_2 respectively from the same event E, the back projected waveforms interfere constructively along AB and result in an image of the same (Figure B.1d).

B.2.3 Calculation of the Fresnel zone portion

Since the potential Fresnel zones $C_{t-\Delta t}D_{t-\Delta t}$ are parts of the tangent planes $A_{t-\Delta t}B_{t-\Delta t}$ (Figure B.1b), the subset of the time t isochron which lies on these tangent planes is its Fresnel zone portion. Assuming that the variation in the orientations of the tangent planes is small within the time interval Δt ($0 < \Delta t \leq \frac{T}{2}$), we may approximately take the part of the time t isochron between the specular conversion point for $\Delta t = 0$, F_t and the tangent plane for $\Delta t = \frac{T}{2}$, $A_{t-\frac{T}{2}}B_{t-\frac{T}{2}}$ as its Fresnel zone portion (Figure B.1b).

The equation of the tangent plane $A_{t-\frac{T}{2}}B_{t-\frac{T}{2}}$ can be obtained as,

$$nx \cdot x + ny \cdot y + nz \cdot z - \left(nx \cdot Fx_{t-\frac{T}{2}} + ny \cdot Fy_{t-\frac{T}{2}} + nz \cdot Fz_{t-\frac{T}{2}}\right) = 0$$

$$\text{Or,} \qquad nx \cdot \left(x - Fx_{t-\frac{T}{2}}\right) + ny \cdot \left(y - Fy_{t-\frac{T}{2}}\right) + nz \cdot \left(z - Fz_{t-\frac{T}{2}}\right) = 0$$

where ($Fx_{t-\frac{T}{2}}$, $Fy_{t-\frac{T}{2}}$, $Fz_{t-\frac{T}{2}}$) are coordinates of the specular conversion point for $\Delta t = \frac{T}{2}$, $F_{t-\frac{T}{2}}$ and (nx, ny, nz) are components of the normal vector **n** to the isochron at time $t-\frac{T}{2}$ at $F_{t-\frac{T}{2}}$.

The points of the time t isochron that are on the same side of the tangent plane $A_{t-\frac{T}{2}}B_{t-\frac{T}{2}}$ as F_t, lies on its Fresnel zone portion (Figure B.1b). Therefore, a point (x_i, y_i, z_i) of the time t isochron is within its Fresnel zone portion if,

$$\frac{nx\cdot\left(x_i-Fx_{t-\frac{T}{2}}\right)+ny\cdot\left(y_i-Fy_{t-\frac{T}{2}}\right)+nz\cdot\left(z_i-Fz_{t-\frac{T}{2}}\right)}{nx\cdot\left(Fx_t-Fx_{t-\frac{T}{2}}\right)+ny\cdot\left(Fy_t-Fy_{t-\frac{T}{2}}\right)+nz\cdot\left(Fz_t-Fz_{t-\frac{T}{2}}\right)}>0 \qquad \ldots.(B.1)$$

Where (Fx_t, Fy_t, Fz_t) are coordinates of F_t.

Following the above approach, the steps to find Fresnel zone portion of an isochron at time t for a source and receiver pair E and R can be summarized as (Figure B.1b),

1) Determine the direction of incidence of the S-to-P converted wave at R, the vector **L** at time t.
2) Trace back ray in the direction reverse of **L** till it intersects the isochron at time t and note coordinates of the intersection point F_t, (Fx_t, Fy_t, Fz_t). Continue till the ray intersects the isochron at time $t-\frac{T}{2}$ and note the coordinates of the intersection point $F_{t-\frac{T}{2}}$, ($Fx_{t-\frac{T}{2}}$, $Fy_{t-\frac{T}{2}}$, $Fz_{t-\frac{T}{2}}$).
3) Calculate the components of the normal vector to the isochron at time $t-\frac{T}{2}$ at the point $F_{t-\frac{T}{2}}$, **n**,

$$nx=\frac{\partial t_{ER}}{\partial x}, \qquad ny=\frac{\partial t_{ER}}{\partial y}, \qquad nz=\frac{\partial t_{ER}}{\partial z}$$

where $t_{ER}(x, y, z)$ is the travel time from E to a subsurface point (x, y, z) with S wave velocity plus the travel time from (x, y, z) to R with P wave velocity.

4) Find the points (x_i, y_i, z_i) of the isochron at time t that satisfies equation B.1.

B.2.4 Fresnel zone imaging with reflected waves

We consider a subsurface reflector A_RB_R below a surface source at position E and a surface receiver at position R (Figure B.2a). A P wave with period T_c generated at E is reflected from A_RB_R and recorded at R as the waveform W_R at time t_R. We adapt the same imaging approach as described above for the S-to-P converted transmitted wave to back project the P-to-P reflected waveform W_R to the Fresnel zone C_RD_R on the reflector A_RB_R where it originated.

We take an arbitrary time t on the record of ground motion at R and assume that a P-to-P diffracted wave arrives at this time from A_RB_R to take part in forming an arbitrary P-to-P reflected waveform W at time t-Δt ($0 < \Delta t \leq \frac{T}{2}$). The isochrons for P-to-P reflected waves for constant velocity are ellipsoid surfaces with the source E and receiver R at its foci (Figure B.2a). We determine the vector **L** which points in the direction of incidence of P-to-P reflected wave represented by W at R and trace back a ray in the direction reverse of it (Figure B.2b). Following similar arguments as in case of the S-to-P converted transmitted wave, the potential Fresnel zones $C_{t-\Delta t}D_{t-\Delta t}$ from which the P-to-P diffracted wave that arrives at R at time t may originate are part of the tangent planes $A_{t-\Delta t}B_{t-\Delta t}$ to the PP reflection isochrons at times t-Δt, at the intersection points of the isochrons with the back traced ray.

The Fresnel zone portion of the time t PP reflection isochron is taken as the subset of the isochron that lies on the tangent planes $A_{t-\Delta t}B_{t-\Delta t}$. We approximate it again by the part of the time t PP isochron between the specular reflection point for $\Delta t = 0$, F_t and the tangent plane for $\Delta t = \frac{T}{2}$, $A_{t-\frac{T}{2}}B_{t-\frac{T}{2}}$. The amplitudes of the recorded wave-field at R at different recording times are smeared along the Fresnel zone portions of the PP isochrons at the respective times to back project W_R to the Fresnel zone C_RD_R on the reflector A_RB_R (Figure B.2c). When this sample smearing process is repeated for records at a number of receivers R, R_1 and R_2 (Figure

B.2d) all of which record P-to-P reflected waves from the reflector A_RB_R, the back projected waveforms W_R, W_1 and W_2 interfere constructively along A_RB_R and result in an image of the same.

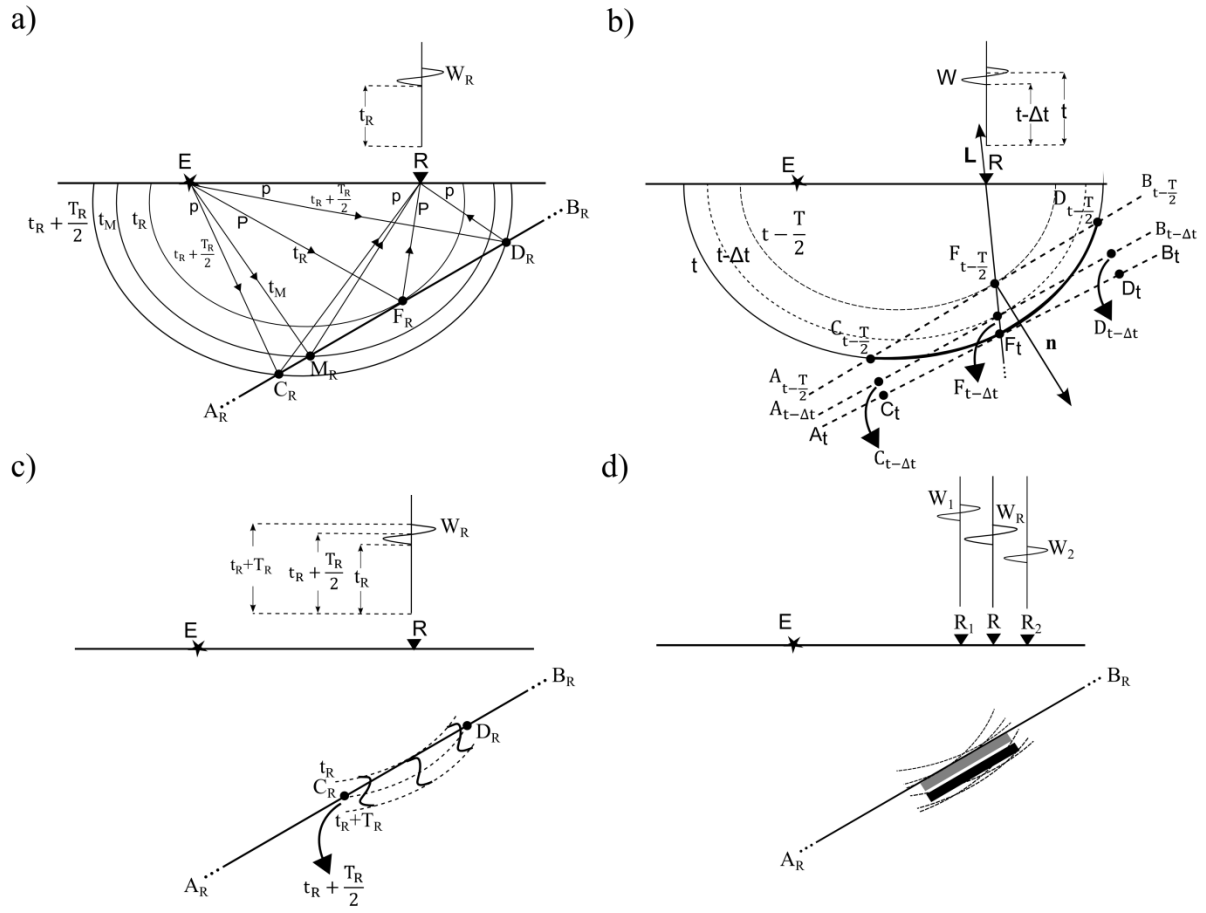

Figure B.2. Principle of Fresnel zone imaging with P-to-P reflected waves, a) origin of a P-to-P reflected waveform W_R recorded at time t_R at a receiver R from a source E, b) possible points of the P-to-P reflection isochron at time t from which a P-to-P diffracted wave may originate and contribute to a P-to-P reflection waveform W recorded at time t-Δt at R, c) W_R projected back to the Fresnel zone part of the reflector A_RB_R at which it is produced, d) reflector A_RB_R generated by constructive interference of the back projected P-to-P reflected waveforms recorded at stations R, R_1 and R_2. The black and grey solid rectangles represent positive and negative intensities formed by constructive interference of individual reflected waveforms.

The steps to find Fresnel zone portion of an isochron at time t for a source E and receiver R in case of the P-to-P reflected wave can be summarized as (Figure B.2b),

1) Determine the direction of incidence of the P-to-P reflected wave, the vector **L** at R at time t.
2) Trace back ray in the reverse direction of **L** till it intersects the isochron at time $t - \frac{T}{2}$ and note the coordinates of the intersection point $F_{t-\frac{T}{2}}$, ($Fx_{t-\frac{T}{2}}$, $Fy_{t-\frac{T}{2}}$, $Fz_{t-\frac{T}{2}}$). Continue till the ray intersects the isochron at time t and note the coordinates of the intersection point F_t, (Fx_t, Fy_t, Fz_t).
3) Calculate the components of the normal vector to the isochron at time $t - \frac{T}{2}$ at the point $F_{t-\frac{T}{2}}$, **n**,

$$nx = \frac{\partial t_{ER}}{\partial x}, \qquad ny = \frac{\partial t_{ER}}{\partial y}, \qquad nz = \frac{\partial t_{ER}}{\partial z}$$

where $t_{ER}(x, y, z)$ is the travel time from E to a subsurface point (x, y, z) plus the travel time from the point (x, y, z) to R with P wave velocity.

4) Find the points (x_i, y_i, z_i) on the isochron at time t that satisfies the condition,

$$\frac{nx \cdot \left(x_i - Fx_{t-\frac{T}{2}}\right) + ny \cdot \left(y_i - Fy_{t-\frac{T}{2}}\right) + nz \cdot \left(z_i - Fz_{t-\frac{T}{2}}\right)}{nx \cdot \left(Fx_t - Fx_{t-\frac{T}{2}}\right) + ny \cdot \left(Fy_t - Fy_{t-\frac{T}{2}}\right) + nz \cdot \left(Fz_t - Fz_{t-\frac{T}{2}}\right)} > 0 \quad \ldots . (B.2)$$

B.2.5 Estimation of the direction of incidence

The direction of incidence of the recorded wave field at the receivers needs to be calculated to find the Fresnel zone portion of the isochrons. For a three component receiver, this can be determined by the polarization analysis of the recorded signal (Maercklin, 2001). As a mono-frequent wave arrives at a receiver, it oscillates along an ellipsoid called a polarization ellipsoid. The direction of the principal axis of this ellipsoid is the propagation direction of the

incident P wave and perpendicular to it is the direction of the incident S wave. However, seismic wave usually contain a band of frequency and the receiver point thus follow a complex trajectory called a hodograph. The hodograph can be least square fit to an ellipsoid by covariance analysis of the recorded wave-field components X, Y, Z. This involves solving the eigenvalue equation over a certain time window of N samples,

$$\mathbf{M}\,\mathbf{V}_i = \lambda_i\,\mathbf{V}_i$$

Where $M = \begin{pmatrix} \mathrm{Cov}(X,X) & \mathrm{Cov}(X,Y) & \mathrm{Cov}(X,Z) \\ \mathrm{Cov}(X,Y) & \mathrm{Cov}(Y,Y) & \mathrm{Cov}(X,Y) \\ \mathrm{Cov}(X,Y) & \mathrm{Cov}(X,Y) & \mathrm{Cov}(Z,Z) \end{pmatrix}$ is called the covariance matrix with $\mathrm{Cov}(X, Y) = \frac{1}{N} \sum_{k=-(N-1)/2}^{(N-1)/2} [X_k(t) - \mu_x][Y_k(t) - \mu_y]$ and μ_x is the mean sample value within the time window of N samples of component X. The eigenvector $\mathbf{V_1}$ associated with the largest eigenvalue λ_1 points in the direction of the principal axis of the fitted ellipsoid and can be approximately taken as the incidence direction of a P wave at the receiver.

For single component recording with closely spaced receivers, the direction of incidence of the recorded wave field can still be determined by local slowness analysis. In the examples given in this thesis, this is done following the method of Kimball and Marzetta (1984) which is based on the concept of semblance, a normalized measure of coherency in seismic data (Taner and Koehler, 1969). For receivers placed along a straight survey line at an interval of Δx, at any time t on the record at a receiver R, semblance S is calculated for a pre-defined time window T using records at N neighboring receivers as,

$$S(p_x, t) = \frac{1}{N} \frac{\int_{t=0}^{T} \left[\sum_{i=0}^{N} w_i(t \pm p_x i\Delta x)\right]^2 dt}{\int_{t=0}^{T} \sum_{i=0}^{N} [w_i(t \pm p_x i\Delta x)]^2\, dt}$$

Where p_x is the horizontal slowness of an assumed incident wave at time t at R, $w_i(t \pm p_x i\Delta x)$ is the record at time $t \pm p_x i\Delta x$ at the i^{th} receiver at distance $i\Delta x$ from the receiver R. The time

window T is chosen equal to the expected duration of the waveform of the incident wave. If a real wave arrives at the receiver R at the time t with slowness p_x, $w_i(t + p_x i\Delta x)$ are identical across all N receivers and in this case the semblance S has its maximum value 1.

At each time t on the record at R, S is calculated for a range of values of p_x and that which corresponds maximum S is taken as the horizontal slowness at the receiver at that time. The vertical slowness p_z at the time t can be determined from the horizontal slowness using the relation,

$$p_z = \sqrt{\left(\frac{1}{v^2}\right) - p_x^2} \qquad \text{(v = near surface velocity)}$$

The angle of incidence θ at time t at R can be then obtained as,

$$\theta = \sin^{-1}\left(\frac{p_x}{p_z}\right)$$

B.2.6 Relation to Kirchhoff pre-stack depth migration

In both FZI and KPSDM, the amplitudes of the recorded wave-field at a receiver at different recording times are smeared along the isochrons at the respective times. However, in FZI, direction of incidence of the wave-field at the receiver is estimated and the amplitude smearing is restricted only to the potential Fresnel zones on possible reflectors/converter using this additional information (Figure A.10a and Figure B.2c). Thus FZI can be alternatively thought of as Fresnel zone-restricted KPSDM. The time derivative of the recorded wave-field and the weight W from equation A.1 can be incorporated into FZI as well to map relative reflection/conversion strengths of the reflectors/converters.

B.2.7 Relation to Fresnel volume migration

FZI can be closely related to the Fresnel volume migration (FVM) technique (Lüth et al.,

2005, Buske et al., 2009). If the length of the direct path of a seismic wave of wavelength λ between a source S and a receiver R is l and another path via a scattering point D in the vicinity of the direct path is m, then D lies in the Fresnel volume around the ray SR if $|m - l| \leq \frac{\lambda}{2}$ (Kravstov and Orlov, 1990). In FVM, for each recording time t at a receiver R, a ray is traced back into the subsurface reverse to the direction of incidence of the recorded reflected wave-field at R till the time t to the point S' (Figure B.3). Then Fresnel volume around this ray S'R is calculated and the amplitude of the recorded wave field at R at the time t is smeared on the part of the time t P-P reflection isochron (for R and the source S) located inside this volume.

If a reflected wave exists on the record at R at the time t, the Fresnel volume around the back propagated ray S'R intersects the corresponding reflector over an area which can be approximately taken as the Fresnel zone that generated the reflected wave. Thus, in effect, in both FZI and FVM, the back projection process of KPSDM is restricted to the Fresnel zones. Therefore both the FZI and FVM are expected to produce similar results with the same dataset. However, FVM can be relatively more computationally intensive than FZI and it is currently not available for the converted waves.

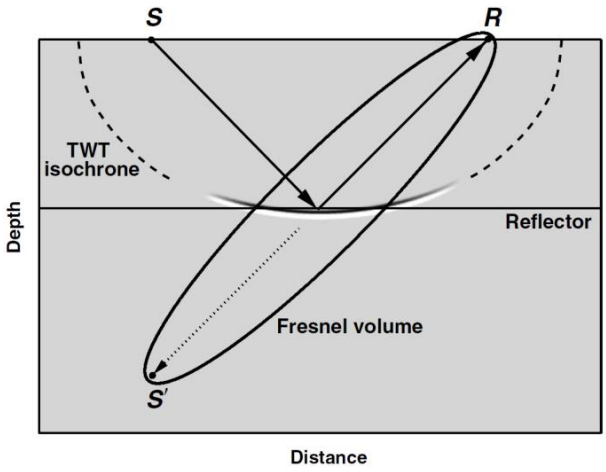

Figure B.3. Principle of Fresnel volume migration for a horizontal reflector in a constant velocity medium. (Buske et al., 2009)

B.3 Synthetic test

In this chapter, the Fresnel zone imaging technique is first tested on two simple synthetic models, one containing a single planar interface and the other containing a single curved interface. The interfaces are imaged using the S-to-P converted transmitted wave and the P-to-P reflected wave employing both FZI and KPSDM. This is then followed by a test on the highly complex Marmousi model using P-to-P reflected waves. In all the tests, the amplitude of the recorded wave-field is used directly instead of its time derivative and the sample smearing is done without any weight. The travel times are calculated using the method of Podvin and Lecomte (1991).

B.3.1 Models

Both the planar and curved models have dimensions of 6 km in x-direction, 5 km in y-direction and 8 km in z-direction and the same velocity and density contrast at the reflecting /converting interface (Figure B.4). For the planar model the interface is a plane with a dip angle of 20^0 at depths between 3.5 km to 1.3 km and for the curved model, the interface is an ellipsoidal segment at depths between 4.9km to 1km.

To generate S-to-P converted transmitted wave, a double couple source is simulated at x=1.5 km, y=2.5 km, z=7.5 km inside the planar model and at x=3.0 km, y=2.5 km, z=7.5 km inside the curved model with a 10Hz Ricker wavelet (Figure B.4b and B.4d top). For the planar model, the simulated wave field is recorded by 30 three component receivers uniformly

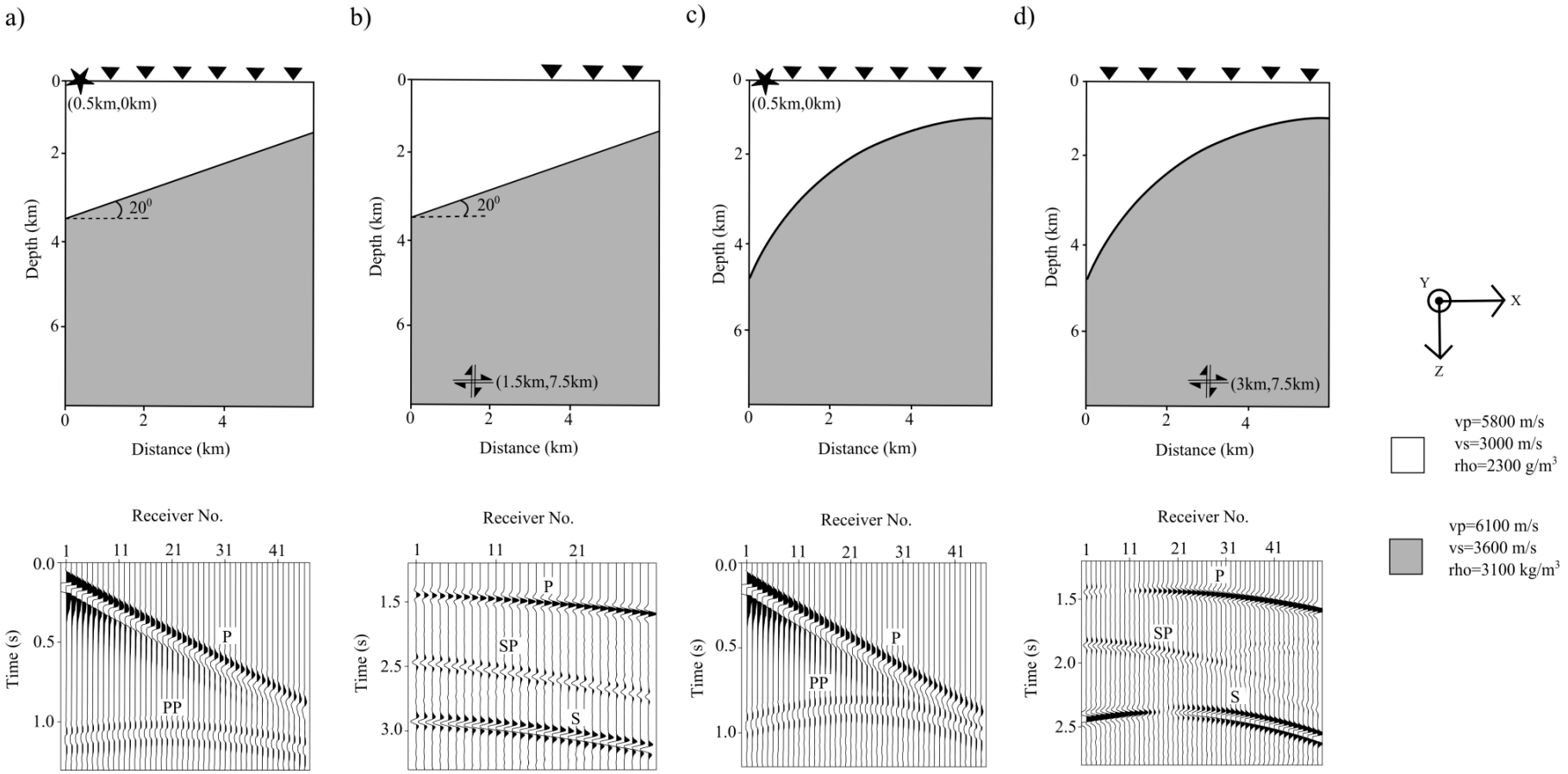

Figure B.4. Models used in the synthetic test, their imaging geometries and vertical component records of the simulated wave fields at the receivers for imaging with different waves; a) planar model with P-to-P reflected wave, b) same model with S-to-P converted transmitted wave, c) curved model with P-to-P reflected wave and d) same model with S-to-P converted transmitted wave.

spaced at interval of 100 m along the x-axis on the top of the model between x=2.5 - 5.4 km at z=0 km and y=2.5 km (Figure B.4b top). The seismogram section of the z-component of these receivers (Figure B.4b bottom) shows clear S-to-P converted arrivals between 2.0s-2.8s. For the curved model, the simulated wave field is recorded by 50 three component receivers uniformly spaced at interval of 100 m along the x-axis on the top of the model between x=0.5 - 5.4 km at z=0 km and y=2.5 km (Figure 4d top). The seismogram section of the z-component of the receivers (Fig. 4d bottom) shows clear S-to-P converted arrivals between 1.7s-2.4s. The direct P and S phases are muted from the z-components of the receivers to obtain seismogram sections containing the S-to-P converted waveforms only.

In case of the P-to-P reflected waves, an explosive source is shot at x=0.5 km, y=2.5 km and z=0 km for both the models with a 10Hz Ricker wavelet (Figure 4a and 4c top). The wave field is recorded by 46 vertical component receivers uniformly spaced at interval of 100m along the x-axis on the top of the models between x=1.0 - 5.5 km at z=0 km and y=2.5 km. Clear P-to-P reflected arrivals are observed at the receivers between 0.8s - 1.2s and 0.7s-1.2s respectively for the planar and curved models (Figure 4a and 4c bottom). Note that the wave-field is simulated with a technique (Promax software package) which does not generate any surface waves. Therefore, by simply muting the first arriving direct wave at each receiver, the shot gather containing the P-to-P reflected waveforms only could be obtained.

B.3.2 Migration

To perform FZI and KPSDM on the synthetic data calculated over the planar and curved models, a 3D grid of dimensions same as the models is defined with 6 km in x-direction, 5 km in y-direction and 8 km in z-direction with uniform grid spacing of 10m. The same uniform grid spacing is used for all of the velocity, travel time and migration grids. Velocity values from the models are assigned to the corresponding grid points to obtain their respective

velocity grids v(x, y, z). The travel time tables for the double couple sources $t_E^S(x, y, z)$ are computed with S wave velocity and for the explosive sources, $t_E^P(x, y, z)$ with P wave velocity. For the receivers the travel time tables $t_R^P(x, y, z)$ are calculated with P wave velocity only. The SP and PP isochrons at a time t can be then obtained by finding grid points with $t_E^S + t_R^P = t$ and $t_E^P + t_R^P = t$ respectively

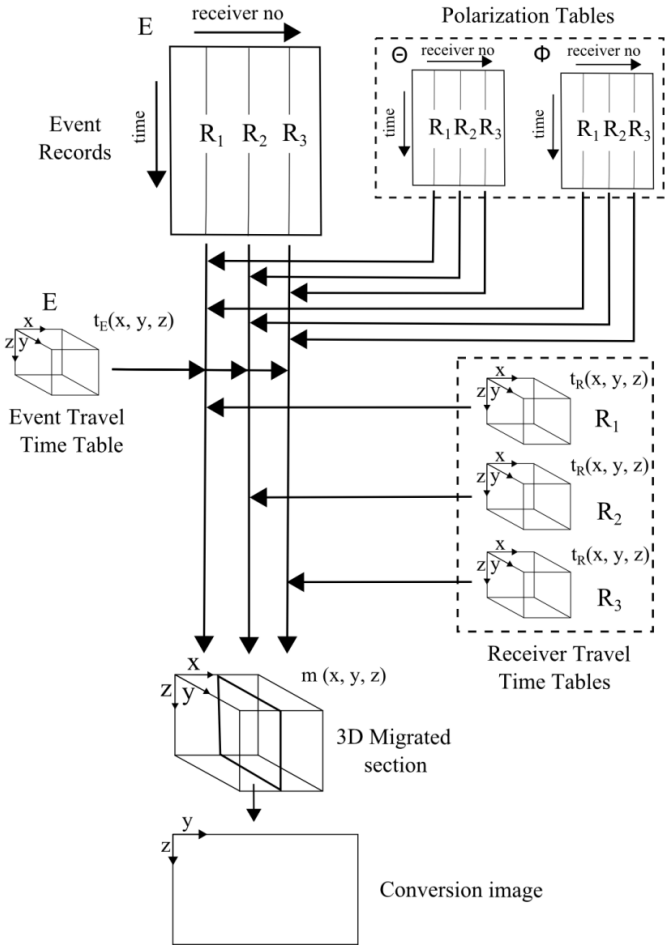

Figure B.5. Work flow for Fresnel zone imaging with S-to-P converted waves using record of a single event E at three receivers R_1, R_2 and R_3.

The data to be migrated consists of four shots. To perform KPSDM on the record at the receiver R for a given shot E, the amplitude of the record at a time t is smeared along the time t SP or PP isochron. To perform FZI on the same record, at each time t, a ray is traced back from R reverse to the direction of incidence of the converted or reflected P wave at R using

the velocity grid. The direction of incidence of the P wave at R is calculated directly by geometrical calculation since the geometry of the converter/reflector is known. A simple ray tracing technique is employed based on the Snell's law.

For the SP converted wave, the ray is back propagated from R till it intersects the SP isochron at time t and the coordinates of this intersection point is noted. The ray tracing is then continued till it intersects the SP isochron at time $t - \frac{T}{2}$ (where T is the dominant period 0.1s of the 10Hz Ricker wavelet) and the coordinates and the normal to the isochron at the intersection point are obtained. For the PP reflected wave, the ray is back propagated till it intersects the PP isochron at time $t - \frac{T}{2}$ and the coordinates and the normal to the isochron at this intersection point are obtained. The ray tracing is then continued till it intersects the PP isochron at time t and the coordinates of the intersection point is again noted. The amplitude of the record at time t is then smeared at only those points of the time t SP or PP isochron that satisfies equation B.1 or B.2.

The above process is repeated for records at each receiver of a shot that results in a 3D migrated section for that shot. A vertical slice of this 3D migrated section along the receiver line at y = 2.5 km is taken as the SP conversion or PP reflection image of the associated model.

Although, the direction of incidence of S-to-P converted wave at a receiver is calculated here directly during the migration, in practice this is pre-calculated from the data e.g. by polarization analysis of record at three component receivers. This result in two polarization sections corresponding to an individual shot that stores the horizontal azimuth angle Φ and the deviation angle from vertical direction Θ of the principal axis of polarization ellipsoid (i.e. direction of incident P-wave) at each recording time at each receiver of the shot. These are referred to as polarization tables.

B.3.3 Results

As a first step, the PP reflection and SP conversion images of the models with the record at a single receiver are investigated (Figure B.6). When the record is smeared along whole isochrons (KPSDM), the back projected energy appears equally along the whole length of the isochrons a significant part of which is not in the vicinity of the reflectors/converters (Figure B.6a and B.6c). Also, from these images it is not possible to make any prediction on the position of the reflecting/converting interfaces inside the models. When the same record is smeared only to the Fresnel zone portions of the same PP reflection and SP conversion isochrons (FZI), the back projected energy is restricted to the reflectors/convertors within the first Fresnel zones (Figure B.6b and B.6d). Although, the actual shape of the reflectors/convertors cannot yet be determined, the position of the reflecting/converting interfaces can be already identified on these images even when record at a single receiver has been employed.

When records at all receivers are included, without Fresnel zone restrictions (KPSDM), the significant amount of back projected energy present away from the reflectors/converters causes substantial noise and artifacts in all of the images (e.g. A, C, E, F in Figure B.7a and B.7c). In particular, in the SP transmitted conversion image of the curved model, a prominent artifact appears (F in Figure B.7c right) as a second vertically oriented converter at depths of 4-8 km. Additionally, in the PP reflection images the top part of the bright spots representing the reflectors appear broken (B and D in Figure B.7a).With Fresnel zone restriction (FZI), the reflecting/converting interfaces in both models are imaged with almost no smearing noise and without any of the above mentioned artifacts. Most remarkable of these is the successful imaging of the curved model with the SP converted transmitted waves (Figure B.7d right) for which the whole isochron smearing approach of KPSDM failed.

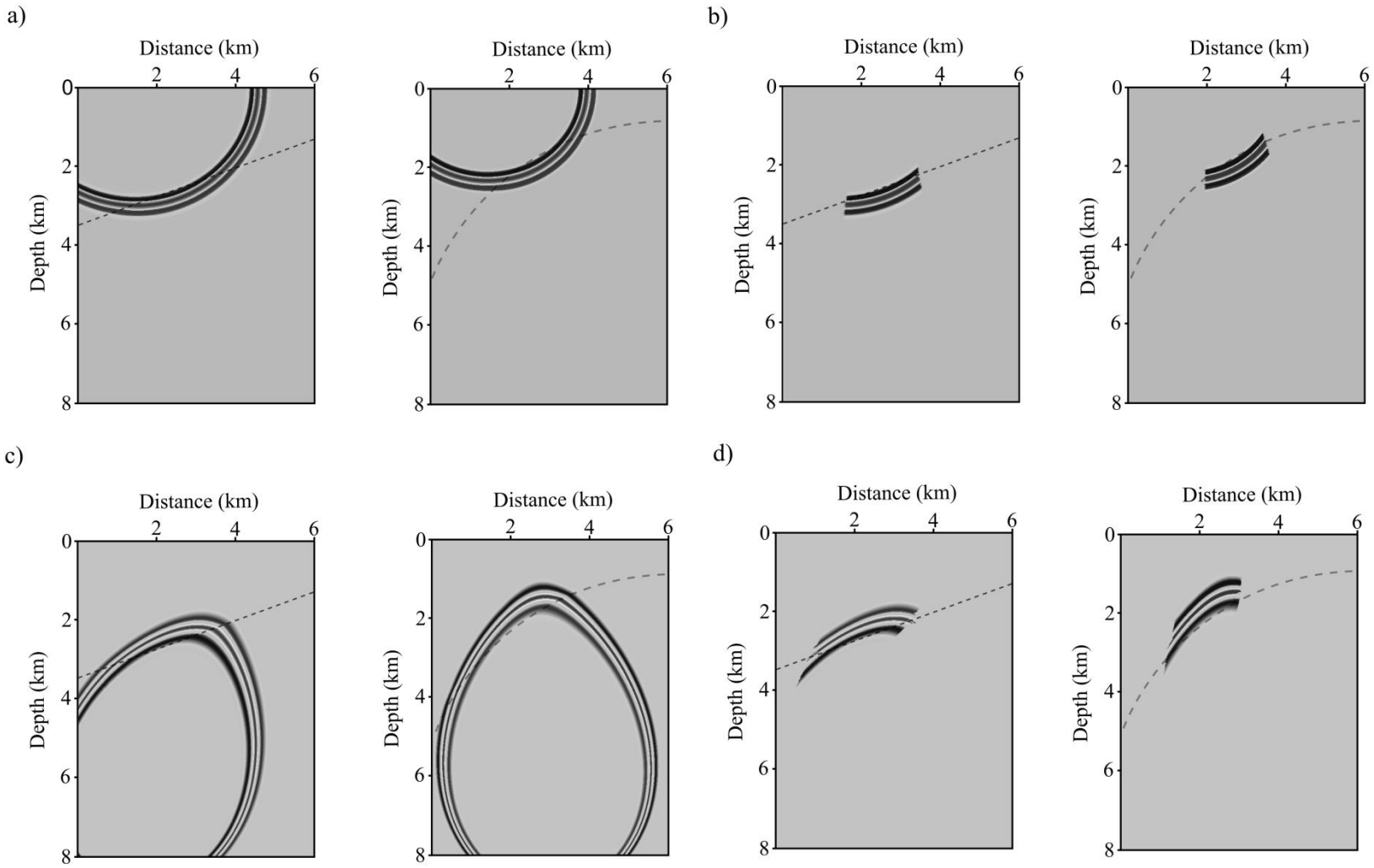

Figure B.6. Record at a single receiver smeared along a) whole P-to-P reflection isochrones, b) Fresnel zone restricted P-to-P reflection isochrones, c) whole S-to-P conversion isochrones and d) Fresnel zone restricted S-to-P conversion isochrones for the planar and curved models.

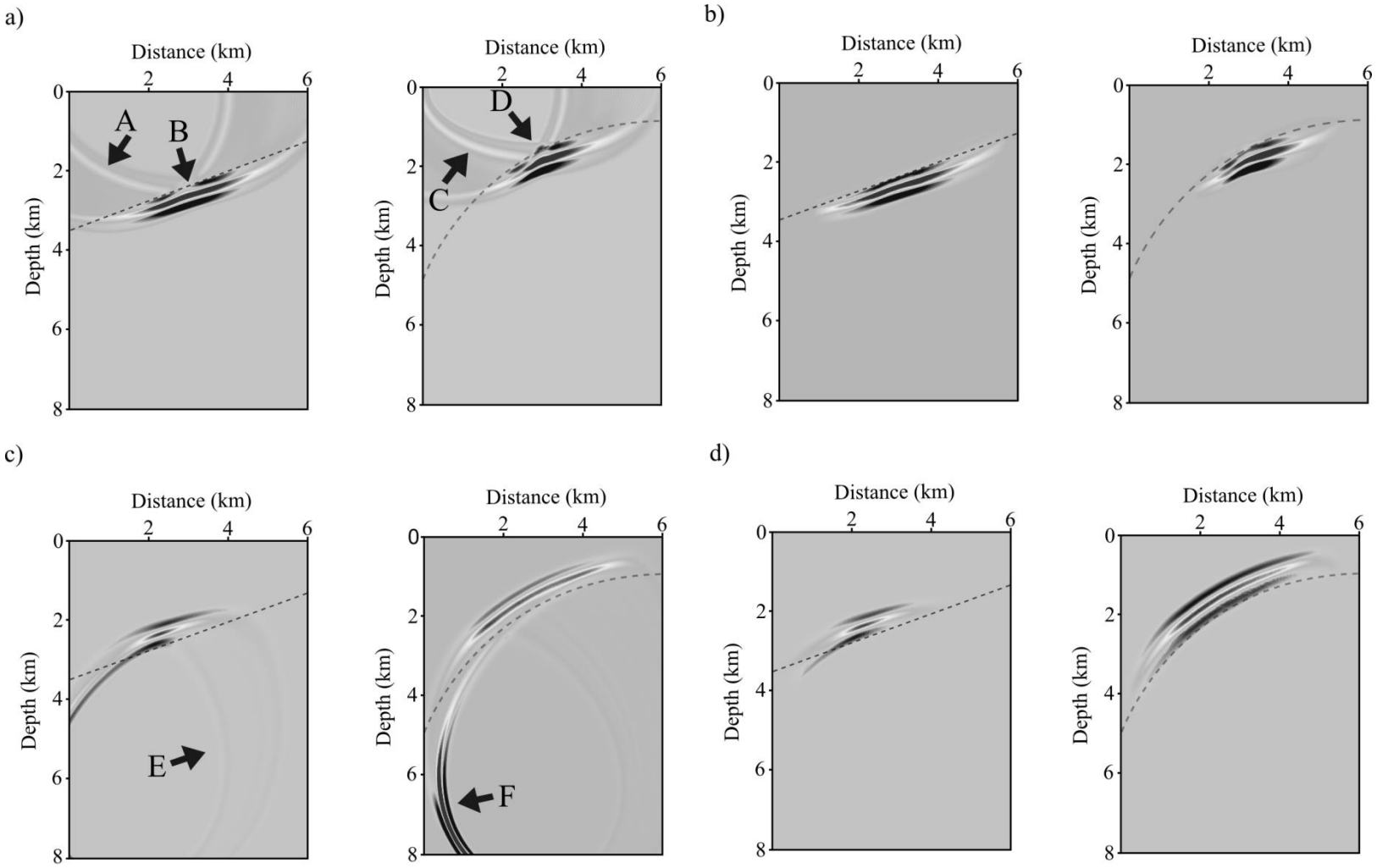

Figure B.7. P-to-P reflection images of the planar and curved models using a) whole isochrons and b) Fresnel zone restricted isochrons. S-to-P conversion images of the same models using c) whole isochrons and d) Fresnel zone restricted isochrons.

Note that the curved reflectors/converters have been imaged in spite of the planar assumption made in calculating the Fresnel zone restrictions. This is because within the Fresnel zone size corresponding to the 10 Hz dominant frequency, the curvature of the curved interface is negligible (Figure B.6b and B.6d right).

B.3.4 Marmousi test

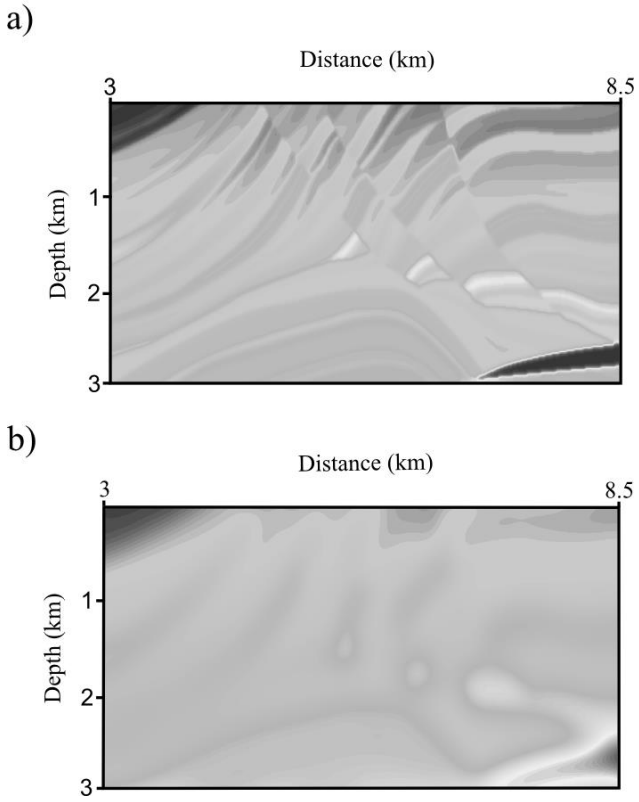

Figure B.8. a) Marmousi model. b) The same model after smoothing.

Marmousi model (Versteeg and Grau, 1991) is a benchmark velocity model widely used to test reflection seismic imaging techniques. It is based on a profile across the North Quenguela trough in the Cuanza basin in Angola and contains numerous reflectors at various dips with significant velocity variations in both horizontal and vertical directions in the range of 1500-5500m/s. This makes the velocity model ideal for synthetic reflection seismic imaging experiments. The original Marmousi model is 2D with depth of 3km and width 9.2 km. For the test, a subset of the model between 3-8.5km is selected which contains most complex part

of the model (Figure B.8a).

A 2D controlled source reflection seismic survey is simulated on top of the chosen subset of the model. The survey comprises of 51 explosive shots with 20Hz Ricker wavelet at regular interval of 100m between 3.2-8.3km. The receiver spread consists of 40 vertical component receivers placed on either side of shot at uniform spacing of 25m. The synthetic data is generated by Promax software package which does not generate surface waves (Figure B.9a). The only noise in the shot gathers is the first arriving direct wave which is removed by applying top mute.

Since the receivers are vertical components only, the direction of incidence of the recorded wave-field at a receiver is computed by calculating horizontal and vertical slowness values at the receiver. The method of Kimball and Marzetta (1984) is used for this slowness estimation (Section B.2.5). This result in two slowness sections for an individual shot gather (Figure B.9b and c), one for the horizontal component of the slowness along the survey line and the second for the vertical component. These are referred to as the slowness tables.

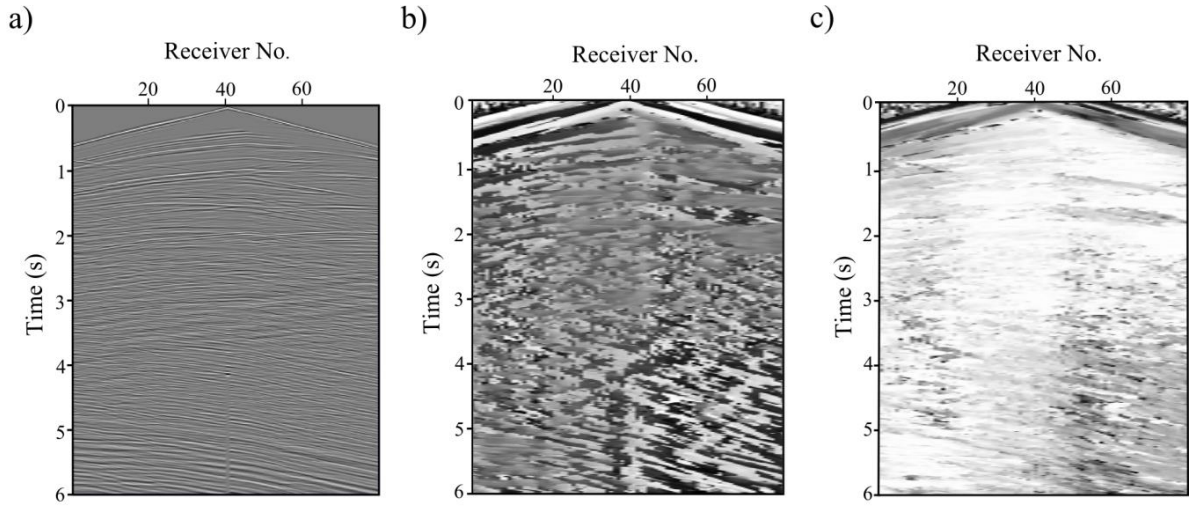

Figure B.9. a) Example synthetic shot gather computed over the Marmousi model. b) Horizontal and c) vertical slowness tables of the same shot gather.

In practice, the velocity model used for migration cannot be known in every detail and is

usually the background velocity model of the subsurface. Also, a smooth velocity model is required for the travel time calculations for both KPSDM and FZI. Thus, the Marmousi velocity model is smoothed prior to application of the imaging techniques (Figure B.8b) on the synthetically generated dataset. A damped least square technique is used for smoothing the model.

B.3.4.1 Migration

To apply KPSDM and FZI on the synthetic data generated over the Marmousi model, a 2D grid is defined with length (x) 5.5km and depth (z) 3km and grid spacing of 4m along all axes. Velocity values from the Marmousi Model are assigned to the corresponding grid points to construct the velocity grid v(x, z). For each of the source and receiver locations the travel time tables $t_E(x, z)$ and $t_R(x, z)$ are computed on this velocity grid using the eikonal solver of Podvin Lecomte (1991).

To perform KPSDM on the record at a receiver R for a shot E, the absolute value of the recorded amplitude at time t is smeared along the PP isochron at time t. To perform FZI on the same record, at each time t, a ray is traced back from R through the velocity grid reverse to the direction of incidence of the recorded wave at R at the time t. The direction of incidence at time t is calculated by retrieving the components of slowness at R at the time t from the pre-calculated slowness tables of E. A simple ray tracing technique is used based on the Snell's law. The ray is back propagated till it intersects the PP isochron at time $(t - \frac{T}{2})$ (where T is the dominant period 0.5s of the 20Hz Ricker wavelet) and the coordinates and the normal to the isochron at the intersection point are obtained. The ray tracing is continued till it intersects the PP isochron at time t and coordinates of the intersection point is again noted. The absolute value of the recorded amplitude at time t is then smeared at only those points of the time t PP isochron that satisfies equation B.2.

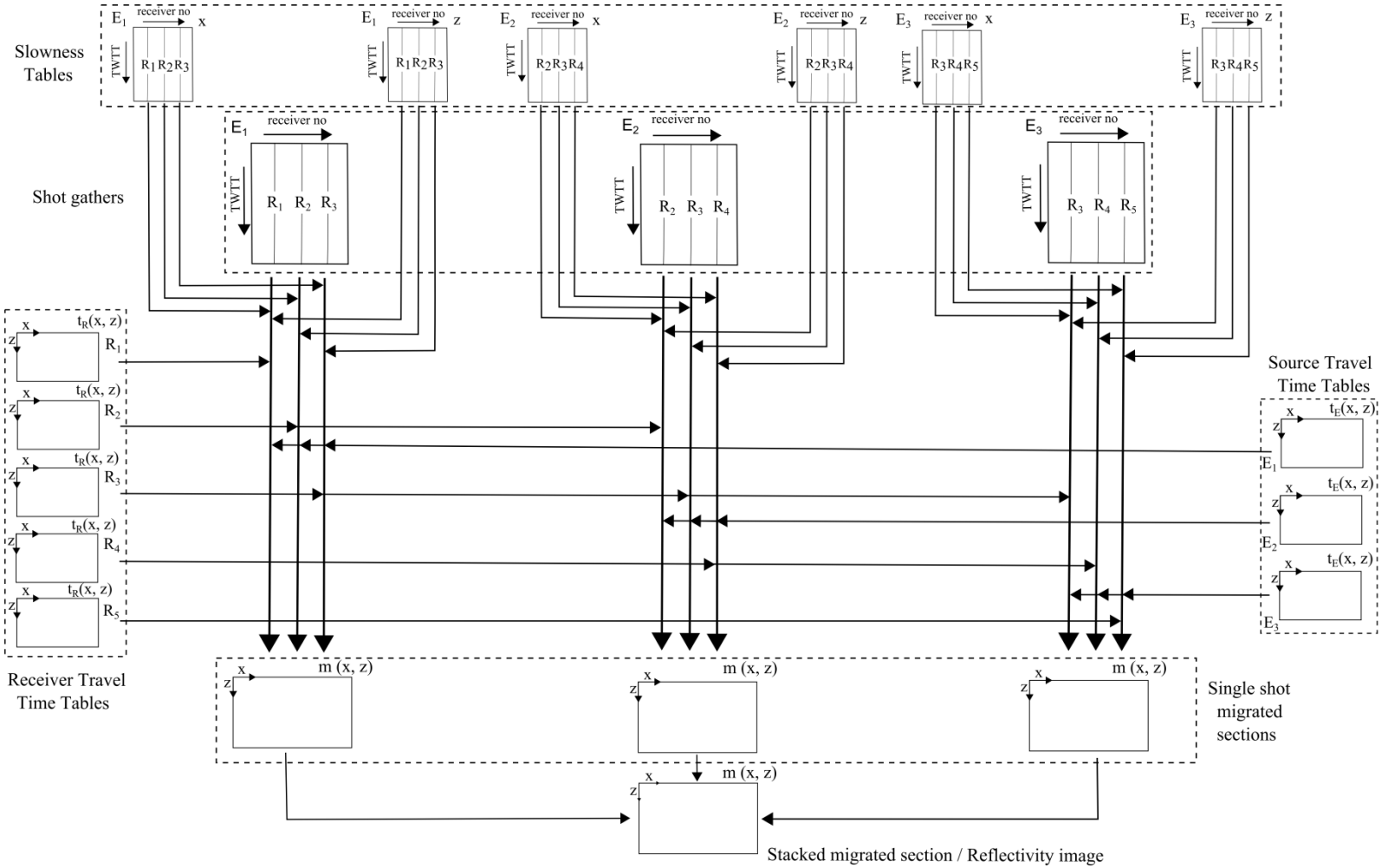

Figure B.10. Work flow for Fresnel zone imaging with P-to-P reflected waves (2D) using three shots E_1, E_2 and E_3 each with records at three receivers R_1-R_2-R_3, R_2-R_3-R_4 and R_3-R_4-R_5 respectively. The shots E_1, E_2 and E_3 are coincident with the receivers R_2, R_3 and R_4 respectively.

The above process is repeated for records at each of the 80 receivers of each of the 51 shots separately. The resulting 2D migrated sections of different shots migrated using an individual technique are then stacked together to obtain the P-P reflection image of the Marmousi model for that technique.

B.3.4.2 Results

First, the P-P reflection images using the KPSDM and FZI techniques on a single shot are inspected. A significant reduction in overall S/N ratio is noted when FZI is employed (Figure B.11). The back projected reflection energy is generally focused in vertical direction with complete absence of the smearing noise on the upper parts and to the sides (e.g. rectangle A in Figure B.11). Moreover, reflectors appear more distinct and continuous (e.g. rectangle B in Figure B.11).

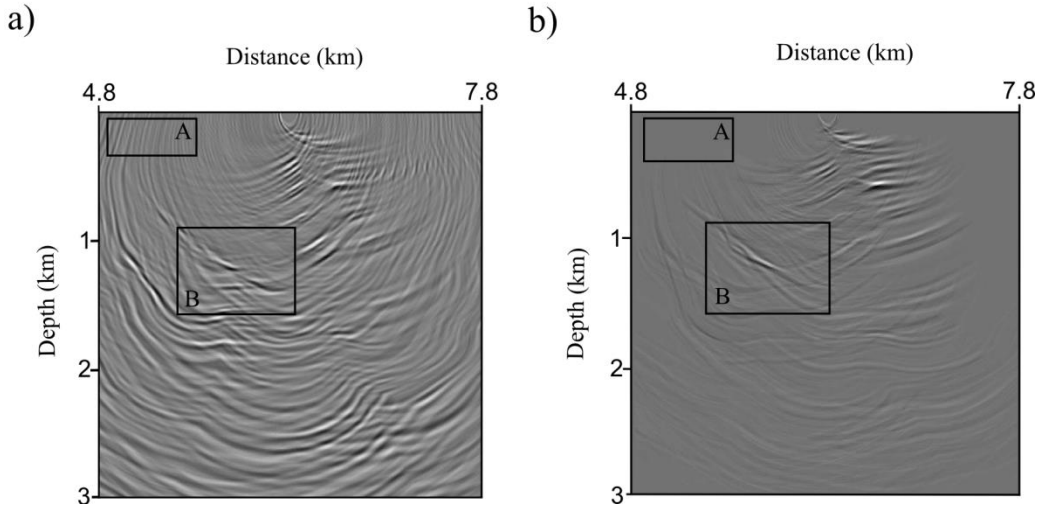

Figure B.11. P-to-P reflection image using a single shot record computed over the Marmousi model using a) Kirchhoff pre-stack depth migration and b) Fresnel zone imaging.

The same improvements can be observed in the final images using all shots as expected. With reduced smearing noise, the FZI image is much cleaner (e.g. rectangle B in Figure B.12). The near surface smearing artifacts are almost absent (e.g. rectangle A in Figure B.12). These S/N differences can have a larger effect on image quality in case of real data which usually

contains a large quantity of random noise. While a moderate amount of smearing noise makes the reflectors obscure, a generous amount can completely hide weaker reflectors. In addition to the general noise enhancements, some artifacts that appear as prominent reflectors in the KPSDM image are not present in the FZI image (e.g. rectangle C in Figure B.12).

In the innermost part of the model, some important reflectors which do show up in the KPSDM image appear to be missing in the FZI image (rectangle D in Figure B.12). This is possibly because of inability of the simple ray tracing technique used to account for the complex velocity variations in this most complicated part of the model. However, overall, the Marmousi model has been successfully imaged by FZI with a number of significant improvements over KPSDM.

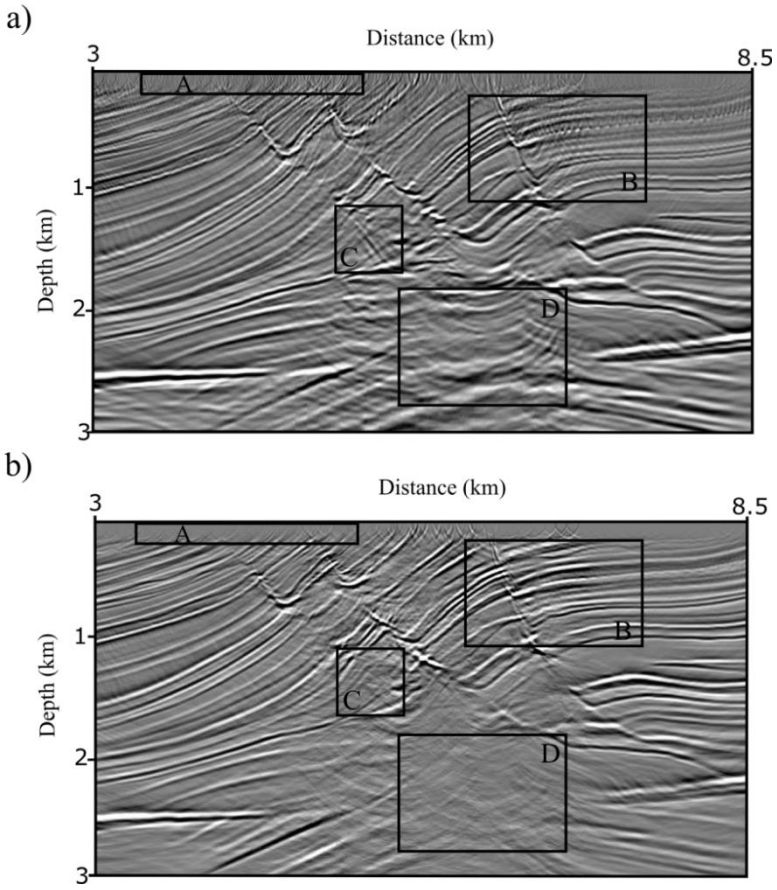

Figure B.12. P-to-P reflection image of the Marmousi Model using a) Kirchhoff pre-stack depth migration and b) Fresnel zone imaging.

B.4 Application on real data

In this chapter, the Fresnel zone imaging technique is demonstrated on two real datasets; a passive micro-seismic earthquake dataset and an active reflection seismic dataset. The datasets are also imaged with KPSDM for comparison as in case of the synthetic tests.

The passive data consists of records of shallow micro-seismic earthquakes (7-10km depth) at an earthquake monitoring station (VACK) located on a sedimentary basin (Cheb; in the same region in Czech Republic where the 9HR profile from part A of this thesis is situated). The S-to-P converted wave at the basement of the basin from the S wave generated by the earthquakes is used to image the bottom edge of the basin. It is observed that in this limited source-receiver coverage, KPSDM fails due to its excessive smearing noise while FZI produces an acceptable image.

The active data is a subset of the deep reflection seismic profile 9HR (~100km from its north-western end) from part A of this thesis. The subsurface reflectivity distribution obtained using data from both a single shot gather and the whole profile show that, even with the enormous source-receiver coverage of the profile, a substantial improvement can be achieved with FZI over KPSDM technique that leads to revelation of new subsurface structures.

B.4.1 Micro-seismic earthquake data

The station VACK is part of the KRASNET network of seismological stations (Figure B.13)

which monitors the regional seismicity of the western Eger rift area at the Czech German border (where northern part of the 9HR profile lies). The area is characterized by frequent small magnitude earthquakes (M_L < 4.0) often in large swarms along a near-vertical plane at depths of 7-10 km (Horalek and Fischer, 2008). The three component records of the events at VACK show a prominent phase on the vertical component arriving shortly before the direct S phase (Figure B.14a). This phase represent the S-to-P converted wave at the bottom of the Cheb basin at estimated depth of around 350m-500m (Fiala and Vejnar, 2004) from the S wave generated by the earthquakes below.

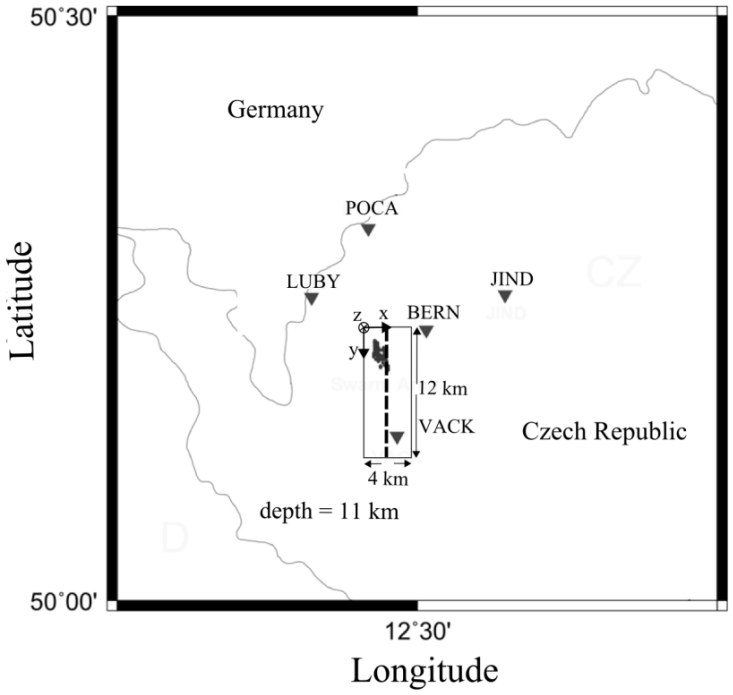

Figure B.13. Stations of KRASNET network (inverted triangles), events from year 2008 swarm (dots) and the grid used to perform Fresnel zone imaging on the records of the same events at the station VACK. The dashed line represents the location of the vertical slice of the migration grid taken as the S-to-P conversion image.

Records of the S-to-P converted phase at station VACK from 67 micro-earthquakes with magnitudes between 1.7-3.1 (Figure B.14b) are selected to image the bottom edge of the Cheb basin using the FZI and KPSDM techniques. For all these events, the waveforms of the SP

phase at the vertical component of the station have similar signatures and a high signal-to-noise ratio (Figure B.14a). Therefore, no further pre-processing of the data is necessary for the application of the imaging approaches. Pre-estimated locations of the hypocenters of the earthquakes are used as the source positions.

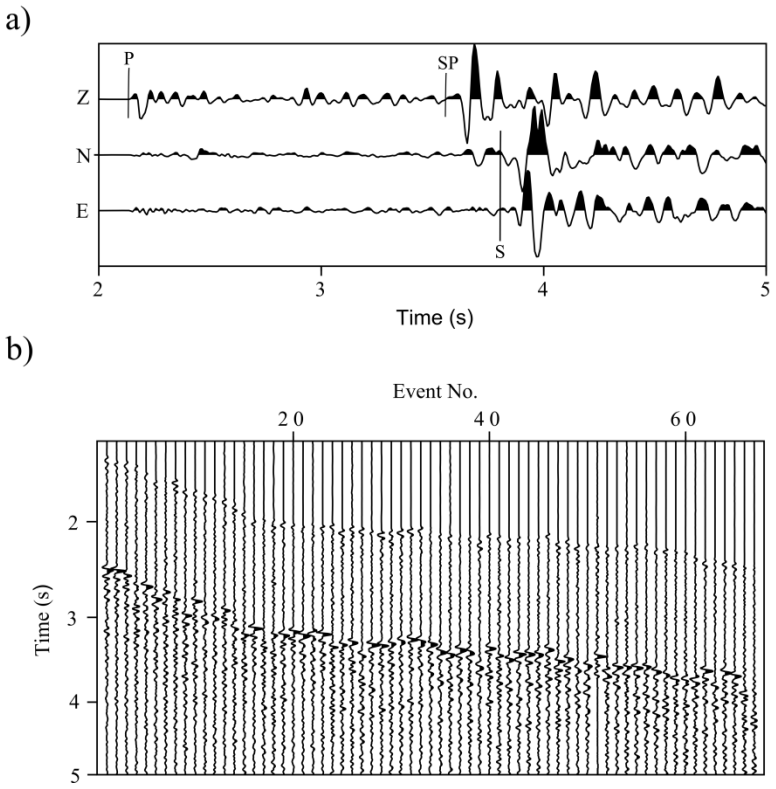

Figure B.14. a) Three component record of a single event (Z = Vertical, N = North and E = East) and b) vertical component record of all 67 events from the year 2008 swarm at the station VACK used for the test.

B.4.1.1 Migration

KPSDM and FZI are applied on the earthquake records at station VACK on a 3D grid with length (x) 12km, width (y) 4km and depth (z) 11km and grid spacing of 20m along all axes (Figure B.13). The same procedure as in section B.3.2 is followed to obtain the velocity and travel time grids with the P and S velocity models of Malek et al. (2005) (Figure A.22b and A.44a).

To perform KPSDM on the record of an event E at station VACK, the amplitudes at different recording times are smeared along SP isochrons of E and VACK at respective times (Figure B.15). To perform FZI on the same record, at each time t, a ray is traced back from the station VACK reverse to the direction of incidence of the S wave at it. The direction of incidence of the SP phase at VACK is calculated by polarization analysis of the three component record.

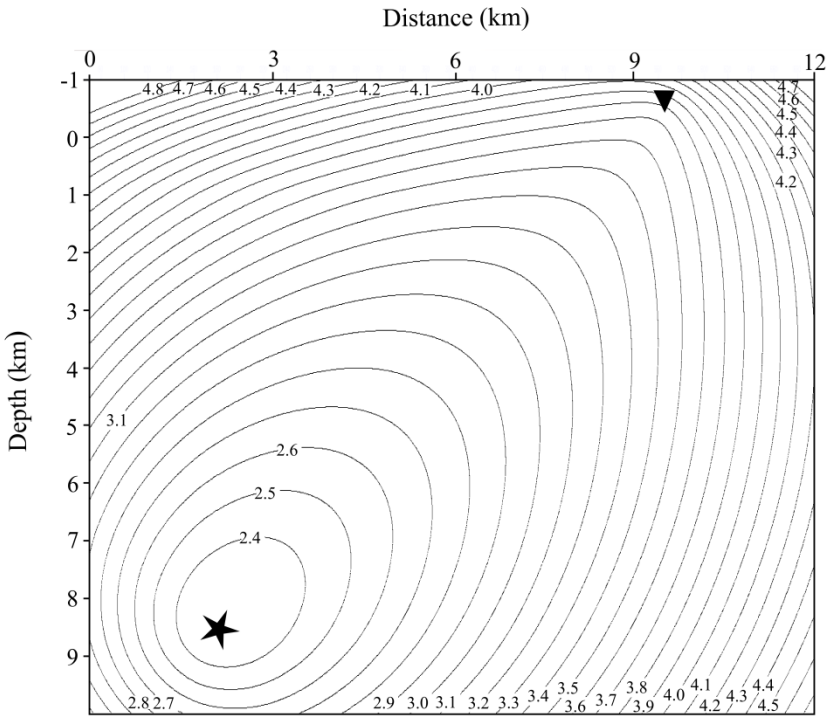

Figure B.15. S-to-P conversion isochrons for the station VACK (inverted triangle) and an event (star) from year 2008 swarm.

The coordinates of the point where this ray intersects the SP isochron at time t is noted. The ray tracing is then continued till the ray intersects the SP isochron at time t - $\frac{T}{2}$ (T = 0.1s corresponding to the dominant frequency of 10 Hz of the SP phase) and the coordinates and the normal to the isochron at the intersection point are obtained. The amplitude of the record at time t is then smeared on the Fresnel zone part of the SP isochron at time t according to equation B.1.

Migration of the record of all the 67 events results in a 3D migrated section. Vertical slice of

the 3D migrated section along x = 2km is taken as the SP conversion image at station VACK.

B.4.1.2 Results

Even without Fresnel zone restriction, most of the back projected S-to-P converted energy recorded at station VACK concentrates below the station at the expected depth range of the basement (Figure B.16a). However, the image is contaminated by prominent artifacts that give hints of additional subsurface structures which cannot be real judging from the geometry of the source and receiver positions (A and B in Figure B.16a). These artifacts are direct consequence of excessive smearing similar to what is observed in the SP conversion image of the curved converter model (Figure B.7c right). Due to the smearing noises present, the exact location of the basement is not very clear in this image.

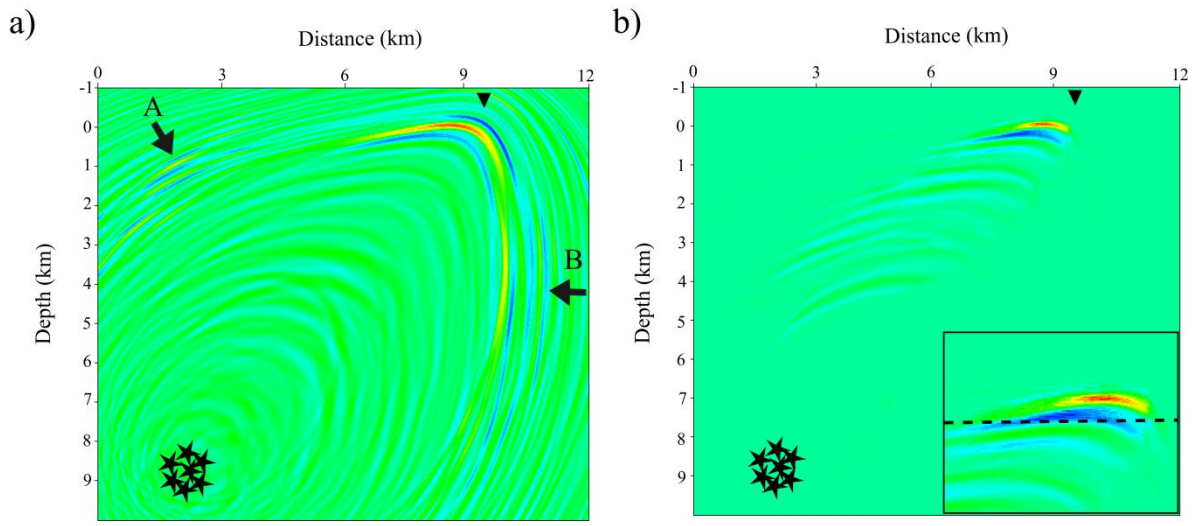

Figure B.16. S-to-P conversion image of the subsurface below the station VACK using a) whole isochrons and b) Fresnel zone restricted isochrons. The inverted triangle and the stars denote the station and the events respectively.

With Fresnel zone restriction, the back projected S-to-P conversion energy is constrained on parts of the SP isochrons that correspond PS transmitted conversion (Figure A.41b). The resulting SP conversion image shows a single, well-focused and strong bright spot below the station VACK (Figure B.16b). The basement can be unambiguously identified at the

anticipated depth of around 400m (bottom edge of the blue band).

B.4.2 Reflection seismic data

The 9HR profile is described in details in section A.3.3. A subset of this profile ~100km from its northern end is taken here for demonstration of FZI (Figure B.17). This part of the profile passes by the swarm area and stops short past the gas escape centers MLZ and KL which are located directly on top of the profile. This is the most interesting section of the profile in relation to the geodynamic activities in the surrounding region. The same preprocessed shot gathers from the section A.3.4 are again used here.

B.4.2.1 Migration

Migration is performed on a 3D grid with length (x) 110km, width (y) 20km and depth (z) 41km and grid spacing of 100m along all axes (Figure B.17). The same procedure as presented in section B.3.3.1 is followed to obtain the velocity and travel time grids. KPSDM is implemented on the record at a receiver R for a shot E by smearing recorded magnitude of the reflected wave field at different recording times along PP isochrons of E and R at respective times (as in section A.3.5.3). FZI is performed on the same record by tracing a ray back from R at each time in the direction reverse of the incident wave at R at that time and then restricting the smearing process to the Fresnel zone part of the PP isochrons at the respective times as in section B.3.3.1. The direction of incidence of the P-to-P reflected waves at the single component receivers are calculated by local slowness analysis (Kimball and Marzetta, 1984).

The above procedure is repeated for records at all receivers of each shot of the chosen subset of the 9HR profile. Then, the 3D migrated sections of all individual shots migrated using an individual technique are stacked together to obtain the final 3D migrated section for that

technique. A vertical slice of this 3D migrated section along the profile line at y = 10km is taken as the reflectivity image of the subsurface below the profile.

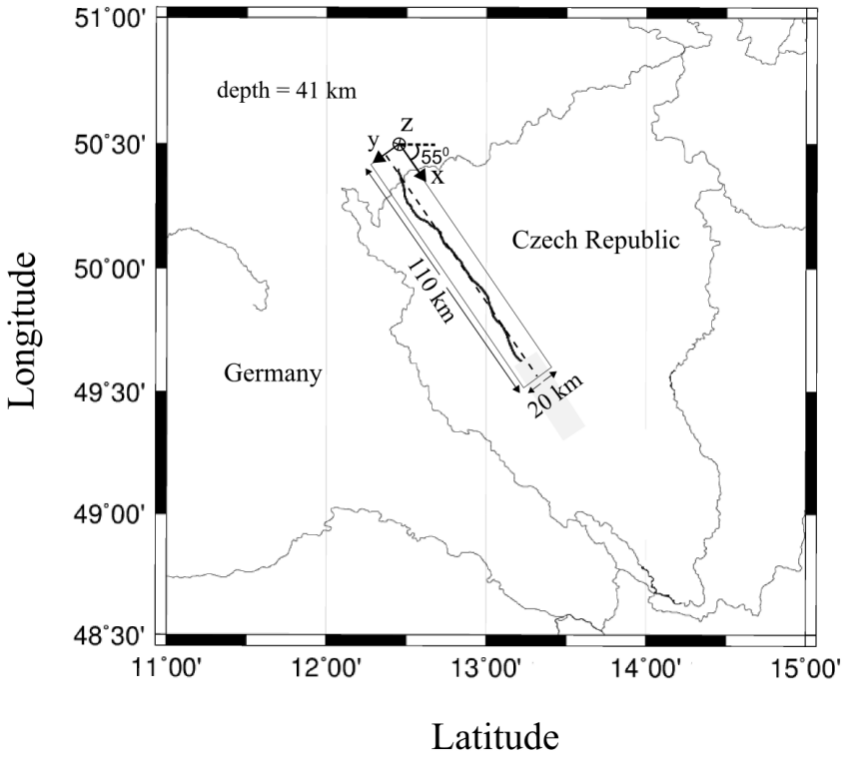

Figure B.17. The grid used to perform Fresnel zone imaging on 9HR profile subset. The dashed line represents the location of vertical slice of the migration grid taken as the P-to-P reflection image below the subset.

B.4.2.2 Results

First, the reflectivity image using data from a single shot located at the north-western end of the profile is investigated. The records at different receivers of this shot show two clearly visible reflected arrivals A and B between 2.0s-3.5s (Figure B.18a).

Smearing the records at the 192 receivers of the shot along whole P-P isochrons result in accumulation of back projected P-to-P reflection energy along two prominent oppositely dipping reflectors (Figure B.18b). These reflectors correspond to the reflected arrivals A and B already seen in the raw shot gather. Unlike the synthetic data (e.g. Figure B.7a or B.11a),

the real data is affected by large amount of random noise. Consequently, smearing along whole isochrons produced a much noisier image as compared to the synthetic cases.

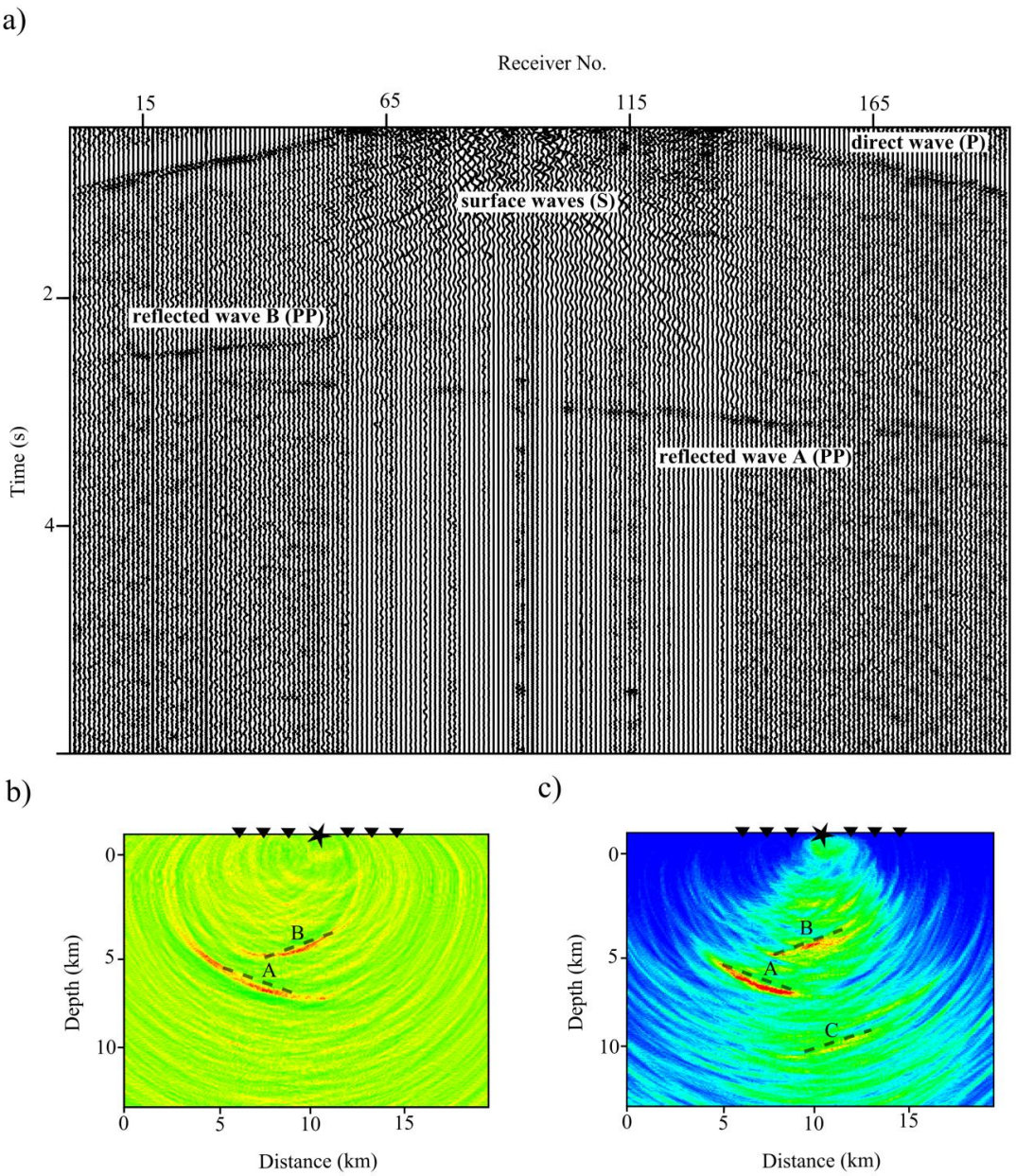

Figure B.18. a) A shot gather (0.5s-6.0s) of 9HR profile with 192 receivers (trace normalization and automatic gain control with window length of 0.4s applied) and P-to-P reflection image of the same shot gather smearing the records at the receivers along b) whole isochrons and c) Fresnel zone restricted isochrons. The star and inverted triangles represent the source and receivers respectively.

When the smearing process is restricted to the Fresnel zone portions of the isochrons, the overall noise is reduced substantially as expected (Figure B.18c). Apart from this general SNR improvement, the reflectors A and B appear more sharply defined and realistic. This is because constraining the smearing process to the reflectors led the constructive interference of the back projected reflection waveforms to localize strictly along the reflectors. Additionally, a new weak reflector C is now visible which is identifiable neither in the image using whole isochrons nor in the raw shot record.

Next, the reflectivity image using all shots of the chosen subset of 9HR profile (Figure B.19) is inspected. Both the images with and without Fresnel zone restriction show the major features of the reflectivity distribution of the crust equally well. The Moho is observed in both images at the average depth 30km along with an upwelling between 20 and 40 km along the profile to a depth of around 27 km. Moreover, a number of distinct diffusively reflective zones of crust containing occasional strong reflectors can be identified in both cases along the whole length of the profile.

However, with the Fresnel zone restriction, a dramatic improvement in overall resolution is achieved as can be anticipated already from the image using the single shot. The reflectors are more continuous and distinct and the diffusively reflective zones are more clearly defined. Numerous new reflectors are revealed throughout the image many of which are not traceable at all without the Fresnel zone restriction. The reflectors A, B and C from the single shot image (Figure B.18c) are more clearly recognized without much difficulty. An interesting pattern of prominent reflectors can be seen extending from near surface down to the Moho between 10km to 45km along the profile. This includes a complex network of weakly reflecting faults directly above the updomed Moho (rectangle D) apparently representing crustal deformations associated with the Moho upwelling process.

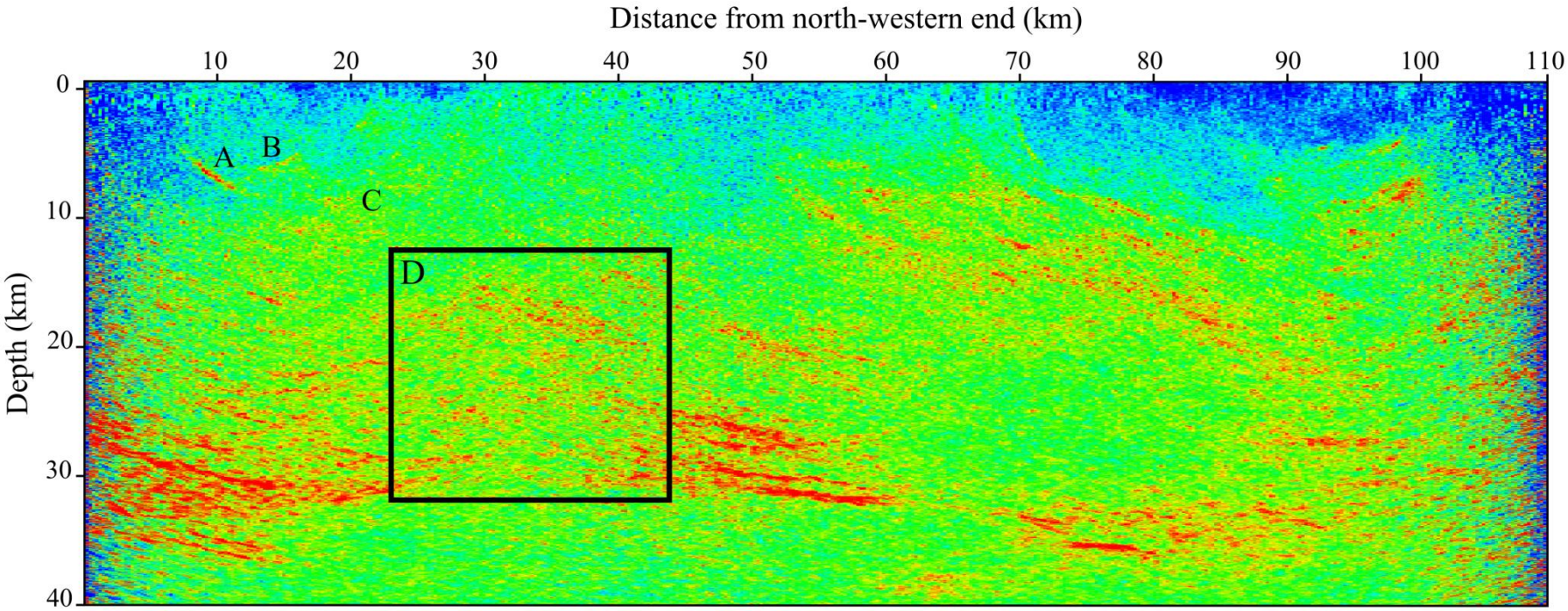

Figure B.19. P-to-P reflection image of the subsurface below 9HR profile using Kirchhoff pre-stack depth migration.

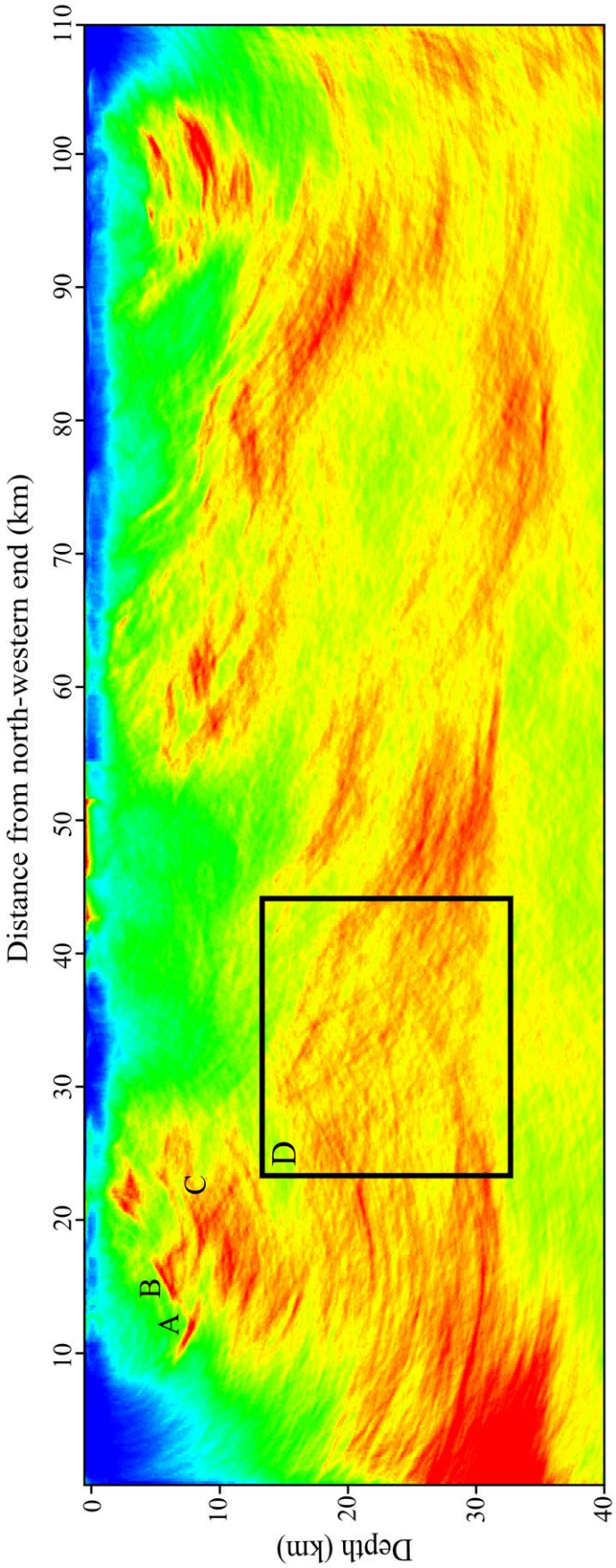

Figure B.20. P-to-P reflection image of the subsurface below 9HR profile using Fresnel zone imaging.

B.5 Conclusions

Seismic imaging is one of the major geophysical tools for scientific investigation of Earth's subsurface. One way to use seismic waves for this purpose is seismic migration in which conversion/reflection events recorded in a seismic section are relocated to their points of origin in the subsurface to map subsurface structures. In the Fresnel zone imaging migration technique presented in this part of the thesis, this is achieved by back projecting the recorded converted/reflected waveforms to all potential Fresnel zones on all possible converters/reflectors that may generate the corresponding converted/reflected waves. An image of the subsurface is produced by constructive interference of these back projected waveforms at the actual converters/reflectors. The Fresnel zones are calculated by using a velocity model and direction of incidence of the recorded wave field at the receivers.

The concept of seismic migration by constructive interference of back propagation of the recorded wave field as employed in FZI is same as in Kirchhoff pre-stack depth migration. The latter migration technique is widely applied because of its advantages such as ability to image high structural complexities, flexibility with source receiver geometry etc. and FZI inherits many of its pros and cons. However, in KPSDM only travel time information of the waves is utilized and a significant proportion of the back projected energy is placed away from actual converters/reflectors. This creates lot of noise and artifacts in the image often completely concealing weak converters/reflectors. In contrast, the direction of incidence of the recorded waves is additionally employed in FZI to limit the back projection only to Fresnel

zones on the converters/reflectors. This improves the S/N considerably and many of the typical artifacts are completely avoided. Tests on synthetic data shows that much of the major noises and image distortions commonly observed in images obtained with KPSDM are not present in images obtained with FZI. Applications on real data further manifest how FZI can indeed provide a superior subsurface image as compared to KPSDM.

As seen in the synthetic experiments, the converter/reflector positions can be identified applying the FZI technique even with record at a single source and receiver pair which is not feasible with the KPSDM method. FZI can in general work with lower source-receiver coverage and more arbitrary source receiver geometry than practically possible with KPSDM. This is evident in employing the techniques on the micro-seismic earthquake dataset for which the latter eventually failed due to unfavorable source and receiver positions. KPSDM is often dip limited for the purpose of suppressing noise and to decrease computation cost. FZI provides solution to both of these issues by focusing of the back projected energy only to the physically relevant part of the converter/reflectors. This does not impose any prior restriction on dips to be imaged and at the same time lowers the computation load since the smearing needs to be done only on subsets of the isochrons.

KPSDM is widely considered as one of the best techniques of seismic imaging. With its unique advantages over KPSDM, FZI appears to be a superior alternative technique based on the same core underlying principle. Thus, FZI can be a very useful tool to investigate subsurface for understanding Earth’s processes and exploring natural resources.

Acknowledgements

I am thankful to my supervisor Prof. Dr. Buske for his helpful advices, guidance and providing the opportunity to carry out the research.

I am also thankful to my colleagues at Institute of Geophysics and Geoinformatics, TU Bergakademie, Freiberg F. Hlousek for providing the local slowness analysis code, O. Hellwig for his help and C. Alexandrakis for her useful language suggestions and checks.

I would like to thank P. Zacherle (Institute of Physics of the Earth, Masaryk University, Brno) for providing waveform data for the station VACK, T. Fischer (Faculty of Science, Charles University in Prague) for providing earthquake locations and W. Geissler (Alfred Wegener Institute, Bremerhaven), H. Kämpf (German Research Centre for Geosciences, Potsdam) for their useful advices.

I would also like to thank all my coauthors for the paper[1] based on the work described in the first part of the thesis who all have contributed in giving the results the final shape.

This research was funded by the German research foundation (DFG), Grant No. SH 55/11-1.

[1] Mullick, N., S. Buske, P. Hrubcová, B. Růžek, S. Shapiro, P. Wigger, and T. Fischer (2015), Seismic imaging of the geodynamic activity at the western Eger rift in central Europe, Tectonophysics, 647-648, 105–111.

References

Alexandrakis, C., Calò, M., Bouchaala, F., Vavryčuk, V. Velocity structure and the role of fluids in the West Bohemia Seismic Zone. Solid Earth, 5, 863-872, (2014).

Babusˇka, V., and Plomerova´, J. Subcrustal lithosphere around the Saxothuringian-Moldanubian suture zone—A model derived from anisotropy of seismic wave velocities, Tectonophysics, 332, 185 – 199 (2001).

Bankwitz, P., G. Schneider, H. Kämpf and E. Bankwitz. Structural characteristics of epicentral areas in Central Europe: study case Cheb Basin (Czech Republic). J. Geodyn, 35, 5-32 (2003).

Bleistein, N. Hagedoorn told us how to do Kirchhoff Migration and inversion, The Leading Edge 18, 918-927 (1999).

Bostock, M. G. Kirchhoff-approximate inversion of teleseismic wave fields. Geophysical Journal International, 149, 787–795 (2002).

Bräuer, K., Kämpf, H., Niedermann, S., Strauch, G., Tesar, J. The natural laboratory NW Bohemia — comprehensive fluid studies between 1992 and 2005 used to trace geodynamic processes. Geochemistry, Geophysics, Geosystems 9, Q04018 (2008).

Bräuer, K., Kämpf, H., Strauch, G. Monthly monitoring of gas and isotope compositions in the free gas phase at degassing locations close to the Nový Kostel focal zone in the western Eger Rift, Czech Republic. Chem. Geol. 290, 163–176 (2011).

Buske, S. 3-D prestack Kirchhoff migration of deep seismic reflection data. Geophys. J. Intern., 137:243-260 (1999).

Buske, S., Gutjahr, S., Sik, S. Fresnel Volume Migration of single-component seismic data, Geophysics, Vol.74, No.6, WCA47-WCA55 (2009).

Dahm, T., Fischer, T. Velocity ratio variations in the source region of earthquake swarms in NW Bohemia obtained from arrival time double-differences. - Geophysical Journal International, 196, 2, pp. 957—970 (2014).

Dèzes, P., Schmid, S.M., Ziegler P.A. Evolution of the European cenozoic rift system: interaction of the Alpine and Pyrenean orogens with their foreland lithosphere Tectonophysics, 389, 1–33 (2004).

Dreger, D.S., Tkalcic, H., Jonston, M. Dilational processes accompanying earthquakes in the Long Valley Caldera. Science 288, 122–125 (2000).

Dueker, K. G., and Sheehan, A. F. Mantle discontinuity structure from midpoint stacks of converted P to S waves across the Yellowstone hotspot track. Journal of Geophysical Research, 102, 8313–8327 (1997).

Fiala, J., Vejnar, Z. The lithology, geochemistry, and metamorphic gradation of the crystalline basement of the Cheb (Eger) Tertiary Basin, Saxothuringian Unit, Bulletin of Geosciences, Vol. 79, No. 1, 41–52 (2004).

Fischer, T., J. Horálek, P. Hrubcová, V. Vavryčuk, K. Bräuer and H. Kämpf. Intra-continental earthquake swarms in West-Bohemia and Vogtland: a review, Tectonophysics (2014).

Geissler, W.H., Kämpf, H., Kind, R., Bräuer, K., Klinge, K., Plenefisch, T., Horalek, J., Zednik, J., Nehybka, V. Seismic structure and location of a CO2 source in the upper mantle of the western Eger (Ohre) Rift, central Europe. Tectonics 24 (TC5001) (2005).

Giese, P. Results of the generalized interpretation of the deep-seismic sounding data, in Explosion Seismology in Central Europe: Data and Results, edited by P. Giese, C. Prodehl, and A. Stein, pp. 201 – 214, Springer, New York (1976).

Goes, S., Spakman, W., Bijwaard, H. A Lower Mantle Source for Central European Volcanism, Science, 286, 1928-1930 (1999).

Granet, M., Wilson, M., Achauer, U. Imaging a mantle plume beneath the Massif Central (France), Earth Planet Sci. Lett., 136, 281-296 (1995).

Griesshaber, E., O´Nions R.K., Oxburgh E.R. Helium and carbon isotope systematics in crustal fluids from the Eifel, the Rhine Graben and Black Forest, F.R.G., Chem. Geol., 99, 213-235 (1992).

Grünthal, G. About the history of earthquake activity in the focal region Vogtland/Western Bohemia. In: P. Bormann (Ed.), Monitoring and analysis of the earthquake swarm 1985/86 in the region Vogtland/Western Bohemia, Akad. der Wissensch. der DDR, Potsdam, pp. 30-34 (1989).

Hagedoorn, J. G. A process of seismic reflection interpretation. Geophysical Prospecting, 2: 85–127 (1954).

Hainzl, S., Fischer, T. Indications for a successively triggered rupture growth underlying the 2000 earthquake swarm in Vogtland/NW-Bohemia. J. Geophys. Res. 107(B12), 2338 (2002).

Hainzl, S. Ogata, Y. Detecting fluid signals in seismicity data through statistical modeling. J. Geophys. Res. 110:B05S07 (2005).

Hainzl,S., Fischer, T., Dahm, T. Seismicity-based estimation of the driving fluid pressure in the case of swarm activity in Western Bohemia. Geoph. J. Int., 191, 271–281 (2012).

Hemmann, A., Meier, T., Jentzsch, G. and Ziegert A. Similarity of waveforms and relative relocation of the earthquake swarm 1997/98 near Werdau, J. Geodyn., 35, 191 – 208 (2003).

Hill, N. R. Gaussian beam migration. Geophysics, 55(11), 1416–1428 (1990).

Horálek, J., Fischer, T. Role of crustal fluids in triggering the West Bohemia/Vogtland earthquake swarms: just what we know (a review). Studia Geophysica et Geodaetica 52, 455–478 (2008).

Hrubcová, P., Środa, P., Špičák, A., Guterch, M., Grad, G.R., Keller, Brückl, E., Thybo, H. Crustal and uppermost mantle structure of the Bohemian Massif based on CELEBRATION2000 data. J. Geophys. Res., 110, B11305 (2005).

Hrubcová, P., Vavryčuk, V., Boušková, A., Horálek, J. Moho depth determination from waveforms of microearthquakes in the West Bohemia/Vogtland swarm area. J. Geophys. Res. 118, 1-17 (2013).

Hua, B., and McMechan, G. Parsimonious 3D post-stack Kirchhoff depth migration: Geophysical Prospecting, 53, 507–522 (2005).

Kimball, C.B., Marzetta, T.M. Semblance Processing of Borehole Acoustic Array Data. Geophysics 49 (3): 274–281 (1984).

Knett, J. Das Erzgebirgische Swarmbeben zu Hartenberg vom 1 Jänner bis Feber 1824. Sitzungsber. Deutsch. Naturwiss. — med. Ver. Böhmen. Lotos Prag N.F. 19, 167–191 (1899).

Kosarev, G., Kind, R., Sobolev, S. V., Yuan, X., Hanka, W., and Oreshin, S., Seismic evidence for a detached Indian Lithospheric mantle beneath Tibet. Science, 283, 1306–1309 (1999).

Kossmat, F. Gliederung des varistischen Gebirgsbaues. Abhandlungen des Sächsischen Geologischen Landesamts 1, 1–39 (1927).

Kravtsov, Y. A., and Orlov, Y. I. Geometrical optics of inhomogeneous media: Springer-Verlag Berlin (1990).

Langston, C. A. Structure under Mount Rainier, Washington, inferred from teleseismic body waves, J. Geophys. Res. 84, 4749–4762 (1979).

Lees, J.M., Multiplet analysis at Coso geothermal. Bull. Seismol. Soc. Am. 88, 1127–1143 (1998).

Lüth,S., Buske, S., Giese, R. & Goertz, A. Fresnel volume migration of multicomponent data. Geophysics, 70(6), 121–129 (2005).

Málek, J., Horálek, J., Janský, J. One-dimensional qP-wave velocity model of the upper crust for the West Bohemia/Vogtland earthquake swarm region. Studia Geophys. Geod. 49, 501–524 (2005).

Maercklin, N. SUPOLAR and SUPOFILT: SU programs for polarization analysis and filtering of three-component data (2001).

Matthews, A., Fouillac, C., Hill, R., O´Nions, R.K., Oxburgh, E. R. Mantle-derived volatiles in continental crust: The Massif Central of France, Earth Planet Sci. Lett., 85, 117-128 (1987).

Mogi, K., Some discussions on aftershocks, foreshocks and earthquake swarms — the fracture of semi-infinite body caused by an inner stress origin and its relation to the earthquake phenomena. Bull. Earthq. Res. Inst. 41, 615–658 (1963).

Parotidis M., Rothert E., Shapiro S.A. Pore-pressure diffusion: A possible triggering mechanism for the earthquake swarms 2000 in Vogtland/NW-Bohemia, central Europe. Geophys. Res. Lett., v.30, No. 20, 2075 (2003).

Passier, M. L., Snieder, R. K. Correlation between shear wave upper mantle structure and tectonic surface expressions: Application to central and southern Germany, J. Geophys. Res.,101(B11), 25,293 – 25,304 (1996).

Plesˇinger, A., Neunhöfer, H., Wielandt, E. Deep structure of the Bohemian massif from phase velocities of seismic surface waves, in Crustal Structure of the Bohemian Massif and the West Carpathians, Exploration of the Deep Continental Crust, edited by V. Bucha and M. (1994)

Plomerová, J., Achauer, U., Babuška, V., Vecsey, L. BOHEMA working group. Upper mantle beneath the Eger Rift (Central Europe): plume or asthenosphere upwelling?Geophysical Journal International 169, 675–682 (2007).

Podvin, P., Lecomte, I. Finite-difference computation of traveltimes in very contrasted velocity models: A massively parallel approach and its associated tools: Geophys. J. Int., 105, 271-284 (1991).

Schleicher, J., Tygel, M., Hubral, P. 3-D true-amplitude finite-offset migration. Geophysics, 58(8), 1112–1126 (1993).

Schneider, W. A., Integral formulation for migration in two and three dimensions. Geophysics, 43, 49–76 (1978).

Shelly, D. R., Hill, D. P. Massin, F., Farrell, J., Smith, R. B., Taira, T. A fluid-driven earthquake swarm on the margin of the Yellowstone caldera, J. Geophys. Res. Solid Earth, 118 (2013).

Sjogreen, B., Petersson, N. A. A fourth order accurate finite difference scheme for the Elastic Wave Equation in second order formulation, Journal of Scientific Computing, 52(1), pp. 17-48 (2012).

Shelly, D. R., Hill, D. P. Massin, F., Farrell, J., Smith, R. B., Taira, T. A fluid-driven earthquake swarm on the margin of the Yellowstone caldera, J. Geophys. Res. Solid Earth, 118 (2013).

Shelly, D., Schuster, G. Reduced-time migration of transmitted PS waves, Geophysics, 68(5), 1695-1707 (2003).

Špičák, A., Horálek, J. Migration of events during the January 1997 earthquake swarm (The West Bohemia–Vogtland region). Stud. Geophys. Geod. 44, 227–232 (2000).

Stewart, R.R., Gaiser, J.E., Brown, R.J., Lawton, D.C. Converted-wave seismic exploration: a tutorial CREWES Research Report 11, CREWES (1999).

Sun, H., Schuster, G. 3D wavepath migration: Geophysical Prospecting, 51, 421–430 (2003).

Taner, M. T., & Koehler, F. Velocity spectra – digital computer derivation and applications of velocity functions. Geophysics, 34, 859–881 (1969).

Tomek, C., Dvorakova, V., Vrana, S. Geological interpretation of the 9HR and 503M seismic profiles in western Bohemia. Jour. Geol. Sci., Series Geology (Prague), v. 47, pp. 43–50 (1997).

Vavryčuk, V. Principal earthquakes: theory and observations from the 2008 West Bohemia swarm. Earth Planet. Sci. Lett. 305, 290–296 (2011).

Vavryčuk, V., Bouchaala, F., Fischer, T. High-resolution fault image from accurate locations and focal mechanisms of 2008 swarm earthquakes in West Bohemia, Czech Republic. Tectonophysics 590, 189–195 (2013).

Versteeg, R., Grau, G., Eds. The Marmousi experience: Proceedings of the 1990 EAEG Workshop, 52nd EAEG Meeting, Eur.Assoc. Expl. Geophys (1991).

Vinnik, L. P. Detection of waves converted from P to SV in the mantle, Physics Earth Planet. Interiors, 15, 39–45 (1977).

Vråna, S., Štědrå, V. Crustal structure of the western part of the Bohemian Massif, Czech Republic, A summary of the project "Geological model of western Bohemia, related to the deep borehole KTB in Germany", Vol 21, no. 4.(1998).

Wagner, G.A., Gögen, K., Jonckheere, R., Wagner, I., Woda, C. Dating of Quaternary volcanoes Komorní Hůrka (Kammerbűhl) and Železna Hůrka (Eisenbűhl), Czech Republic, by TL, ESR, alpha-recoil and fission track chronometry. Z. Geol. Wiss., 30(3), 191 – 200 (2002).

Weinlich, F.H., Bräuer, K., Kämpf, H. Strauch, G., Tesa, J., Weise, S.M. An active subcontinental mantle volatile system in the western Eger Rift, Central Europe: Gas flux, isotopic (He, C, and N) and compositional fingerprints. Geochim. Cosmochim. Acta, 63:3653-3671 (1999).

Wyss, M., Shimazaki, K., Wiemer, S. Mapping active magma chambers by b values beneath the off-Ito volcano, Japan. J. Geophys. Res. 102 (B9), 20,413–20,422 (1997).

For reasons of data protection, the curriculum vitae is not published in the electronic version.